Analysis Note

Measurement of charged particle production in diffractive proton-proton collisions at $\sqrt{s} = 200$ GeV with tagging of the forward scattered proton

Leszek Adamczyk[1], Łukasz Fulek[1], Mariusz Przybycień[1], and Rafał Sikora[1]

[1] *AGH University of Science and Technology, FPACS, Kraków, Poland*

5th March 2020

In this note we present the analysis of the Single Diffractive Dissociation process with the STAR Roman Pot detectors at RHIC. The measurement is focused on the charged particle multiplicity, its dependence on the transverse momentum and pseudorapidity in three regions of ξ: $0.02 < \xi < 0.05$, $0.05 < \xi < 0.1$ and $0.1 < \xi < 02$. The identified particle to antiparticle (pion, kaon, proton and their antiparticle) multiplicity ratios as a function of transverse momentum in above three ξ regions are also measured. The data come from proton-proton collisions collected in 2015. The forward proton was tagged in the STAR Roman Pot system while the charged particle tracks were reconstructed in the STAR Time Projection Chamber (TPC). We describe all stages of the analysis involving comparison of the data with MC simulations and systematic uncertainty studies. More technical parts of the analysis are described in a supplementary analysis note [1].

List of contributions

Leszek Adamczyk	Analysis coordination/supervision, production of picoDST, production of embedded MC samples
Łukasz Fulek*	Main analyzer, write-up author
Mariusz Przybycień	Analysis supervision
Rafał Sikora	Analysis support

* - contact editor

Change log

5th March 2020	ver. 1.0	Initial revision

Contents

I

1. Introduction

Inclusive measurements of charged-particle distributions in proton–proton (pp) collisions probe the strong interaction in the low-momentum transfer, non-perturbative regime of Quantum Chromodynamics (QCD). In this kinematic region interactions are usually described by phenomenological models implemented in Monte Carlo (MC) event generators. Measurements can be used to constrain the free parameters of these models. An accurate description of low-energy strong interaction processes is essential for understanding and precise simulation of different types of pp processes and the effects of multiple pp collisions in the same bunch crossing at high instantaneous luminosity at hadron colliders. Measurements with tagging of the forward-scattered proton are of special interest. They give direct access to specific but still significant part of pp processes called diffraction. In addition precise modelling of forward particle production is essential for better understanding of the longitudinal development of air showers observed in experiments studying cosmic radiation.

We present a measurement of charged particle production in events with single proton tagging (dominated by Single Diffraction (SD): $p + p \rightarrow p + X$). The following observables are studied:

$$\frac{1}{N_\text{ev}} \frac{dN_\text{ev}}{dn_\text{ch}}, \qquad \frac{1}{N_\text{ev}} \frac{1}{2\pi p_\text{T}} \frac{d^2 N}{d\bar{\eta} dp_\text{T}}, \qquad \frac{1}{N_\text{ev}} \frac{dN}{d\bar{\eta}} \tag{1.1}$$

where n_ch is the number of primary charged particles within kinematic range given by $p_\text{T} > 200$ MeV and $|\eta| < 0.7$, N_ev is the total number of events with $2 \leq n_\text{ch} \leq 8$, N is the total number of charged particles within the above kinematic acceptance and $\bar{\eta}$ is the pseudorapidity of the charged particle with longitudinal momentum taken with respect to direction of the forward scattered proton. To suppress non-SD events the trigger system required no signal in BBC-small in the direction of forward scattered proton and signal in BBC-small in opposite direction. The measurements are performed in a fiducial phase space of the forward scattered protons of $0.04 < -t < 0.16$ GeV^2/c^2 and $0.02 < \xi < 0.2$, where ξ is the fractional energy loss of the scattered proton. In case of SD process $\xi = M_\text{X}^2/s$, where M_X is the mass of the state X into which one of the incoming proton dissociates and s is the center of mass energy squared of the pp system. The above mentioned observables are presented in three ξ regions: $0.02 < \xi < 0.05$, $0.05 < \xi < 0.1$ and $0.1 < \xi < 0.2$. In addition their average values in an event are presented as a function of ξ.

We have also studied an identified particle to antiparticle (pion, kaon, proton and their antiparticle) multiplicity ratios as a function of p_T also in the above mentioned three regions of ξ. The system X into which proton diffractively dissociates has net charge and baryon number +1. It is believed that initial charge and barion number should appear in the very forward direction leading to the equal amount of particles and antiparticles in the central region created by fragmentation and hadronization processes. However other scenarios are also possible where extra baryon is uniformly distributed over rapidity [2] or even appear close to the gap edge [3]. It is natural to expect that possible charge and baryon number transfer to central region will be better visible at small ξ where amount of particle-antiparticle creation is smaller due to the generally smaller particle multiplicity or due to the fact that gap edge is inside our fiducial region of $|\eta| < 0.7$.

2. Monte Carlo Samples

MC samples used to correct data for detector effects were obtained by the embedding MC technique [4], in which simulated particles are mixed with the real Zerobias events at the raw data level. Zerobias data events used in the embedding were sampled over the entire data-taking period in order to properly describe the data set used in the analysis. Two samples of embedding MC were produced:

1. Single particle MC, in which particles are generated from flat distributions in η and p_{T}, in order to have similar statistics in all bins.

2. The Schuler and Sjöstrand (SaS) model implemented in PYTHIA8 with 4C tune.

The particles were propagated through the full simulation of the STAR-TPC and RP system detectors using GEANT3 [5] and GEANT4 [6], respectively. Obtained information for the simulated particles was embedded into the existing information of the real data. These events were next processed through the full reconstruction chain.

It is preferred to get the detector corrections from a MC, which is dedicated to simulate the studied physics process. However, for this purpose, the statistics in the MC should be several times greater than we have in the data for analysis. Since this is not possible with low efficiency of TPC and TOF, the basic method of corrections used in the analysis is a method of factorization of global efficiency into the product of single-particle efficiencies. In this way, statistically precise multidimensional corrections on TPC and TOF are obtained from the single particle MC.

Additionally, several pure MC samples were generated. The simulated particles were propagated through full simulation and reconstruction chain but were not embedded into Zerobias events. Systematic effect related to hadronization of the diffractive system was determined by using an alternative hadronization model implemented in HERWIG. The comparison to the corrected data distribution was done for PYTHIA 8 4C (SaS) and HERWIG, in addition all results were compared to the EPOS and alternative PYTHIA 8 model Minimum Bias Rockefeller (MBR) with A2 tune. EPOS predicts very large contribution of forward protons, which originate from non-diffractive events and are well separated in rapidity from other final state particles. This is the result of low mass excitation of the proton remnant (< 1 GeV) leading to hadronization of the beam remnant back to the proton. Therefore for the comparison with uncorrected data EPOS predictions were separated in two classes: diffractive (EPOS-SD) modelled by Pomeron exchange and non-diffractive modelled by low mass excitation of the proton remnant (EPOS-SD′). In all PYTHIA 8 models, diffractive cross-sections are scaled by the fudge factors, which were introduced in order to describe the full phase space [7, 8]. As a result, diffractive cross sections are arbitrary suppressed at relatively large values of ξ (>0.05). This arbitrary suppression significantly changes predicted distribution of ξ and fractions of different processes in our fiducial phase space. Therefore data was also compared with expectations obtained without suppression of the diffractive cross sections (MBR-tuned).

Figure 2.1 shows $\log_{10} \xi$ and $|t|$ distributions generated with EPOS (SD and SD′) and PYTHIA 8 SD (MBR and MBR-tuned). There are differences among models in both the low and high ξ regions. In the STAR acceptance region, there is a significant contribution of SD′ in EPOS, while SD contribution is suppressed. In addition, the t-slope is very different for EPOS-SD and SD′ compared to PYTHIA 8 predictions. The PYTHIA 8 (MBR-tuned) expectations, as opposed to the MBR model, lead to the larger cross-sections in the high-mass regions.
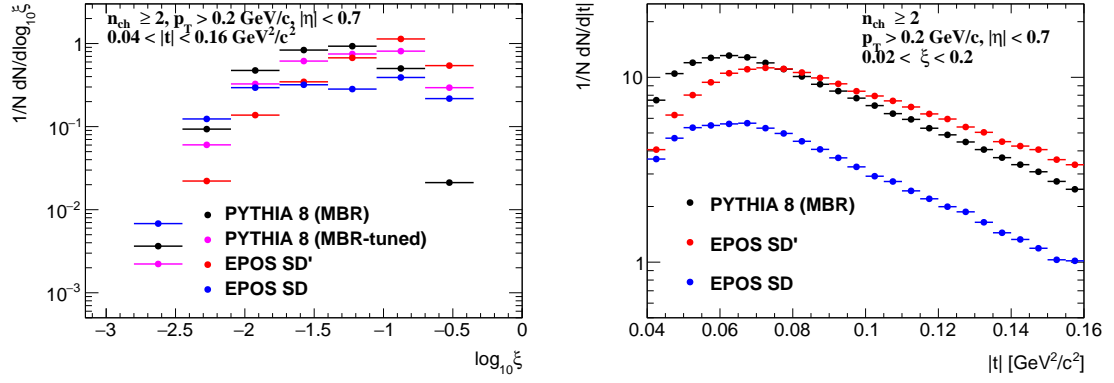
Figure 2.1: (left) $\log_{10}\xi$ and (right) $|t|$ distributions for various MC generators at $\sqrt{s} = 200$ GeV.

3. Data Sample and Event Selection

The data sample used in this analysis was collected in proton-proton collisions at centre-of-mass energy of $\sqrt{s} = 200$ GeV during RHIC Run 15, i.e. in year 2015.

Figure 3.1: Integrated number of events collected for each trigger in the RP data stream during Run 15.

All of the studies in this work use data from only the SDT trigger condition, which was the main trigger designed for SDD studies in Run 15 and used in this analysis. It was formed by the following conditions combined with the logical AND:

1. RP_EOR || RP_WOR - signal in at least one RP on one side of the STAR central detector.

2. Veto on any signal in small BBC tiles or ZDC on the triggered RP side of the STAR central detector.

3. At least two TOF hits.

Above requirements were imposed in accordance with the diffractive events topology. Veto on any signal in small BBC tiles and ZDC allows to accept only events with rapidity gap and reject diffractive events with parallel pile-up event. The requirement of at least two TOF hits was to ensure activity in the mid-rapidity.

Integrated luminosity delivered by the RHIC to the STAR detector in pp collisions during Run 15 amounts to 185.1 pb^{-1} [9], whereas about 34.4M SDT events were gathered by the STAR detector, shown in Fig. 3.1, which corresponds to 16 nb^{-1} of integrated luminosity.

3.1 Event Selection

Events were selected from those passing the SDT trigger condition. In order to remove events having poor quality and background the following conditions were required:

1. Trigger signals in exactly two stations of one arm of RP system,

2. Any trigger signal in small BBC tiles on the opposite side of the STAR central detector to the triggered RP station,

4

3. Exactly one proton track in the above RP stations with $0.02 < \xi < 0.2$ and $0.04 < -t < 0.16$ GeV^2/c^2.

4. Exactly one primary vertex with TPC tracks matched with hits in TOF (later in the text such vertex is refered as a TOF vertex),

5. TPC vertex within $|V_z| < 80$ cm - events with vertices away from the IP have low acceptance for the central and forward tracks,

6. At least two but no more than eight primary TPC tracks, $2 \leq n_{\text{sel}} \leq 8$, matched with hits in TOF and satisfying the selection criteria described in Sec. 3.2,

7. If there are exactly two primary tracks satisfying above criteria and exactly two global tracks used in vertex reconstruction (Sec. 6.1), the longitudinal distance between these global tracks should be smaller than 2 cm, $|\Delta z_0| < 2$ cm, due to small ($< 20\%$) vertex reconstruction efficiency for tracks with $|\Delta z_0| > 2$ cm (as described in Sec. 6.1).

Figure 3.2 shows the multiplicity of TOF vertices (left) and the z-position of primary vertex in a single TOF vertex events (right). Data are compared to embedded PYTHIA 8 SD sample. These distributions are not significantly process-dependent, therefore, contributions from other processes are not included in these plots.
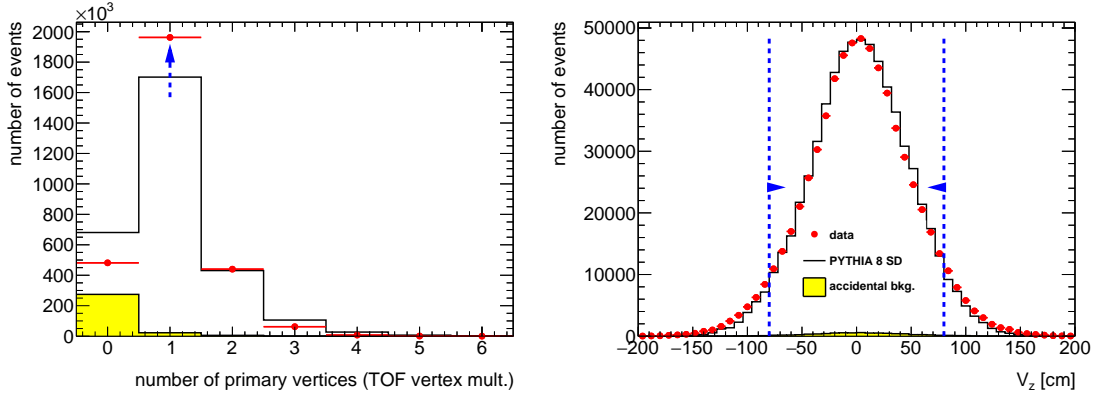

Figure 3.2: (left) Primary vertex multiplicity and (right) the z-position of primary vertex in a single TOF vertex events before applying the cut on the quantity shown. Blue lines indicate regions accepted in the analysis.

3.2 Track Selection

The following quality cuts had to be passed by the selected primary tracks in this analysis:

1. The tracks must be matched with hits reconstructed in TOF,

2. The number of the TPC hits used in the helix fit $N_{\text{hits}}^{\text{fit}}$ must be greater than 24,

3. The ratio of $N_{\text{hits}}^{\text{fit}}$ to the number of all possible TPC hits, $N_{\text{hits}}^{\text{fit}}/N_{\text{hits}}^{\text{possible}}$, must be greater than 0.52,

4. The number of the TPC hits used to determine the dE/dx information $N_{\text{hits}}^{\text{dE/dx}}$ must be greater than 14,

5. The transverse impact parameter with respect to the beamline d_0 must be less than 1.5 cm,

5

177   6. The radial component of the distance of the closest approach between the global helix and
178   the vertex DCA_{xy} must be less than 1.5 cm (consistent with the d_0 limit),

179   7. The absolute magnitude of longitudinal component of the distance of the closest approach
180   between the global helix and the vertex $|DCA_z|$ must be less than 1 cm,

181   8. The track's transverse momentum p_T must be greater than 0.2 GeV/c,

182   9. The track's absolute value of pseudorapidity $|\eta|$ must be smaller than 0.7.

183   The N_{hits}^{fit} and $N_{hits}^{fit}/N_{hits}^{possible}$ cuts are used to reject low quality TPC tracks and avoid track
184   splitting effects. The d_0 and global DCA_{xy}, $|DCA_z|$ cuts are used to select tracks that originate
185   from the primary interaction vertex. The cut on $N_{hits}^{dE/dx}$ is used to ensure that selected tracks
186   have sufficient energy loss information for particle identification purposes. In this analysis tracks
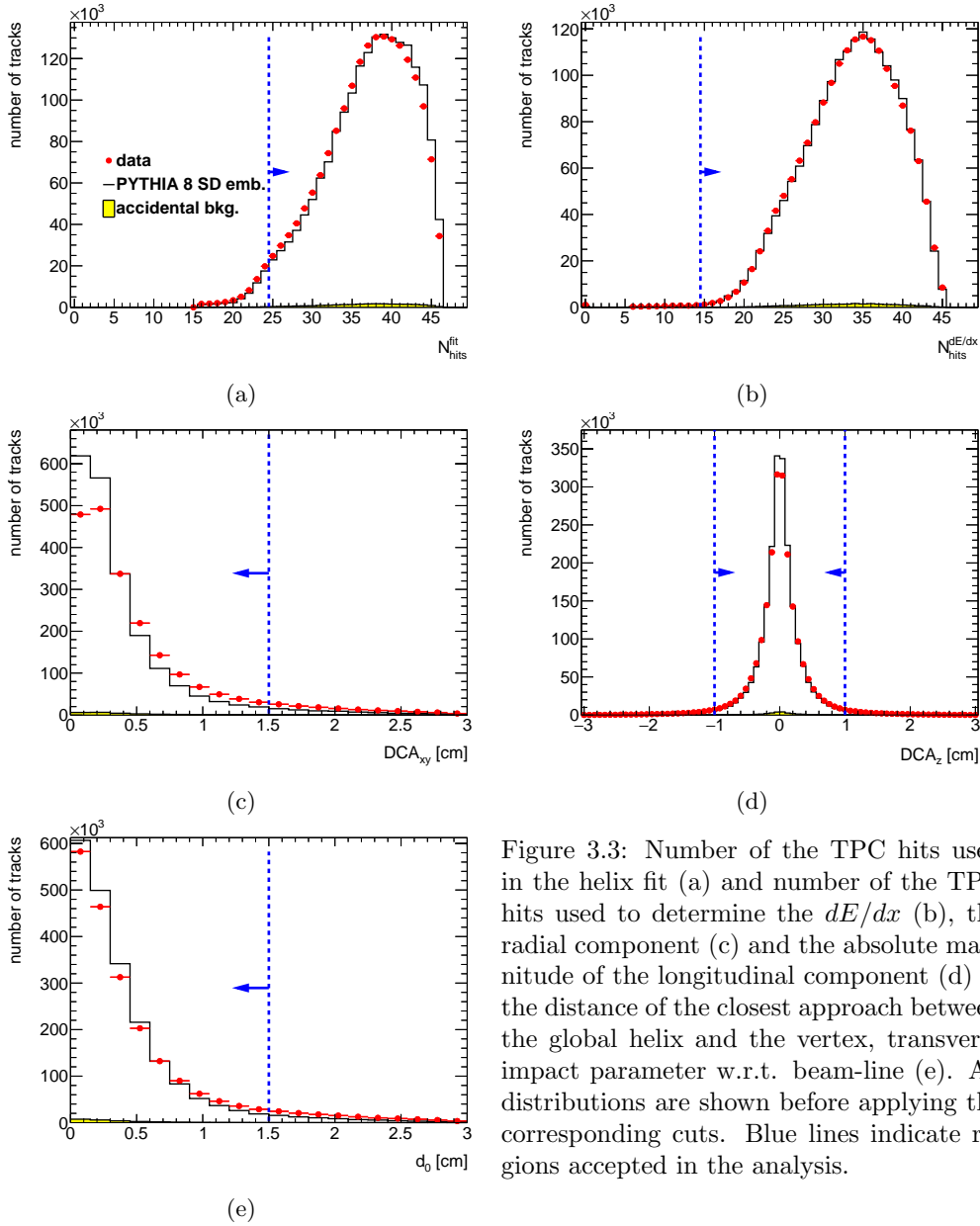

(a)

(b)

(c)

(d)

(e)

Figure 3.3: Number of the TPC hits used in the helix fit (a) and number of the TPC hits used to determine the dE/dx (b), the radial component (c) and the absolute magnitude of the longitudinal component (d) of the distance of the closest approach between the global helix and the vertex, transverse impact parameter w.r.t. beam-line (e). All distributions are shown before applying the corresponding cuts. Blue lines indicate regions accepted in the analysis.
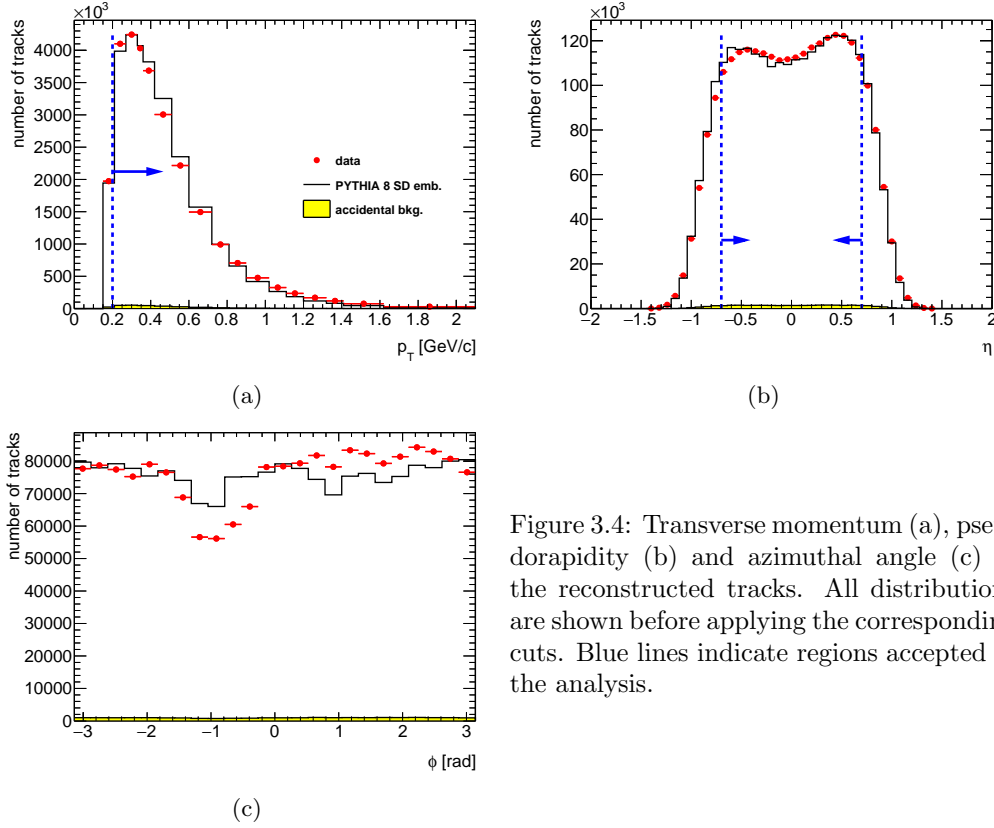
6

(a)

(b)

(c)

Figure 3.4: Transverse momentum (a), pseudorapidity (b) and azimuthal angle (c) of the reconstructed tracks. All distributions are shown before applying the corresponding cuts. Blue lines indicate regions accepted in the analysis.

without identification are required to have $p_{\mathrm{T}} > 0.2$ GeV/c and $|\eta| < 0.7$ due to high track reconstruction and TOF matching efficiencies in this region. For the identified particle-antiparticle ratio analysis, where in addition to charged pions, charged kaons and (anti)proton are measured, the p_T cut was increased to 0.3 and 0.4 GeV/c, respectively. The distributions of the DCA_{xy}, $|\mathrm{DCA}_z|$, d_0, $N_{\mathrm{hits}}^{\mathrm{fit}}$ and $N_{\mathrm{hits}}^{\mathrm{dE/dx}}$ quatities together with applied cuts are shown in Fig. 3.3, while the p_T, η and the azimuthal angle, ϕ, of the reconstructed tracks are shown in Fig. 3.4. Data are compared to embedded PYTHIA 8 SD sample.

3.3 Fiducial Region of the Measurement

A fiducial phase space of measurement is defined by the following criteria. Primary charged particles are defined as charged particles with a mean lifetime $\tau > 300$ ps, either directly produced in pp interaction or from subsequent decays of directly produced particles with $\tau < 30$ ps. In this analysis, the results are corrected to the region of the total number of primary charged particles (without identification), $2 \leq n_{\mathrm{ch}} \leq 8$. These primary charged particles had to be contained within the kinematic range of $p_{\mathrm{T}} > 0.2$ GeV/c and $|\eta| < 0.7$. In identified charged antiparticle to particle ratio measurement, the lower transverse momentum limit was changed for the analyzed particles as follows: 0.2 GeV/c (pions), 0.3 GeV/c (kaons), 0.4 GeV/c (protons and antiprotons)

The measurements were performed in a fiducial phase space of the forward scattered protons of $0.04 < -t < 0.16$ GeV^2/c^2 and $0.02 < \xi < 0.2$. Figure 3.5 shows that the efficiency to events containing at least two primary charged particles, $\epsilon_{n_{\mathrm{ch}} \geq 2}(\log_{10} \xi)$, is smaller than 50% for events with $\xi < 0.02$ and for this reason the lower ξ cut was introduced. All measured observables are presented in three ξ regions: $0.02 < \xi < 0.05$, $0.05 < \xi < 0.1$ and $0.1 < \xi < 0.2$.

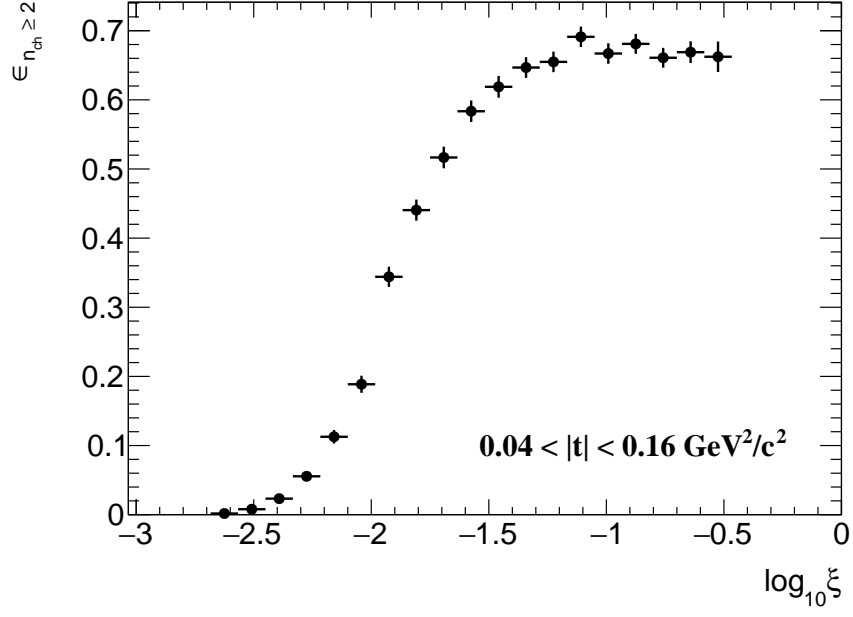Figure 3.5: $\epsilon_{n_{\mathrm{ch}} \geq 2}$ as a function of $\log_{10} \xi$ calculated from PYTHIA 8 (MBR).

4. Background Contribution

The background contribution to the charged-particle distributions can be broken down into event-level and track-level backgrounds, which are described in detail in the following sections:

- Accidental background refers to events which do not originate from a single collision of two protons.

- Track backgrounds from non-primary tracks consist of secondary tracks and fake tracks; the first come mostly from decays, the short-lived particles with mean life $30 < \tau < 300$ ps, or secondary interactions with the detector dead material, while the second comes from the track reconstruction algorithms and out-of-time pile-up with no corresponding true particles.

4.1 Accidental Background

The accidental backgrounds (same bunch pile-up background) are quantified using data-driven method and defined as a process where in one bunch crossing there is coincidence of two inter-actions, where any single-side proton signal is collected in coincidence with a signal in the TPC-TOF detector. This type of background may come from the overlap of a signal in RP (proton from beamhalo, low mass SD process without activity in TOF, elastic or low mass Central Diffraction (CD) processes with undetected proton on the other side) with a signal in TPC+TOF (mainly Non-Diffraction (ND) events without forward proton).

The accidental background contribution was calculated from Zerobias data, where two signatures of such background were investigated: the reconstructed proton in RP and the reconstruction of vertex from TPC tracks. The analysis was done for each RP arm separately and thus the Zerobias data was firstly required to pass the following criteria:

1. no trigger in any RP or trigger in exactly one arm (two RPs) with exactly one reconstructed proton track in that arm,

2. veto on any signal in small BBC tiles or ZDC on the same side of the IP as RP under consideration,

3. no reconstructed vertex or exactly one vertex with at least two TOF-matched tracks passing the quality criteria. The latter includes also signal in BBC small tiles on the opposite side of the IP to the RP under study.

The sample of selected Zerobias data with total number of events N was divided into four classes:

$$N = N(P,S) + N(R,S) + N(P,T) + N(R,T) \tag{4.1}$$

where: $N(P,S)$ is the number of events with reconstructed proton in exactly one RP and reconstructed vertex, $N(R,S)$ is the number of events with no trigger in any RP and reconstructed vertex, $N(P,T)$ is the number of events with reconstructed proton in exactly one RP and no reconstructed vertex, $N(R,T)$ is the number of events with no trigger in any RP and no reconstructed vertex.

Since the signature of the signal is a reconstructed proton in exactly one RP and a reconstructed vertex, the number of such events can be expressed as:

$$N(P,S) = N\left(p_3 + p_1 p_2\right) \tag{4.2}$$

where: p_1 is the probability that there is a reconstructed proton in RP and there is no reconstructed vertex, p_2 is the probability that there is no reconstructed proton in RP and there is a reconstructed

vertex, p_3 is the probability that there is a reconstructed proton in RP and there is a reconstructed vertex (not accidental).

The other classes of events given in Eq. (4.1) can be expressed in terms of the above probabilities as:

$$\begin{aligned}
N(R,S) &= N(1-p_1)p_2(1-p_3) \\
N(P,T) &= N(1-p_2)p_1(1-p_3) \\
N(R,T) &= N(1-p_1)(1-p_2)(1-p_3)
\end{aligned} \tag{4.3}$$

Finally, the accidental background contribution $A_{\text{bkg}}^{\text{accidental}}$ is given by:

$$A_{\text{bkg}}^{\text{accidental}} = \frac{p_1 p_2}{p_3 + p_1 p_2} = \frac{N(R,S)N(P,T)N}{N(R)N(T)N(P,S)} \tag{4.4}$$

where: $N(R) = N(R,S) + N(R,T)$ and $N(T) = N(P,T) + N(R,T)$.

The shapes of the accidental background related to TPC distributions come from the above Zerobias data events which pass all the analysis selection except having no trigger in any RP. The templates corresponding to RP distributions are from protons in the above data sets but with no reconstructed vertex. The normalization is given by Eq. (4.4). Figure 4.1 shows distributions of the reconstructed ξ with the accidental background contribution for events with proton reconstructed in WU and WD arms.
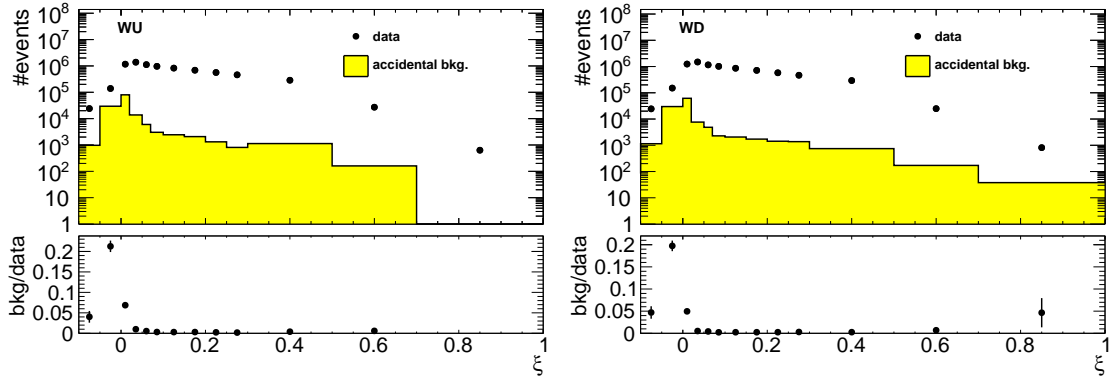

Figure 4.1: Uncorrected distributions of the reconstructed ξ for events with proton reconstructed in (left) WU and (right) WD arms. Data is shown as black markers, whereas the accidental background contribution is shown as yellow histogram. The ratio of accidental background and data is shown in the bottom pad.

The selection of Zerobias events, which is arbitrary and mainly driven by the selection of the signal, may provide some bias to the normalization of the accidental background. As a systematic check, two criteria for Zerobias selection were changed to:

1. no trigger in any RP or trigger in exactly one arm (two RPs) with *no more* than one reconstructed proton track in that arm,

2. no reconstructed vertex or exactly one vertex (*without any additional requirements*). The requirement of signal in BBC small tiles remains unchanged.

As a result of this change in the procedure, as shown in Fig. 4.2, the accidental background normalization increases of about 50% with respect to the nominal value. Therefore, the background changes by ±50% was taken as a systematic uncertainty related to the accidentals.
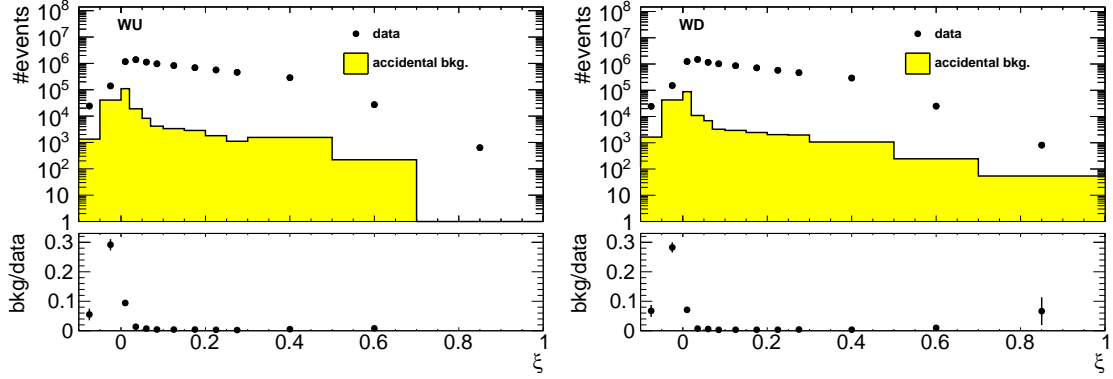
Figure 4.2: Uncorrected distributions of the reconstructed ξ for events with proton reconstructed in (left) WU and (right) WD arms. The accidental background contribution calculated with changed Zerobias selection criteria is also shown.

4.2 Background from Non-Primary Tracks

Reconstructed tracks matched to a non-primary particle, so-called background tracks, originate mainly from the following sources:

- decays of short-lived primary particles with strange quark content (mostly K^0, Λ^0),

- photons from π^0 and η decays which are converting to $e^+ e^-$,

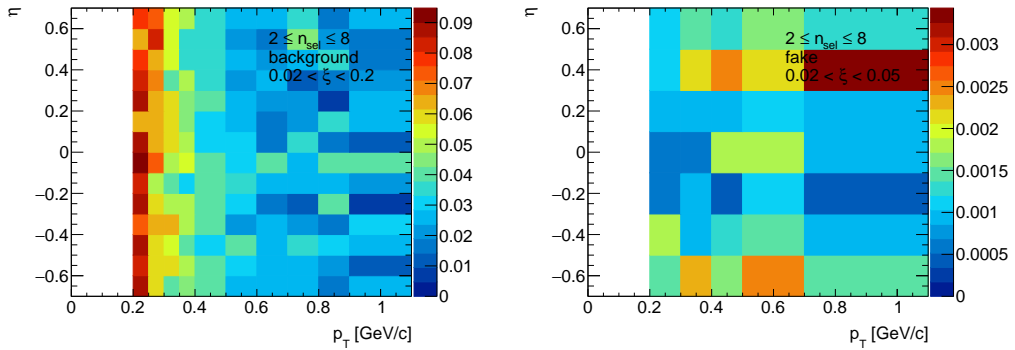- hadronic interactions of particles with the beam-pipe or detector dead material.

Figure 4.3: (left) Distribution of fraction of selected tracks associated with non-primary particles in the range $0.02 < \xi < 0.2$ and (right) distribution of fraction of tracks which are not associated with true-level particles in the range $0.02 < \xi < 0.05$.

There is also a contribution from fake tracks, i.e. tracks not associated with true-level particles, coming from out-of-time pile-up or formed by a random combination of TPC hits. Figure 4.3 shows the background $f_{\mathrm{bkg}}(p_{\mathrm{T}}, \eta)$ and fake track $f_{\mathrm{fake}}(p_{\mathrm{T}}, \eta)$ contribution to reconstructed tracks as a function of p_{T} and η. There were no differences observed in the background contribution in different ξ ranges, hence, all three ξ ranges were merged for this study. The highest background fraction, which varies between $5 - 10\%$, was found to be at low p_{T}. Due to too low statistics in PYTHIA 8 embedding MC, the shape of the fake track contribution was assumed to be the same in all three ξ ranges. However, its normalization was calculated for each ξ range separately with a ratio between the ranges of $1 : 0.74 : 1.11$. The change by $\pm 100\%$ in fake track contribution was taken as a systematic uncertainty.

Proton Background

Secondary particles can be created due to the interaction of particles with detector dead-material. The proton sample contains background from such protons knocked out from the detector materials [10]. Most of these protons have large DCA to the primary vertex and are not associated with the primary vertex. However, the protons with small DCA are included in the primary track sample. Antiprotons do not have knockout background, hence the DCA tail is almost absent in their DCA distributions.

The fraction of knock-out background protons depends on a number of factors, including the amount of detector material, analysis cuts and the ξ of diffractive proton. While it is natural to calculate the fractions of primary and background protons in the MC sample, the MC models do not necessarily predict the fraction of knock-out background protons correctly. Hence, other data-driven methods must be used to calculate this type of background.
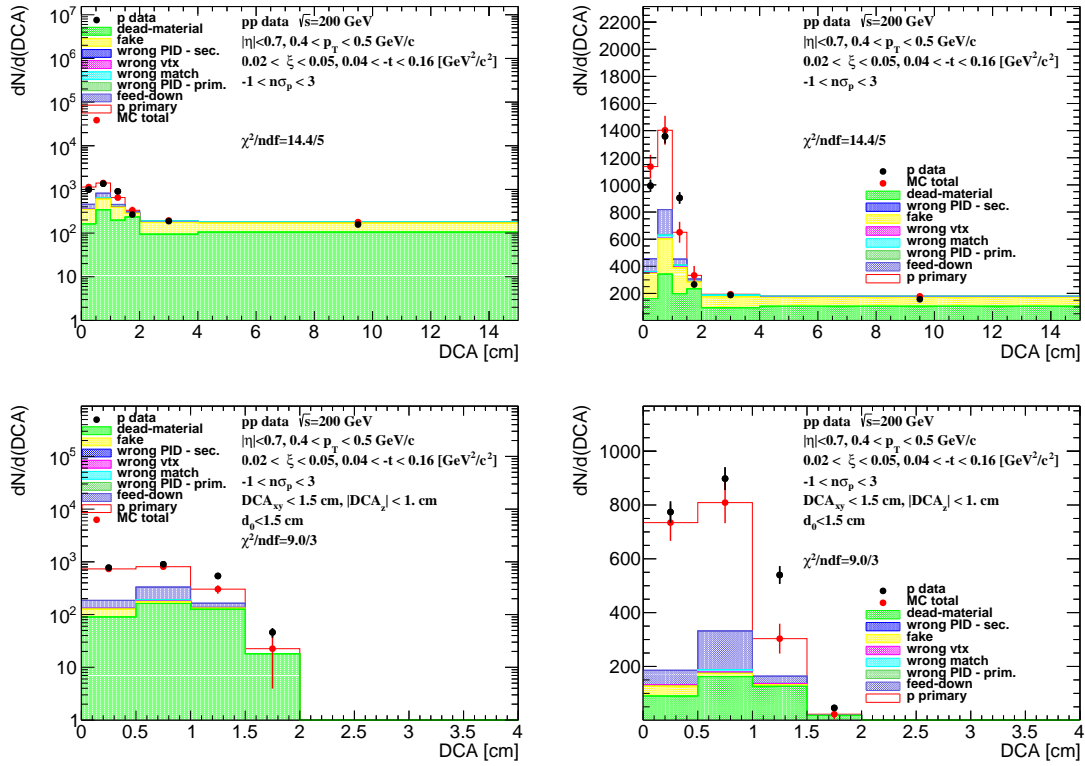

Figure 4.4: The DCA distributions of protons for $0.4 < p_T < 0.5$ GeV/c shown for single range of $0.02 < \xi < 0.05$ (shown in log and linear scale in left and right column, respectively). The MC contributions are shown after scaling the dead-material template to data. (top) Background enriched samples were used in the normalization procedure, whereas (bottom) the proton background was estimated from the nominal sample.

In order to correct for the knock-out background protons, sample enriched in proton background was used for background normalization, where DCA_{xy}, DCA_z and d_0 cuts were abandoned. Additionally, at least one, instead of exactly one, reconstructed vertex was allowed in this sample. Figures 4.4 and 4.5 show the DCA distributions of protons and antiprotons, respectively, for nominal (bottom) and background enriched (top) samples. The distributions for other p_T and ξ regions are shown in Appendix B. The protons and antiprotons are selected by a dE/dx cut of $-1 < n\sigma_{p,\bar{p}} < 3$ where $n\sigma_{p,\bar{p}}$ is given by Eq. (8.10). The fraction of knock-out protons within the selected sample is determined via MC template fits. The templates of reconstructed tracks with

dE/dx corresponding to the proton and antiproton are obtained from PYTHIA 8 embedding MC separately for:

- primary (anti)protons,

- knock-out background protons (labeled as dead-material),

- fake tracks,

- secondary particles with dE/dx of (anti)proton (labeled as wrong PID - sec.),

- tracks associated with primary (anti)protons, but with the reconstructed vertex not matched to true-level primary vertex (labeled as wrong vtx),

- reconstructed track is partially matched to true-level particle (labeled as wrong match, track to true-level particle matching is described in [1], i.e. track and true-level particle have appropriate number of common hit points but the distance between true-level particle and track is too large, $\delta^2(\eta, \phi) > (0.15)^2$,

- primary particles with dE/dx of (anti)proton (labeled as wrong PID - prim.),

- (anti)proton as a product of short-lived decays, mainly Λ^0 (labeled as feed-down).

First, the background enriched sample was used (Fig. 4.4, top), where the template of knock-out background protons was normalized to the number of events in the fake-subtracted tail of the DCA distribution, $2 < \text{DCA} < 15$ cm. Next the knock-out proton and fake background was subtracted from the DCA distribution and the sum of other templates was normalized to the number of events in the signal region, DCA < 1.5 cm.

The fraction of the knock-out proton background in the signal region, DCA < 1.5, was estimated from the nominal sample (Fig. 4.4, bottom), where DCA_{xy}, DCA_z and d_0 track cuts were applied and exactly one reconstructed vertex was required. The normalization of each MC contribution was kept the same as that estimated for the background enriched sample. Figure 4.6 shows the knock-out proton background as a function of p_T in three ranges of ξ. The following functional form was found to describe the background protons:

$$f_{\text{bkg}}^p(p_T) = p_0 \exp(p_1 p_T) \tag{4.5}$$

where p_0 and p_1 are free parameters obtained from a fit.

The obtained fraction of knock-out background protons is approximately 20% at $p_T = 0.45$ GeV/c and less than 10% at $p_T = 1.0$ GeV/c.

Figure 4.5 shows the corresponding DCA distributions with MC templates for antiprotons, where the background from knock-out particles is not present. Therefore, there was no need for any fit to be performed in this comparison. The MC templates fairly well describe the DCA distribution for both, protons, after tunning the fraction of knock-out background to data, and antiprotons. Additionally, there is a small ($< 1\%$) background contribution, present for both particles, which also was taken into account and subtracted. It originates from reconstructed tracks which have the appropriate number of common hit points with true-level particle, but the distance between them is too large, i.e. $\delta^2(\eta, \phi) > (0.15)^2$.

Systematic Uncertainty Related to Proton Background

The knock-out proton background estimation introduces systematic uncertainties. First, the normalization interval of the knock-out proton background template in the background enriched sample was changed to $4 < \text{DCA} < 15$ cm. This introduced a relative systematic uncertainty of up to 30% for $p_T \approx 1.0$ GeV/c.

The knock-out proton background contribution was parameterized as it is shown in Eq. (4.5). The systematic uncertainty related to the fit procedure was estimated by varying the parameters,
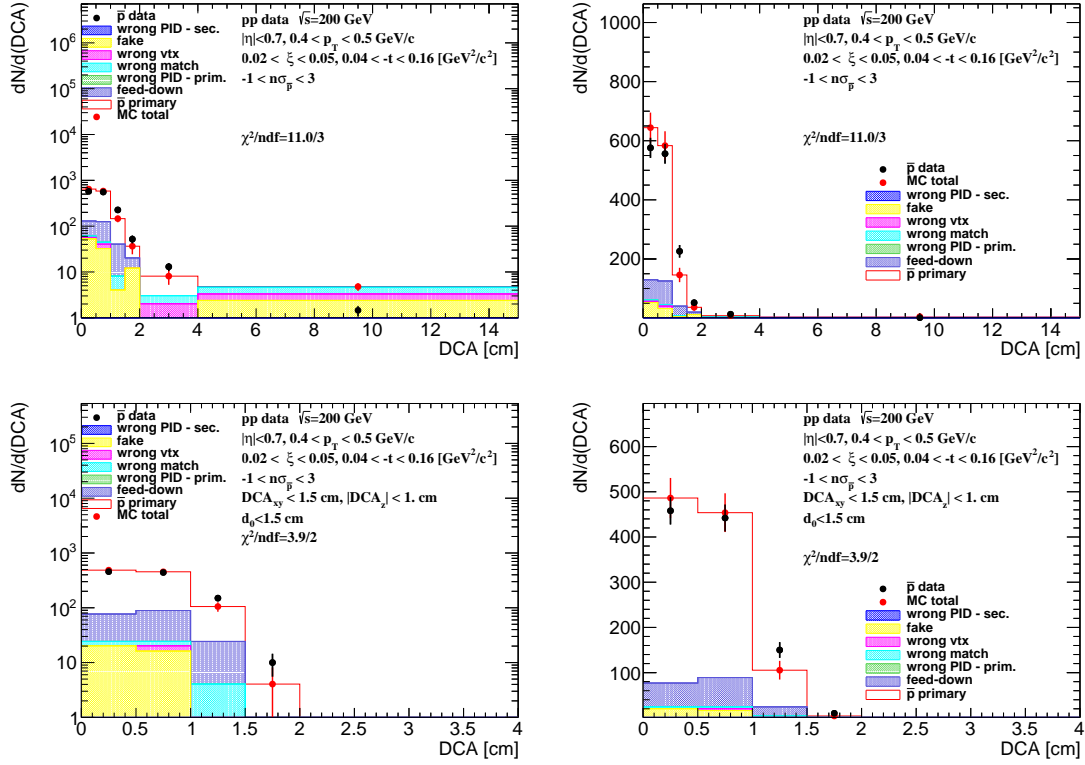
Figure 4.5: The DCA distributions of antiprotons for $0.4 < p_{\mathrm{T}} < 0.5$ GeV/c shown for one range of $0.02 < \xi < 0.05$ (log and linear scale in left and right column, respectively). The MC controbutions are shown as colour histograms. (top) Background enriched and (bottom) nominal samples were used.

p_0 and p_1, by their statistical uncertainties ($\pm 1\sigma$). As a result, a relative systematic uncertainties of about 10% were obtained.

Differences in the shape of the DCA distribution between data and MC can affect the knock-out proton background estimation procedure. Figure 4.7 (top left) shows the data to MC ratio of the number of events in the background dominated region, $2 < \mathrm{DCA} < 15$ cm. Since this region is used to estimate background normalization, and the shape of the DCA distribution in the data differs from that observed in the simulation, the predicted background in the DCA < 1.5 cm region can change. Thus, the following functional form was used to estimate the slope between data and MC:

$$\frac{\mathrm{data}}{\mathrm{MC}}(\mathrm{DCA}) = A(\mathrm{DCA} - 8.5) + B \tag{4.6}$$

where A (slope) and B are fit free parameters. Differences in slope between data and MC were used to estimate how many more tail-like tracks would fit into the signal region and a systematic uncertainty, which varies up to 5% for $0.02 < \xi < 0.05$, was introduced.

All above components of the systematic uncertainty related to the knock-out proton background, shown in Fig. 4.7, are added in quadrature. Those related to the fit range and the shape of the proton background are symmetrized.
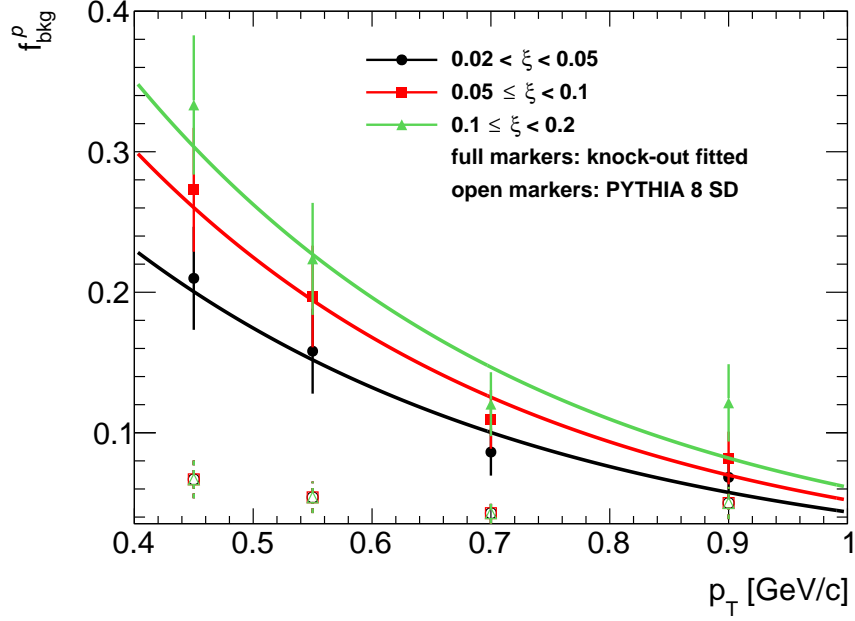
14

Figure 4.6: The fraction of knock-out proton background as a function of p_T in three ranges of ξ with fitted parametrizations. Full markers represent fitted knock-out background and open markers represent PYTHIA 8 SD predictions.
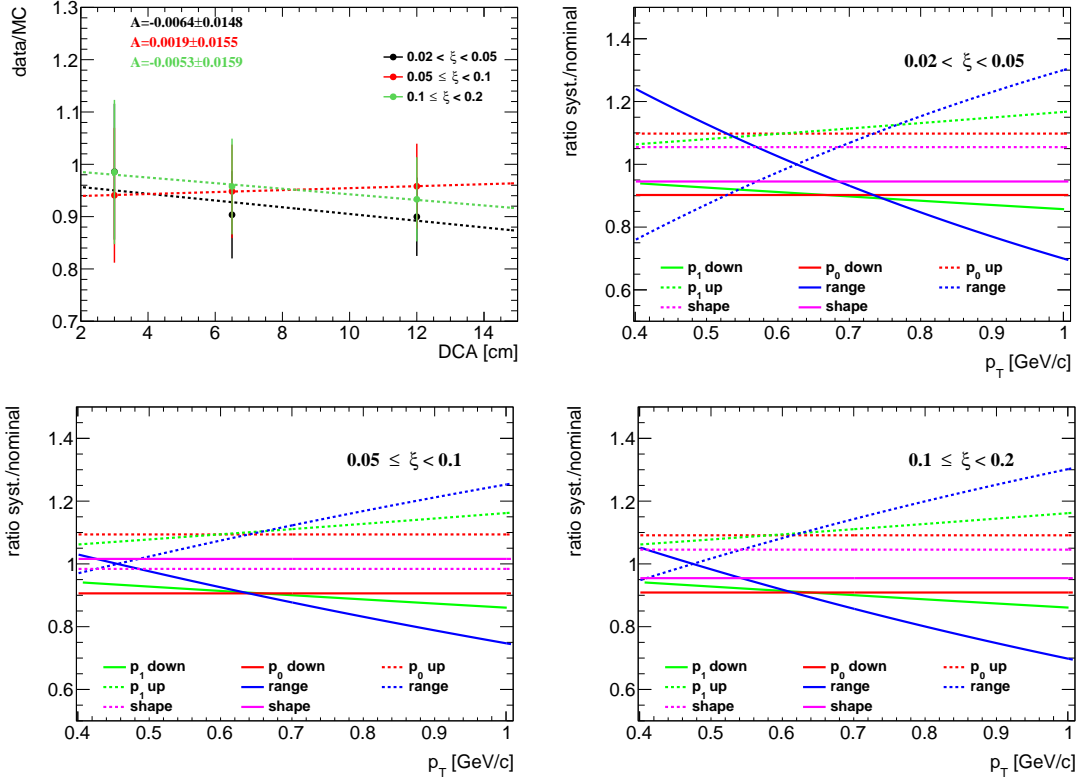

Figure 4.7: (top left) Data to MC ratio of the number of events in the background dominated region in three ranges of ξ with fitted functional form given by Eq. (4.6). (top right and bottom) Components of the systematic uncertainty related to the knock-out background protons contribution in three ξ ranges.

15

Pion Background

The pion spectra are corrected for weak decays (mainly of K_S^0 and Λ^0), muon contribution and background from the detector dead-material interactions. The pion decay muons can be identified as pions due to the similar masses. These contributions are obtained from PYTHIA 8 SD. Figure 4.8 shows the background contribution to the pion spectra as a function of p_T in three ranges of ξ, separately for π^- and π^+. Since there were negligible differences observed between these three ranges of ξ, the background contribution was averaged over ξ. The following parametrization was found to describe it:

$$f_{\text{bkg}}^{\pi}(p_T) = a_0 \exp(a_1 p_T) + a_2 p_T^2 + a_3 p_T \tag{4.7}$$

where a_i, $i = 0, \ldots, 3$ are free paramaters of the fitted function.

The pion background contribution varies between 5% at low-p_T ($p_T = 0.25$ GeV/c) and about 1% at $p_T = 1.0$ GeV/c for both negatively and positively charged pions. In addition, the background was calculated from EPOS SD+SD$'$ for the full range of ξ. The differences between PYTHIA 8 and EPOS are up to 1% for π^-.
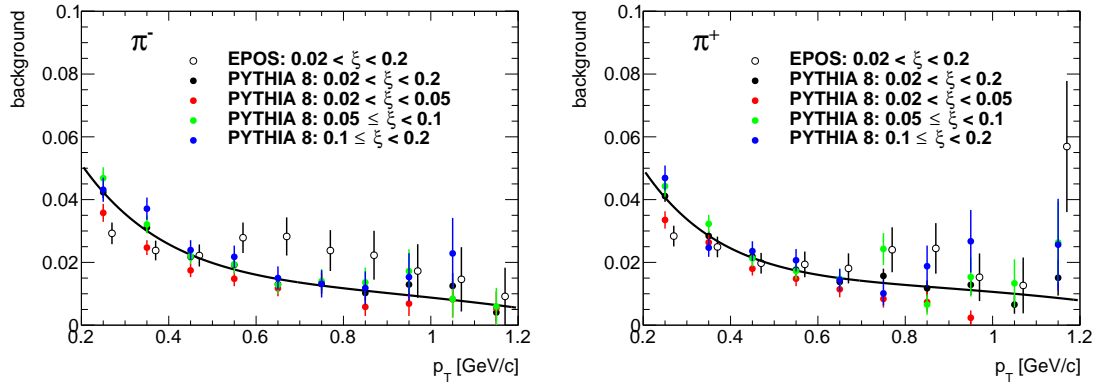

Figure 4.8: Pion background fraction as a function of p_T calculated from PYTHIA 8 and shown separately for (left) negatively and (right) positively charged pions in three ranges of ξ: (red) $0.02 < \xi < 0.05$, (green) $0.05 < \xi < 0.1$, (blue) $0.1 < \xi < 0.2$. (full black points) The pion background averaged over three ranges of ξ with fitted parametrization is also shown. Open black points represent EPOS predictions for the full ξ range.

5. Non-SD Contributions

The contributions coming from ND, Double Diffractive (DD) and CD events are estimated from MC models, where forward proton and reconstructed vertex are the result of the same pp interaction. Tracks reconstructed in RPs which are modeled in the MC simulations are only coming from:

- forward protons produced in the SD, CD or DD diffractive systems or from ND events,

- secondary particles from showering initiated by interaction of forward protons with beam-line elements.

Figure 5.1 shows the uncorrected ξ and t distributions in data compared to various MC models: PYTHIA 8 A2 (MBR), PYTHIA 8 A2 (MBR-tuned) and EPOS. The MC distributions are split into SD, ND, DD and CD components. For EPOS, SD$'$ is separated from the ND events. Additionally, the accidental background is also shown. PYTHIA 8 A2 (MBR-tuned) predictions agree much better with the data than PYTHIA 8 A2 (MBR) and result also in a suppression of non-SD events. EPOS describes data better than PYTHIA 8 but shows a dominant contribution of SD$'$ events. All MCs predict significant DD and ND background at large ξ, thereby the analysis was limited to $\xi < 0.2$.

On the other hand, Figs. 5.2 to 5.4 show the uncorrected distributions of variables used in the later analysis: n_{sel}, p_{T} an $\bar{\eta}$. The background contributions from non-SD interactions differ a bit between each other, i.e. EPOS predicts significantly larger CD contribution, whereas DD and ND are suppressed in PYTHIA 8 A2 (MBR-tuned). As a result PYTHIA 8 A2 (MBR) is used as the default model of non-SD with systematic uncertainty $\pm 50\%$, which covers all differences between the models.
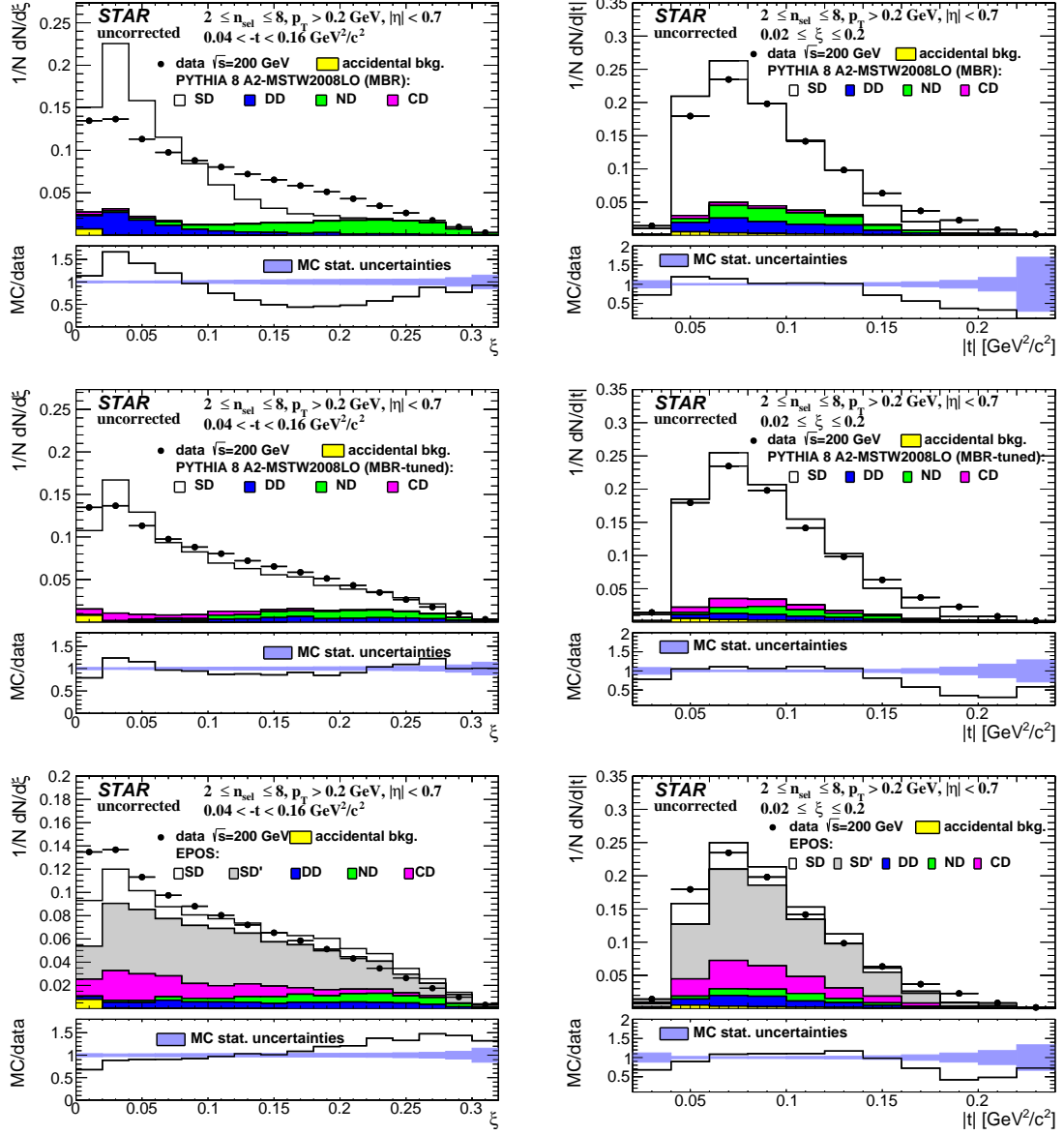
Figure 5.1: Uncorrected distributions of data compared to various MC models: (top) PYTHIA 8 A2 (MBR), (middle) PYTHIA 8 A2 (MBR-tuned) and (bottom) EPOS, as a function of (left column) ξ and (right column) $|t|$.
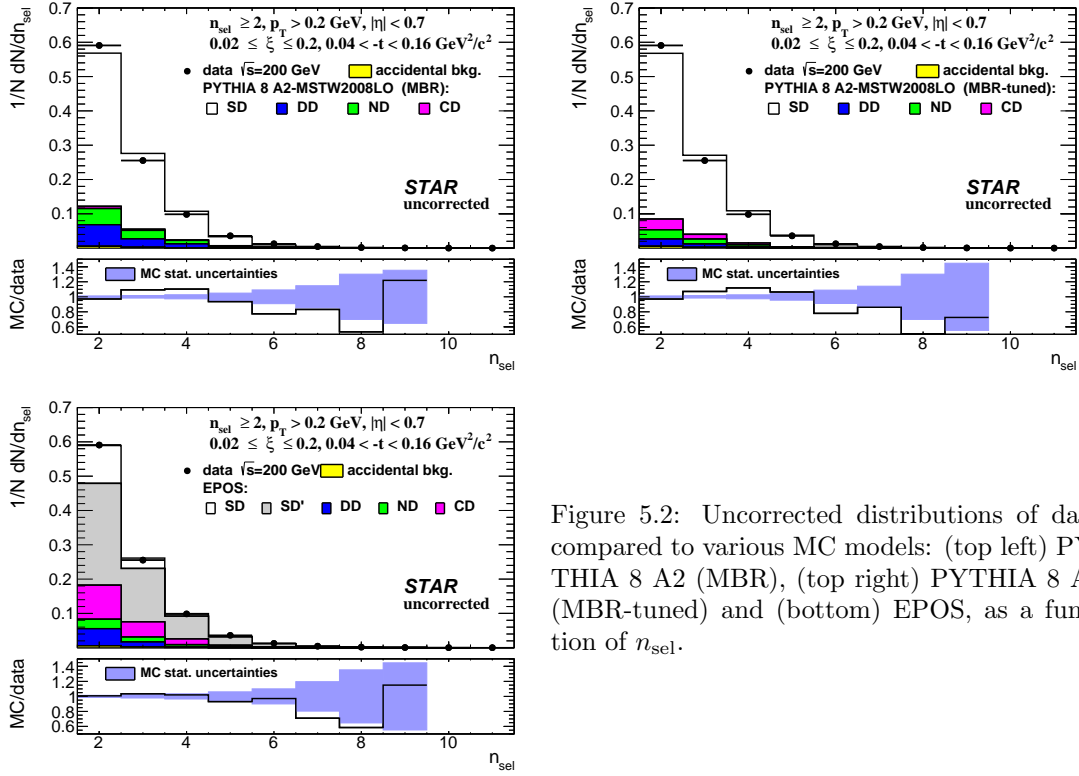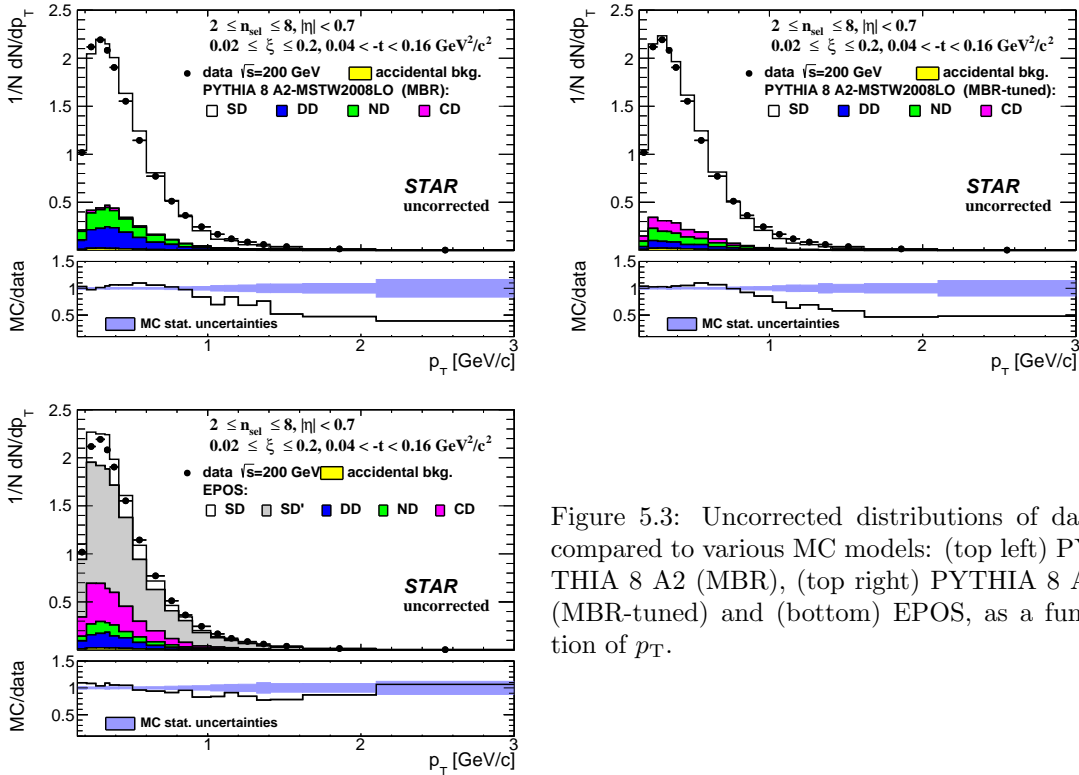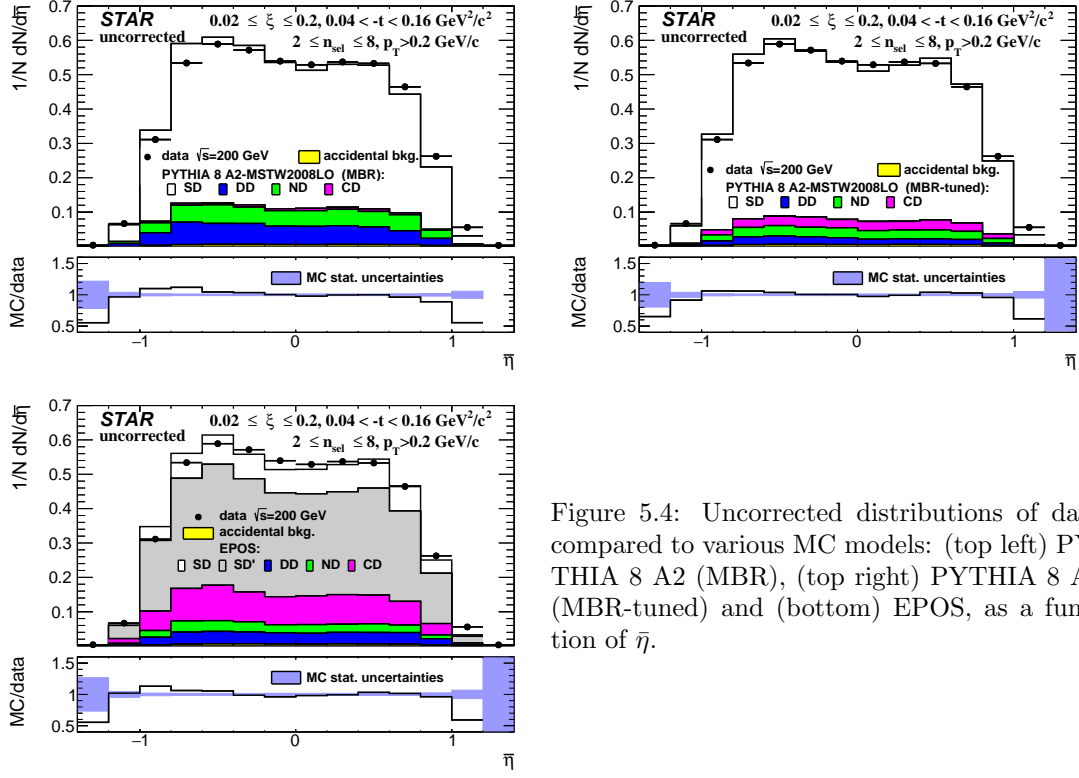
Figure 5.2: Uncorrected distributions of data compared to various MC models: (top left) PYTHIA 8 A2 (MBR), (top right) PYTHIA 8 A2 (MBR-tuned) and (bottom) EPOS, as a function of $n_{\rm sel}$.

Figure 5.3: Uncorrected distributions of data compared to various MC models: (top left) PYTHIA 8 A2 (MBR), (top right) PYTHIA 8 A2 (MBR-tuned) and (bottom) EPOS, as a function of $p_{\rm T}$.

Figure 5.4: Uncorrected distributions of data compared to various MC models: (top left) PYTHIA 8 A2 (MBR), (top right) PYTHIA 8 A2 (MBR-tuned) and (bottom) EPOS, as a function of $\bar{\eta}$.

6. Selection Efficiencies

6.1 Vertex Reconstruction

In pp collisions, where the charged-particle multiplicity is low, the vertex finding algorithm sometimes fails to find the primary vertex. In addition, at high luminosity, vertex finder can fail due to the contribution of pile-up events and providing a wrong reconstructed vertex. In the study of vertex reconstruction efficiency we required at least two reconstructed global tracks $n_{\text{sel}}^{\text{global}} \geq 2$ passing all the quality cuts listed in Sec 3.2 but without DCA_{xy} and DCA_z cuts and associated to a true-level primary particles. Additionally, MC events were accepted if the z-coordinate of the true-level primary vertex was between -80 and 80 cm and $n_{\text{ch}} \geq 2$. All corrections, described in this section, were calculated in three ranges of ξ separately using PYTHIA 8 SD embedding MC.

The global tracks (not necessarily associated to a true-level primary particles), which are used by the vertex-finder algorithm, had to pass the following quality cuts:

1. Tracks must be matched with hits reconstructed in TOF,

2. The number of the TPC hits used in the helix fit $N_{\text{hits}}^{\text{fit}}$ must be greater than 20,

3. The ratio of the number of TPC hits used in the helix fit to the number of possible TPC hits $N_{\text{hits}}^{\text{fit}}/N_{\text{hits}}^{\text{poss}}$ must be greater than 0.52,

4. The transverse impact parameter with respect to the beamline d_0 must be less than 2 cm,

5. The track's transverse momentum p_{T} must be greater than 0.2 GeV/c.

The above track selection criteria are different than those used in the analysis. Thus, primary vertex reconstruction efficiency and fake vertex rate were calculated as a function of the number of global tracks used in vertexing $n_{\text{vrt}}^{\text{global}}$ instead of $n_{\text{sel}}^{\text{global}}$.

In the analysis exactly one vertex with $n_{\text{sel}} \geq 2$ is required. However, in the study of vertex reconstruction, events with additional vertices were allowed. Therefore, we define the best vertex as the reconstructed vertex with the highest number of TOF-matched tracks. This vertex does not have to be associated to true-level primary vertex. The algorithm, which matches reconstructed vertices to true-level vertices, checks for reconstructed tracks originating from them. If at least one reconstructed track is assigned to a true-level particle, then the reconstructed vertex is assigned to the true-level vertex from which the true-level particle originates. Since the fake vertices (not matched to the true-level primary vertex) are allowed in the analysis, the overall vertex-finding efficiency, $\epsilon_{\text{vrt}}\left(n_{\text{vrt}}^{\text{global}}\right)$, is expressed as:

$$\epsilon_{\text{vrt}}\left(n_{\text{vrt}}^{\text{global}}\right) = \epsilon_{\text{vrt}}^{\text{best}}\left(n_{\text{vrt}}^{\text{global}}\right) + \delta_{\text{vrt}}^{\text{fake}}\left(n_{\text{vrt}}^{\text{global}}\right) \tag{6.1}$$

where:

$\epsilon_{\text{vrt}}^{\text{best}}\left(n_{\text{vrt}}^{\text{global}}\right)$ is the primary vertex reconstruction efficiency, determined as the ratio of the number of good reconstructed events (reconstructed best primary vertex with $n_{\text{sel}} \geq 2$ and matched to the true-level primary vertex) to the number of input MC events,

$\delta_{\text{vrt}}^{\text{fake}}\left(n_{\text{vrt}}^{\text{global}}\right)$ is the fake vertex rate, determined as the ratio of the number of good reconstructed events (reconstructed best primary vertex with $n_{\text{sel}} \geq 2$ and not matched to the true-level primary vertex) to the number of input MC events. Due to the contribution of pile-up, it is possible that the best vertex originates from fake tracks instead of true-level particles.

The vertex-finding efficiency as a function of $n_{\mathrm{vrt}}^{\mathrm{global}}$ is shown in Fig. 6.1 (left). When there are exactly two global tracks used in the vertex reconstruction, $n_{\mathrm{vrt}}^{\mathrm{global}} = 2$, the vertex-finding efficiency depends on the longitudinal distance between these tracks $|\Delta z_0|$. Therefore, the vertex finding efficiency for such events $\epsilon_{\mathrm{vrt}}\left(|\Delta z_0|\right)$ is given by:

$$\epsilon_{\mathrm{vrt}}\left(|\Delta z_0|\right) = \epsilon_{\mathrm{vrt}}^{\mathrm{best}}\left(|\Delta z_0|\right) + \delta_{\mathrm{vrt}}^{\mathrm{fake}}\left(|\Delta z_0|\right) \tag{6.2}$$

where: $\epsilon_{\mathrm{vrt}}^{\mathrm{best}}\left(|\Delta z_0|\right)$ is the primary vertex reconstruction efficiency, $\delta_{\mathrm{vrt}}^{\mathrm{fake}}\left(|\Delta z_0|\right)$ is the fake vertex rate.

Figure 6.1 (right) shows the vertex finding efficiency for events with $n_{\mathrm{vrt}}^{\mathrm{global}} = 2$. This efficiency is smaller than 20% for tracks with $|\Delta z_0| > 2$ cm, hence the analysis was limited to events with $|\Delta z_0| < 2$ cm, when $n_{\mathrm{vrt}}^{\mathrm{global}} = 2$.
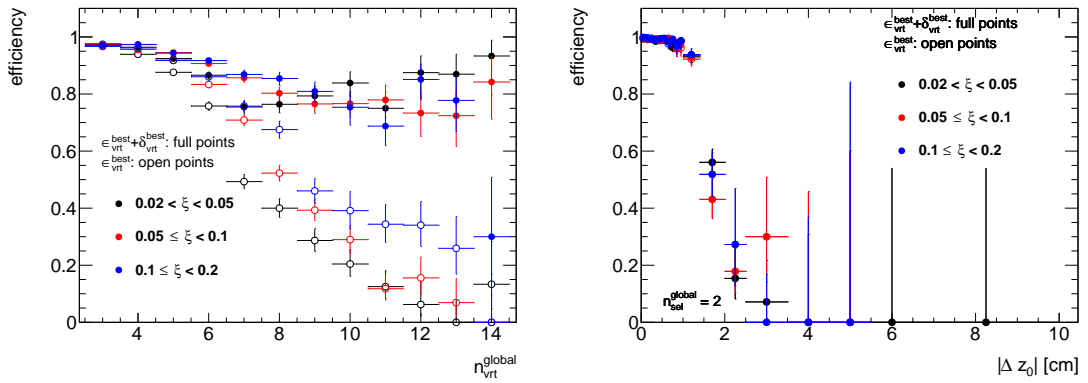
Figure 6.1: Vertex-finding efficiency in three ranges of ξ as a function of (left) $n_{\mathrm{vrt}}^{\mathrm{global}}$ and (right) with respect to the $|\Delta z_0|$ between reconstructed tracks in events with $n_{\mathrm{vrt}}^{\mathrm{global}} = 2$.

Events are rejected if additional vertices are reconstructed in addition to the best one. Rejected events can be classified as:

a) two or more additional vertices,

b) additional secondary vertex from interactions with the detector dead-material,

c) additional fake vertex,

d) additional primary vertex (vertex splitting or background vertex reconstructed as best vertex),

e) additional decay TOF vertex.

The correction for vetoing such events, $\epsilon_{\mathrm{vrt}}^{\mathrm{veto}}\left(n_{\mathrm{vrt}}^{\mathrm{global}}\right)$, is given by:

$$\begin{aligned}\epsilon_{\mathrm{vrt}}^{\mathrm{veto}}\left(n_{\mathrm{vrt}}^{\mathrm{global}}\right) &= 1 - \frac{\text{number of events with more than one reconstructed TOF vertex}}{\text{number of events with at least one reconstructed TOF vertex}} \\ &= 1 - \epsilon_a - \epsilon_b - \epsilon_c - \epsilon_d - \epsilon_e\end{aligned} \tag{6.3}$$

where $\epsilon_a - \epsilon_e$ are the fractions of events with additional vertices, whose labels are listed above.

As before, the correction was calculated as a function of $|\Delta z_0|$ for events with $n_{\mathrm{vrt}}^{\mathrm{global}} = 2$. Figure 6.3 shows the fraction of multi-vertex events with respect to the $n_{\mathrm{vrt}}^{\mathrm{global}}$. There is a large fraction of events ($> 90\%$) with additional background vertices for $n_{\mathrm{vrt}}^{\mathrm{global}} \geq 9$, what would result in large correction factor. Hence, the analysis was limited to events with $n_{\mathrm{sel}} \leq 8$. The total
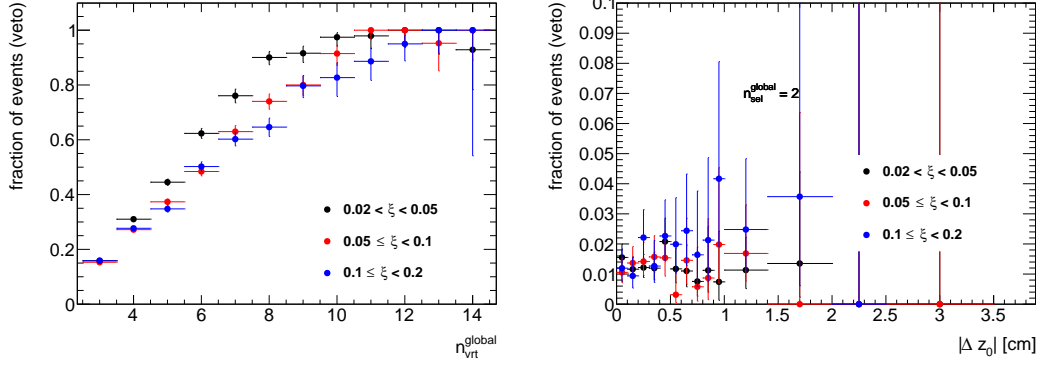
Figure 6.2: Total fraction of multi-vertex events as a function of (left) $n_{\mathrm{vrt}}^{\mathrm{global}}$ for events with $n_{\mathrm{vrt}}^{\mathrm{global}} > 2$ and (right) $|\Delta z_0|$ for events with $n_{\mathrm{vrt}}^{\mathrm{global}} = 2$ in three ranges of ξ.
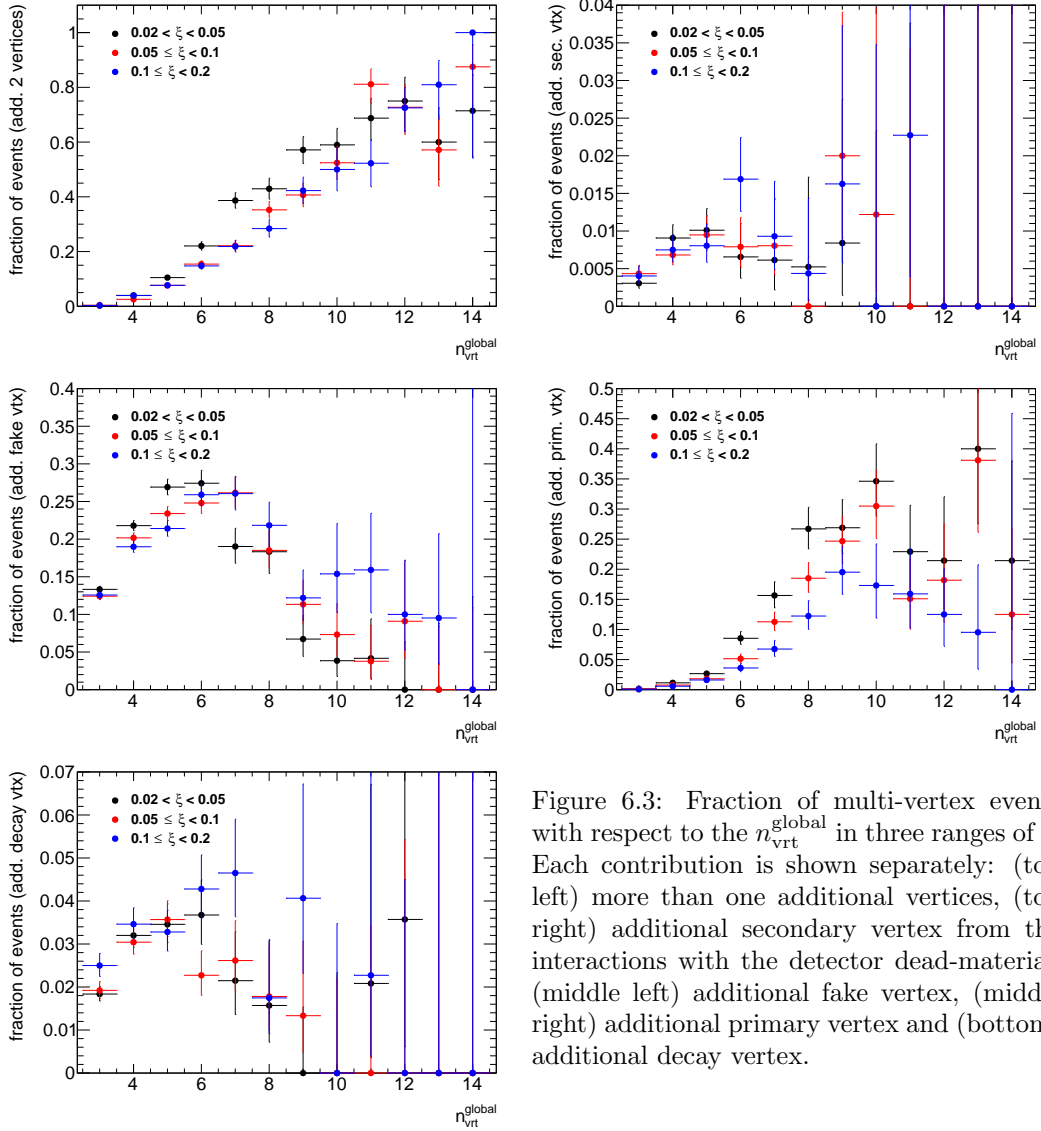

Figure 6.3: Fraction of multi-vertex events with respect to the $n_{\mathrm{vrt}}^{\mathrm{global}}$ in three ranges of ξ. Each contribution is shown separately: (top left) more than one additional vertices, (top right) additional secondary vertex from the interactions with the detector dead-material, (middle left) additional fake vertex, (middle right) additional primary vertex and (bottom) additional decay vertex.

fraction of multi-vertex events, $\epsilon_a + \epsilon_b + \epsilon_c + \epsilon_d + \epsilon_e$, as a function of $n_{\mathrm{vrt}}^{\mathrm{global}}$ and $|\Delta z_0|$, shown in Fig. 6.2, demonstrates that $\epsilon_{\mathrm{vrt}}^{\mathrm{veto}}(|\Delta z_0|)$ is very large ($> 98\%$) for events with $n_{\mathrm{vrt}}^{\mathrm{global}} = 2$.

Although, the analysis was limited to $n_{\mathrm{sel}} \leq 8$, a fraction of events with additional background vertices was still relatively large. Since most of these additional vertices are fake, it was checked whether the charged-particle multiplicity distributions are different for events with and without reconstructed fake vertices. These distributions, as shown in Fig 6.4, are in good agreement, thus, above studies of vertex reconstruction were repeated using MC events that do not contain reconstructed fake vertices. The vertex finding efficiency, which was calculated from such events, is shown in Fig. 6.5. It is greater than 95% for events with $2 \leq n_{\mathrm{vrt}}^{\mathrm{global}} \leq 8$. In addition, the corresponding fraction of multi-vertex events, shown in Figs. 6.6 and 6.7, is smaller than 20%. Since fake vertices were rejected from this study, the ϵ_c term from Eq. (6.3) is equal to 0.

The correction factors calculated from MC events that do not contain reconstructed fake vertices are relatively small, hence, they were used in the analysis instead of the one obtained from the full MC sample.
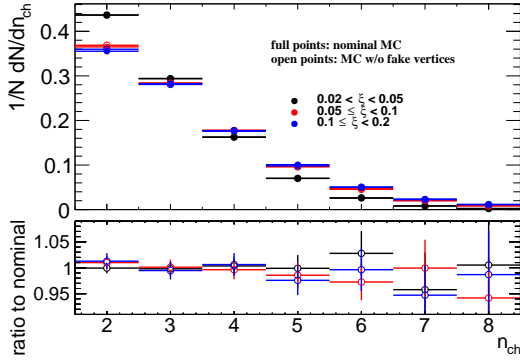
Figure 6.4: Charged-particle mulitplicity distributions in three ranges of ξ calculated from PYTHIA 8 SD embedding MC for (full points) all generated events and (open points) events without reconstructed fake vertices.
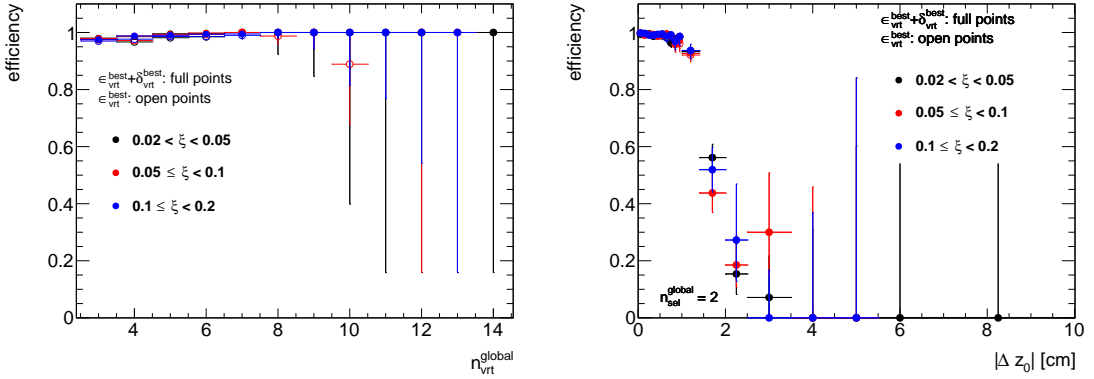

Figure 6.5: Vertex-finding efficiency in three ranges of ξ as a function of (left) $n_{\mathrm{vrt}}^{\mathrm{global}}$ and (right) with respect to the $|\Delta z_0|$ between reconstructed tracks in events with $n_{\mathrm{vrt}}^{\mathrm{global}} = 2$. Only events that do not contain fake vertices were used.
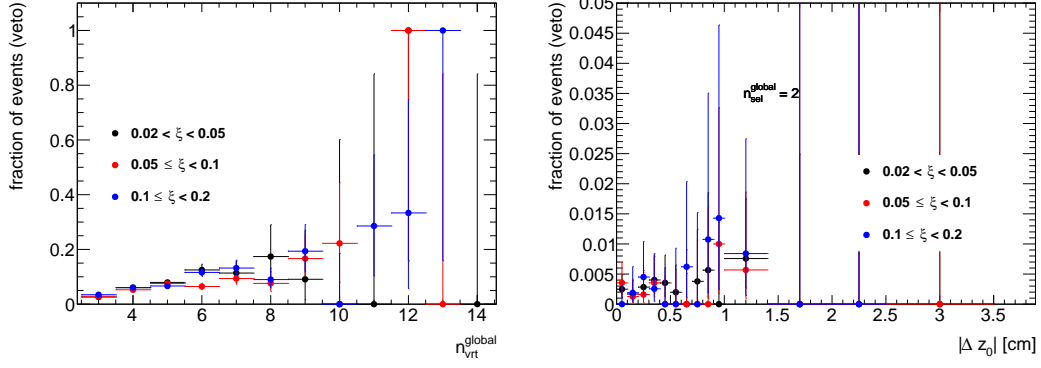
Figure 6.6: Total fraction of multi-vertex events as a function of (left) $n_{\text{vrt}}^{\text{global}}$ for events with $n_{\text{vrt}}^{\text{global}} > 2$ and (right) $|\Delta z_0|$ for events with $n_{\text{vrt}}^{\text{global}} = 2$ in three ranges of ξ. Only events that do not contain fake vertices were used.
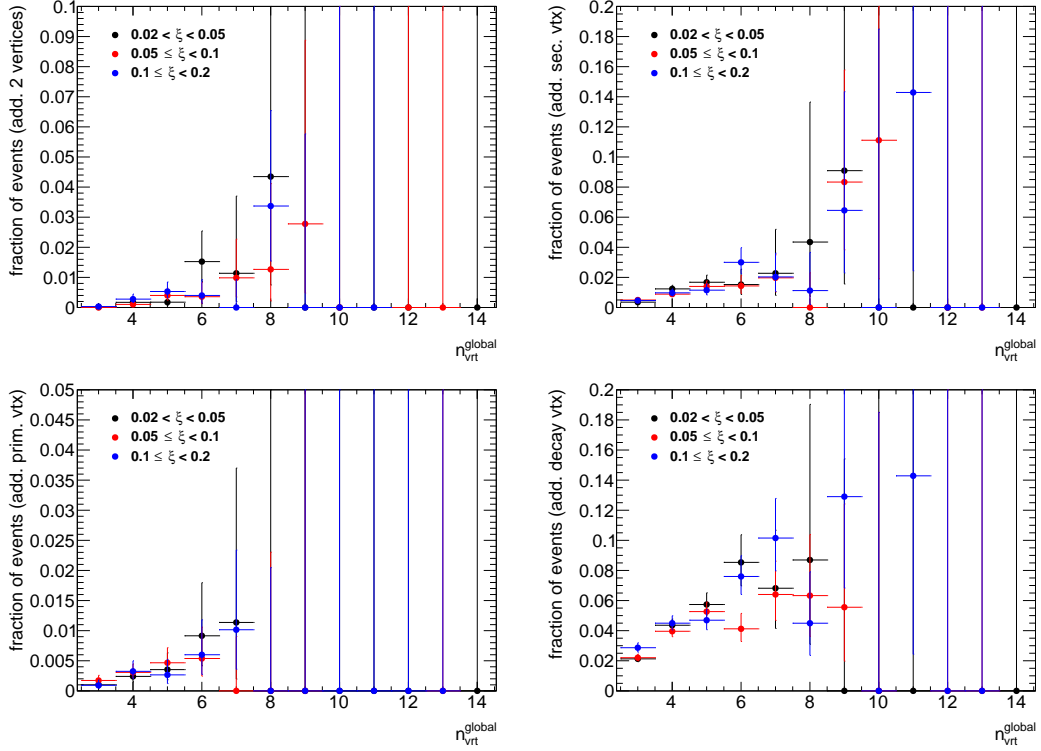

Figure 6.7: Fraction of multi-vertex events with respect to the $n_{\text{vrt}}^{\text{global}}$ in three ranges of ξ. Each contribution is shown separately: (top left) more than one additional vertices, (top right) additional secondary vertex from the interactions with the detector dead-material, (bottom left) additional primary vertex and (bottom right) additional decay vertex. Only events that do not contain fake vertices were used.

6.2 Correction to BBC-Small

The SDT trigger conditions imposed signal in RPs and veto on any signal in the same-side small BBC tiles, whereas signal in the opposite-side BBC-small was required by the offline event selection. These requirements were imposed in order to accept only events with rapidity gap and
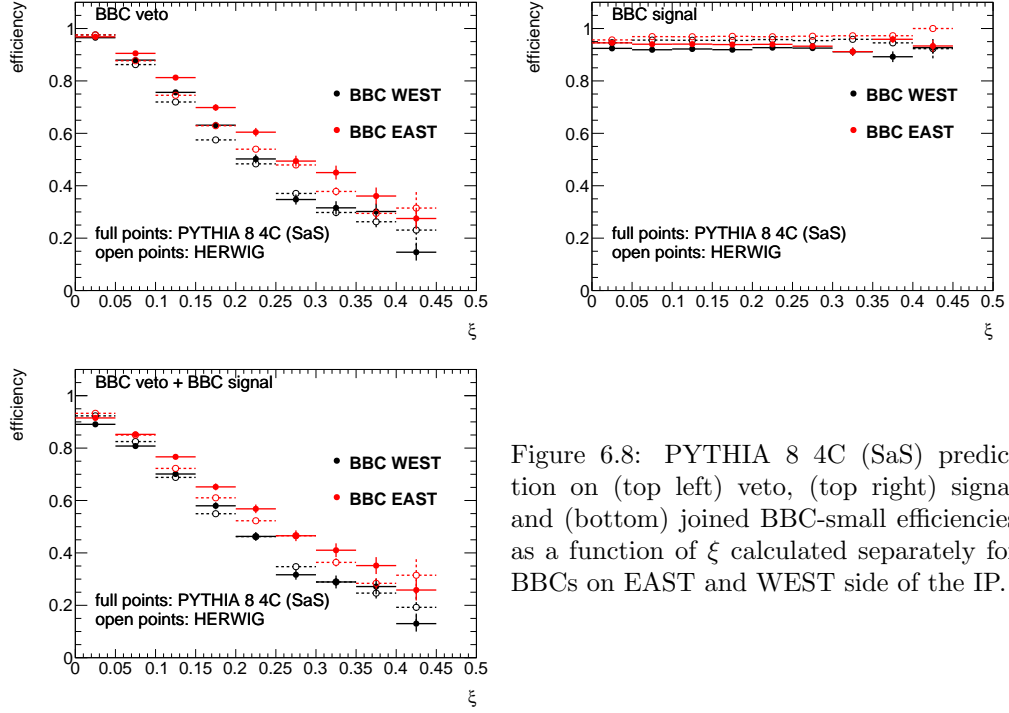
Figure 6.8: PYTHIA 8 4C (SaS) prediction on (top left) veto, (top right) signal and (bottom) joined BBC-small efficiencies as a function of ξ calculated separately for BBCs on EAST and WEST side of the IP.

reduce DD, ND and accidental backgrounds. A joined BBC-small efficiency, ϵ_{BBC}, was obtained as a function of each measured quantity using PYTHIA 8 4C (SaS) embedded into Zerobias data and HERWIG MC. The efficiency was calculated for events within fiducial region as follows:

$$\epsilon_{\mathrm{BBC}} = \frac{\text{number of MC events satysfying the BBC-small selection criteria}}{\text{number of MC events}} \quad (6.4)$$

Figures 6.9 to 6.11 show the fraction of generated true-level MC events, within the fiducial region of the measurement, in which the selection criteria on BBC-small signal and veto are fulfilled. In addition, veto, signal and joined BBC-small efficiencies are presented separately as a function of ξ in Fig. 6.8. The ϵ_{BBC} varies from about 90% for events with ξ within $0.02 - 0.05$ to about 60% for events with $0.1 < \xi < 0.2$.

Data is corrected for BBC-small efficiency using PYTHIA 8 4C (SaS). The uncertainty related to this correction is estimated by using HERWIG MC sample, where the hadronisation model is different from that used in PYTHIA 8. Figure 6.12 shows the PYTHIA 8 prediction on BBC efficiency divided by the HERWIG prediction in three ranges of ξ. The deviations between these two models are of the order of 2% at $0.05 < \xi < 0.1$ and about 10% for other two ξ regions. The difference between these two hadronisation models is used as systematic uncertainty.
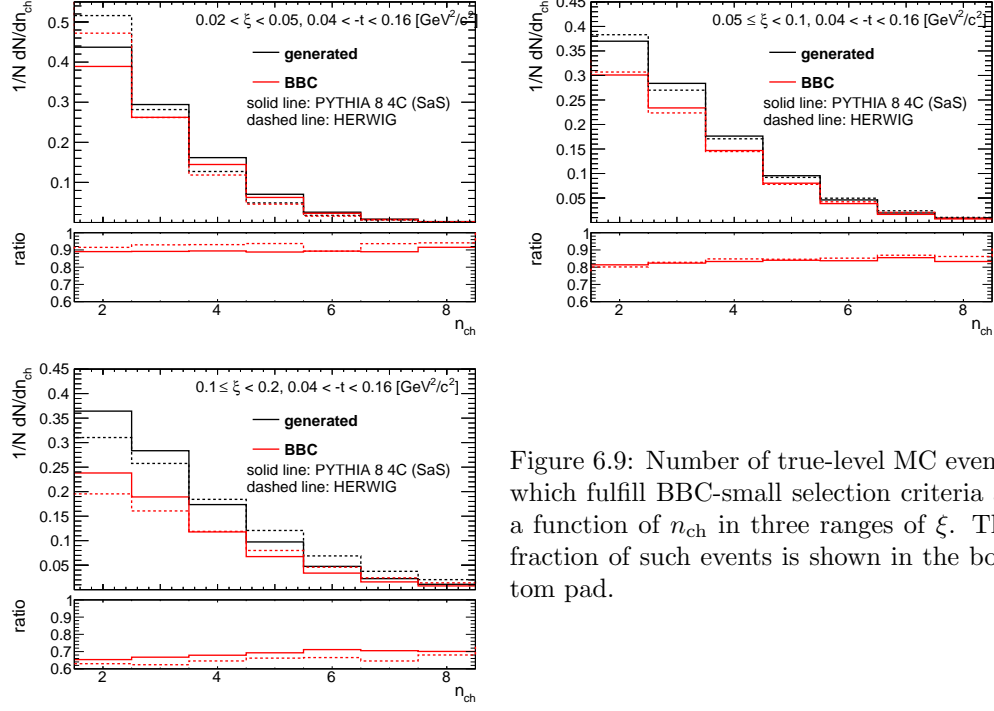
26

Figure 6.9: Number of true-level MC events which fulfill BBC-small selection criteria as a function of $n_{\rm ch}$ in three ranges of ξ. The fraction of such events is shown in the bottom pad.
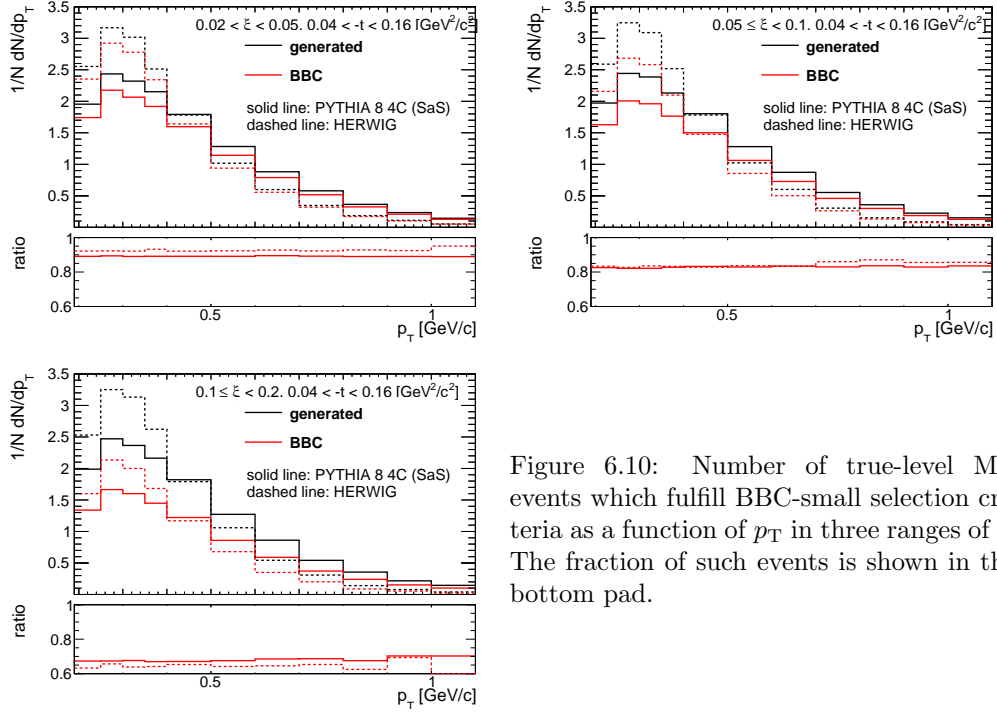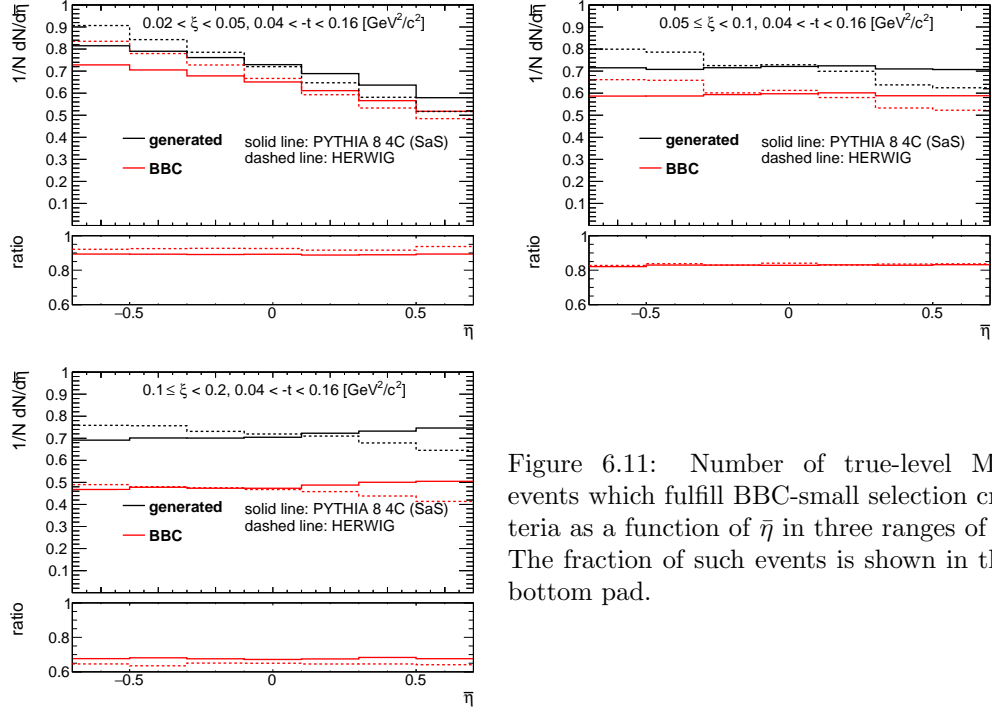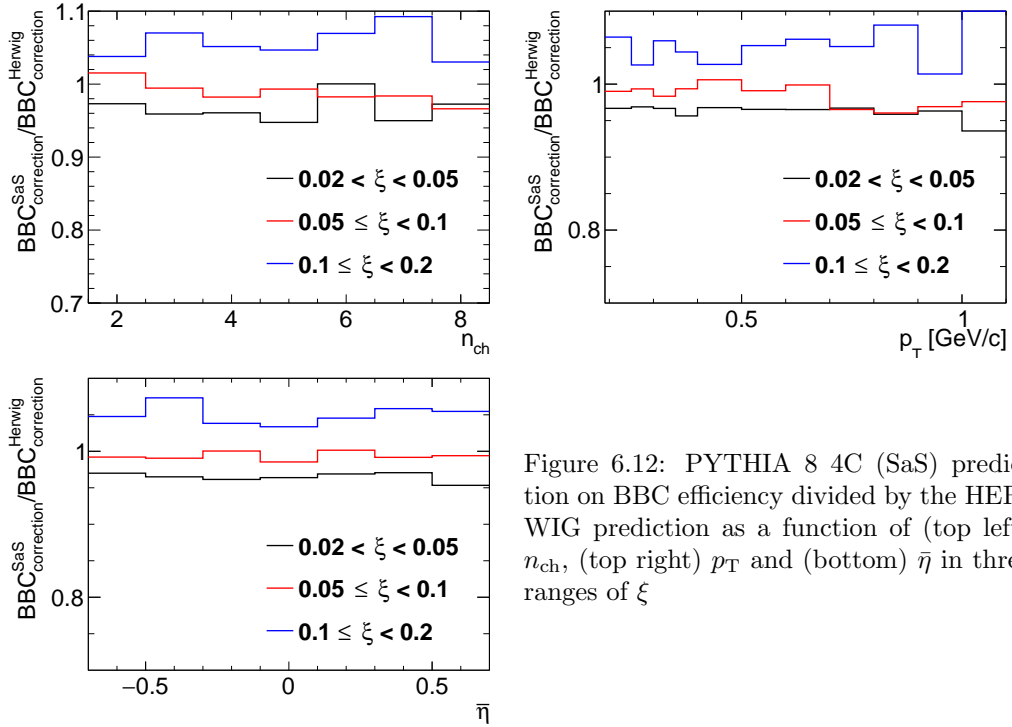

Figure 6.10: Number of true-level MC events which fulfill BBC-small selection criteria as a function of $p_{\rm T}$ in three ranges of ξ. The fraction of such events is shown in the bottom pad.

Figure 6.11: Number of true-level MC events which fulfill BBC-small selection criteria as a function of $\bar{\eta}$ in three ranges of ξ. The fraction of such events is shown in the bottom pad.

Figure 6.12: PYTHIA 8 4C (SaS) prediction on BBC efficiency divided by the HERWIG prediction as a function of (top left) n_{ch}, (top right) p_T and (bottom) $\bar{\eta}$ in three ranges of ξ

7. Migrations into and out of the Fiducial Region

In this section the corrections due to the migrations of tracks and forward proton into and out of the fiducial region are described.

7.1 Migrations of Tracks into and out of the Fiducial Region

The procedure, described in this section, accounts for migrations of tracks into and out of the fiducial region, which originate from TPC resolution effects. The correction factor for such tracks, $f_{\mathrm{okr}}(p_T, \eta)$ is defined as follows:

$$f_{\mathrm{okr}}(p_{\mathrm{T}}, \eta) = \frac{1 - f_{\mathrm{okr}}^{-}(p_{\mathrm{T}}, \eta)}{1 - f_{okr}^{+}(p_{\mathrm{T}}, \eta)} \tag{7.1}$$

where:

$f_{\mathrm{okr}}^{-}(p_{\mathrm{T}}, \eta)$ is the fraction of reconstructed tracks for which the corresponding primary particle is outside of the kinematic range of the measurement,

$f_{\mathrm{okr}}^{+}(p_{\mathrm{T}}, \eta)$ is the fraction of primary particles for which the corresponding reconstructed track is outside of the kinematic range of the measurement.

The resulting residual migrations, shown in Fig. 7.1, were estimated using PYTHIA 8 SD embedding MC. The main effect was observed at $|\eta| \sim 0.7$, where about $2-6\%$ reconstructed tracks were associated to primary particle outside the fiducial region. However, above contributions to the correction factor, $f_{\mathrm{okr}}(p_T, \eta)$, cancel each other and a resultant factor is about 2% at $|\eta| \sim 0.7$.
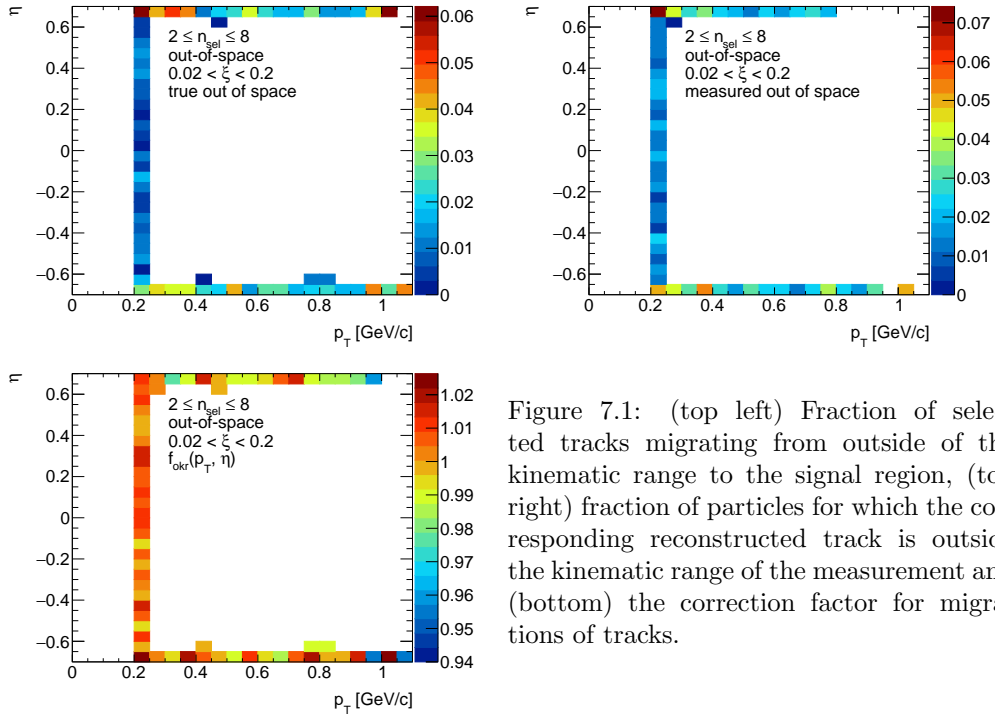

Figure 7.1: (top left) Fraction of selected tracks migrating from outside of the kinematic range to the signal region, (top right) fraction of particles for which the corresponding reconstructed track is outside the kinematic range of the measurement and (bottom) the correction factor for migrations of tracks.

29

7.2 Migrations in ξ

The analysis was performed in three ranges of ξ. Thus, there are migrations into and out of these ξ regions. They mainly originate from the resolution of ξ, which is measured with the RPs. Figure 7.2 shows the resolution of ξ as a function of the true-level ξ (denoted as ξ_{true}) with fitted zeroth order polynomial. The resolution of ξ_{reco} is fairly constant and equals to about 0.3%.

The corrections due to migrations into and out of ξ regions was defined as:

$$f_\xi = \frac{1 - f_\xi^-}{1 - f_\xi^+} \qquad (7.2)$$

where:

f_ξ^- is the fraction of events for which the corresponding true-level ξ_{true}, is outside of the ξ region,

f_ξ^+ is the fraction of events for which the corresponding reconstructed ξ_{reco} is outside of the ξ region.
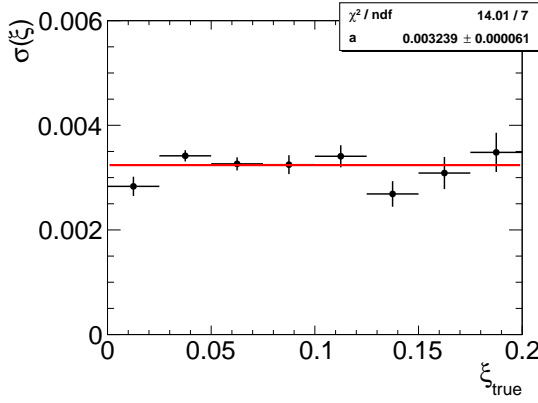
Figure 7.2: The resolution of ξ as a function of ξ_{true}. The zeroth order polynomial, shown as red line, was fitted.

The f_ξ was calculated for each measured variable separately. Figures 7.3 to 7.5 show the fraction of events f_ξ^- and f_ξ^+ as a function of n_{ch}, p_{T} and $\bar{\eta}$. The largest differences between migrations into and out of the ξ regions were observed at $0.02 < \xi < 0.05$, where they are of the order of $2 - 3\%$. In the other ξ regions, the difference between f_ξ^- and f_ξ^+ is smaller than 1%.
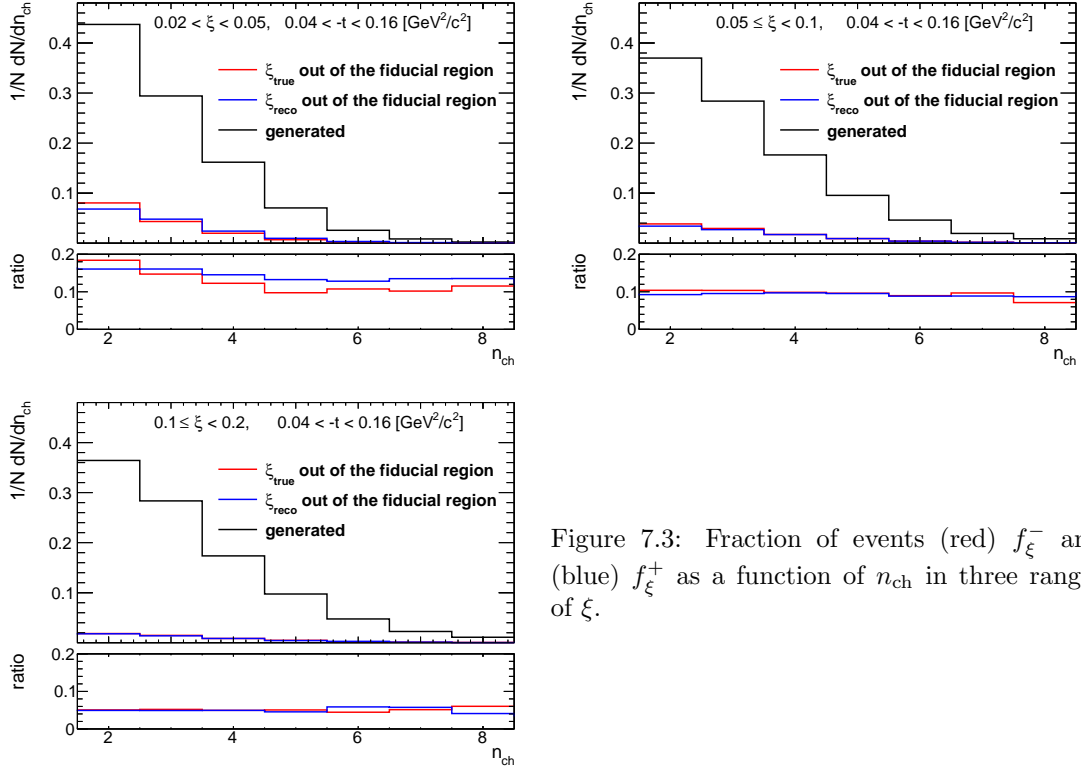
Figure 7.3: Fraction of events (red) f_ξ^- and (blue) f_ξ^+ as a function of n_{ch} in three ranges of ξ.
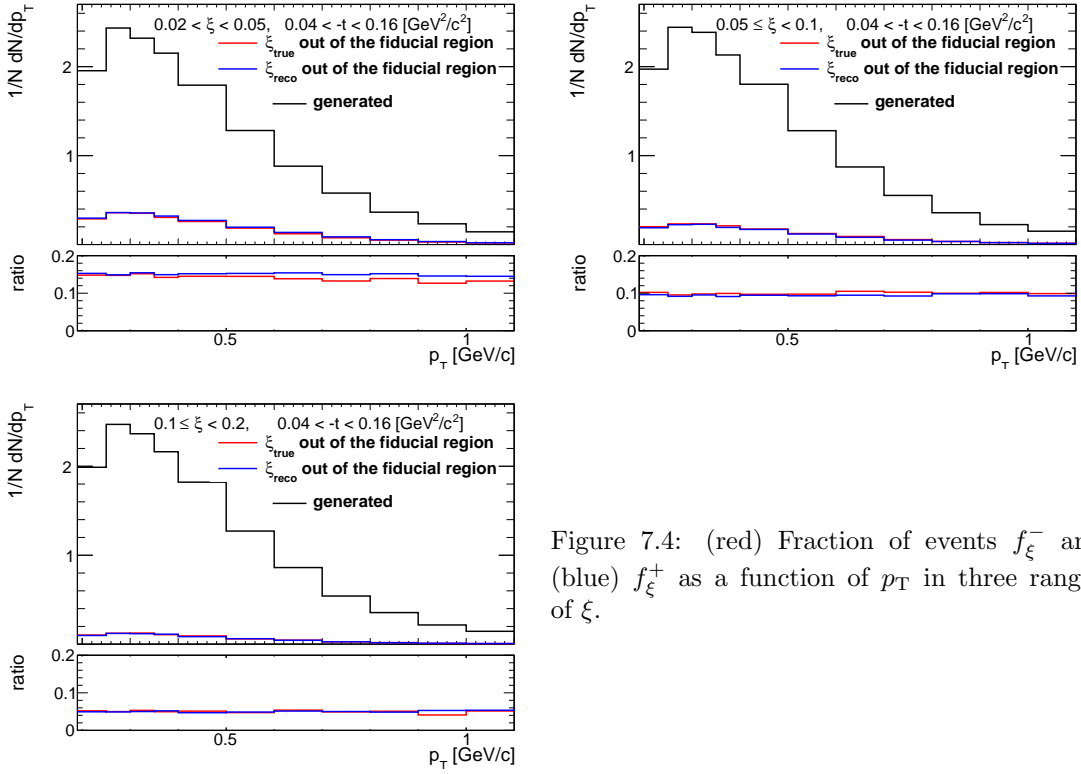

Figure 7.4: (red) Fraction of events f_ξ^- and (blue) f_ξ^+ as a function of p_T in three ranges of ξ.
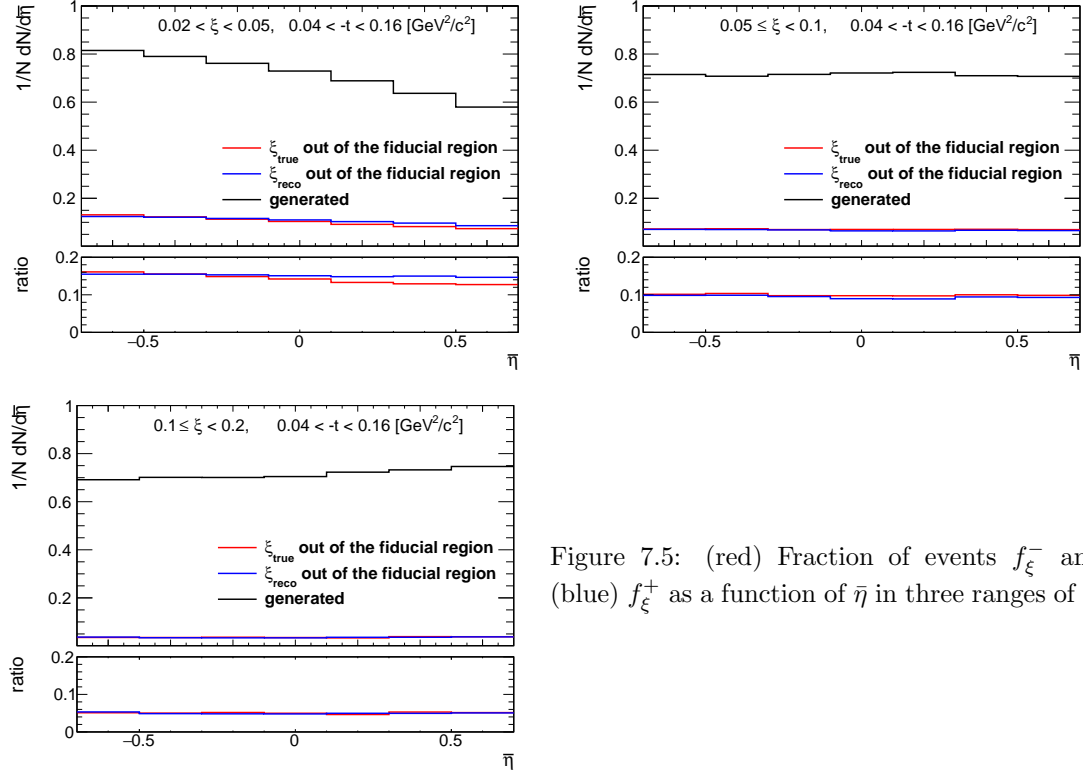
Figure 7.5: (red) Fraction of events f_ξ^- and (blue) f_ξ^+ as a function of $\bar{\eta}$ in three ranges of ξ.

8. Corrections and Unfolding Procedure

After subtraction of accidental, DD, CD and ND backgrounds, the data was corrected for detector inefficiencies to obtain the distributions of charged particles and particle to antiparticle (pion, kaon, proton and their antiparticle) multiplicity ratios. These corrections include:

- event-by-event weights due to vertex reconstruction efficiency:

$$w_{\mathrm{ev}}^{\mathrm{vrt}}\left(n_{\mathrm{vrt}}^{\mathrm{global}}, |\Delta z_0|\right) = \frac{1}{\epsilon_{\mathrm{vrt}}\left(n_{\mathrm{vrt}}^{\mathrm{global}}, |\Delta z_0|\right)} \cdot \frac{1}{\epsilon_{\mathrm{vrt}}^{\mathrm{veto}}\left(n_{\mathrm{vrt}}^{\mathrm{global}}, |\Delta z_0|\right)} \tag{8.1}$$

  where the $|\Delta z_0|$ dependence is only applicable for events with $n_{\mathrm{vrt}}^{\mathrm{global}} = 2$ as described in Sec. 6.1.

- track-by-track weights due to track reconstruction efficiency, track backgrounds, migrations of tracks into and out of the fiducial region:

$$w_{\mathrm{trk}}\left(p_{\mathrm{T}}, \eta, V_z\right) = \frac{1 - f_{\mathrm{bkg}}\left(p_{\mathrm{T}}, \eta\right) - f_{\mathrm{fake}}\left(p_{\mathrm{T}}, \eta\right)}{\epsilon_{\mathrm{TPC}}\left(p_{\mathrm{T}}, \eta, V_z\right) \epsilon_{\mathrm{TOF}}\left(p_{\mathrm{T}}, \eta, V_z\right)} f_{\mathrm{okr}}\left(p_{\mathrm{T}}, \eta\right) \tag{8.2}$$

  where: $\epsilon_{\mathrm{TPC}}\left(p_{\mathrm{T}}, \eta, V_z\right)$ is TPC track reconstruction efficiency [1], $\epsilon_{\mathrm{TOF}}\left(p_{\mathrm{T}}, \eta, V_z\right)$ is TOF matching efficiency [1], $f_{\mathrm{okr}}\left(p_{\mathrm{T}}, \eta\right)$ is a factor accounting for migrations of tracks into and out of the fiducial region, $f_{\mathrm{bkg}}\left(p_{\mathrm{T}}, \eta\right)$ is a fraction of background tracks, and $f_{\mathrm{fake}}\left(p_{\mathrm{T}}, \eta\right)$ is a fraction of fake tracks.

- event-by-event (for n_{ch} distribution) or track-by-track (for p_{T}, $\bar{\eta}$ distributions) weights, f_ξ, due to migrations of events between three ξ regions.

Additionally, the obtained distributions were corrected for BBC-small efficiency, ϵ_{BBC}, using the following weight, which was calculated for each true-level quantity (n_{ch}, p_{T}, $\bar{\eta}$) separately:

$$w_{\mathrm{BBC}} = \frac{1}{\epsilon_{\mathrm{BBC}}} \tag{8.3}$$

In the following sections, the correction procedure for each of the measured distributions is presented separately. The uncorrected distributions in a wider range are shown in Figs. 5.2 to 5.4.

8.1 Correction to dN/dn$_{\mathrm{sel}}$

In order to express the multiplicity distribution in terms of the number of charged particles, n_{ch}, instead of the number of selected tracks, n_{sel}. The following procedure based on the Bayesian unfolding [11, 12] was used. First, the n_{sel} distribution was corrected for vertex reconstruction effects by applying event-by-event weights, $w_{\mathrm{ev}}^{\mathrm{vrt}}(n_{\mathrm{vrt}}^{\mathrm{global}}, |\Delta z_0|)$. The number of events in which n_{ch} are produced, $N_{\mathrm{ev}}(n_{\mathrm{ch}})$, can be associated with the number of events in which n_{sel} are reconstructed, $N_{\mathrm{ev}}(n_{\mathrm{sel}})$. Since there are several possible n_{sel} observed in n_{ch} event, $N_{\mathrm{ev}}(n_{\mathrm{ch}})$ is given by:

$$\begin{aligned} N_{\mathrm{ev}}(n_{\mathrm{ch}}) &= \sum_{\substack{n_{\mathrm{sel}} \geq 0 \\ n_{\mathrm{sel}} \leq 8}} P(n_{\mathrm{ch}}|n_{\mathrm{sel}}) \cdot N_{\mathrm{ev}}(n_{\mathrm{sel}}) \\ &= \frac{1}{\epsilon_m(n_{\mathrm{ch}})\epsilon_r(n_{\mathrm{ch}})} \sum_{n_{\mathrm{sel}} \geq 2} P(n_{\mathrm{ch}}|n_{\mathrm{sel}}) \cdot N_{\mathrm{ev}}(n_{\mathrm{sel}}) \end{aligned} \tag{8.4}$$

where:

$P(n_{\mathrm{ch}}|n_{\mathrm{sel}})$ is the conditional probability of having n_{ch} charged particles in an event in which n_{sel} tracks were found,

$\epsilon_m(n_{\mathrm{ch}})$ is a factor, which recovers events that are lost due to TPC track reconstuction and TOF matching inefficiencies, i.e. those with $n_{\mathrm{ch}} \geq 2$ but $n_{\mathrm{sel}} < 2$,

$\epsilon_r(n_{\mathrm{ch}})$ is a factor, which recovers events which are lost due to fake tracks, i.e. those with $n_{\mathrm{ch}} \leq 8$ but $n_{\mathrm{sel}} > 8$. It was checked that this effect is negligible (smaller than 1‰) and can be omitted.

Figure 8.1 shows $\epsilon_m(n_{\mathrm{ch}})$ in three ranges of ξ. It was derived from MC and varies from about 25% for $n_{\mathrm{ch}} = 2$ to 95% for $n_{\mathrm{ch}} = 8$. Since there are additional data-driven corrections to TPC and TOF efficiences, MC events were modified by randomly removing or adding tracks. This was done in accordance with differences in the efficiencies between data and MC.
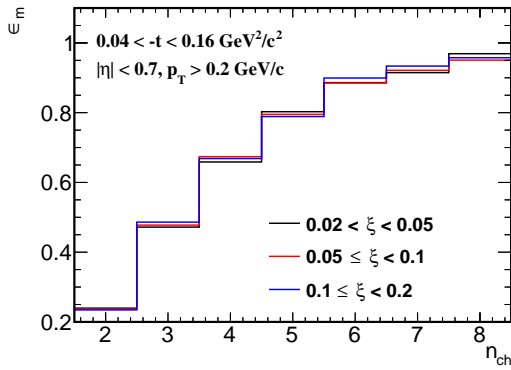
Figure 8.1: $\epsilon_m(n_{\mathrm{ch}})$ calculated separately in three ranges of ξ.

The probability $P(n_{\mathrm{ch}}|n_{\mathrm{sel}})$ can be derived using Bayes' theorem, which can be stated mathematically in terms of charged particle and charged track multiplicities as:

$$P(n_{\mathrm{ch}}) \cdot P(n_{\mathrm{sel}}|n_{\mathrm{ch}}) = P(n_{\mathrm{ch}}|n_{\mathrm{sel}}) \cdot P(n_{\mathrm{sel}}) \tag{8.5}$$

where: $P(n_{\mathrm{sel}})$ and $P(n_{\mathrm{ch}})$ are probabilities of observing n_{sel} and n_{ch} respectivelly, $P(n_{\mathrm{ch}}|n_{\mathrm{sel}})$ and $P(n_{\mathrm{sel}}|n_{\mathrm{ch}})$ are conditional probabilities.

In order to improve the estimate of $P(n_{\mathrm{ch}}|n_{\mathrm{sel}})$, the unfolding is done iteratively:

- In the first iteration, it is assumed that:

$$P(n_{\mathrm{ch}}|n_{\mathrm{sel}}) = P = P^{\mathrm{MC}}(n_{\mathrm{sel}}|n_{\mathrm{ch}}) \frac{P^{\mathrm{MC}}(n_{\mathrm{ch}})}{P^{\mathrm{MC}}(n_{\mathrm{sel}})} \tag{8.6}$$

$$N_{\mathrm{ev}}(n_{\mathrm{ch}}) = \frac{1}{\epsilon_m(n_{\mathrm{ch}})} \sum_{n_{\mathrm{sel}} \geq 2}^{n_{\mathrm{sel}} \leq 8} N_{\mathrm{ev}}(n_{\mathrm{sel}}) \cdot P \tag{8.7}$$

where $P^{\mathrm{MC}}(n_{\mathrm{sel}}|n_{\mathrm{ch}})$, $P^{\mathrm{MC}}(n_{\mathrm{ch}})$ and $P^{\mathrm{MC}}(n_{\mathrm{sel}})$ are obtained from MC. $P^{\mathrm{MC}}(n_{\mathrm{sel}}|n_{\mathrm{ch}})$ is the same for each iteration.

- In the $(i+1)$th iteration we have:

$$P^{i+1} = P^{\mathrm{MC}}(n_{\mathrm{sel}}|n_{\mathrm{ch}}) \frac{N_{\mathrm{ev}}^{i}(n_{\mathrm{ch}})}{N_{\mathrm{ev}}(n_{\mathrm{sel}})} \tag{8.8}$$

$$N_{\mathrm{ev}}^{i+1}(n_{\mathrm{ch}}) = \frac{1}{\epsilon_m(n_{\mathrm{ch}})} \sum_{n_{\mathrm{sel}} \geq 2}^{n_{\mathrm{sel}} \leq 8} N_{\mathrm{ev}}(n_{\mathrm{sel}}) \cdot P^{i+1} \tag{8.9}$$

where $N_{\mathrm{ev}}^{i}(n_{\mathrm{ch}})$ is calculated in the previous iteration, and $N_{\mathrm{ev}}(n_{\mathrm{sel}})$ is taken from data.

34

The unfolding matrices $P(n_{ch}|n_{sel})$ for each ξ region, shown in Fig. 8.2, were obtained from MC and used in all iterations of the above procedure. Similarly to $\epsilon_m(n_{ch})$, the matrices were modified in order to take into account differences between data and MC.
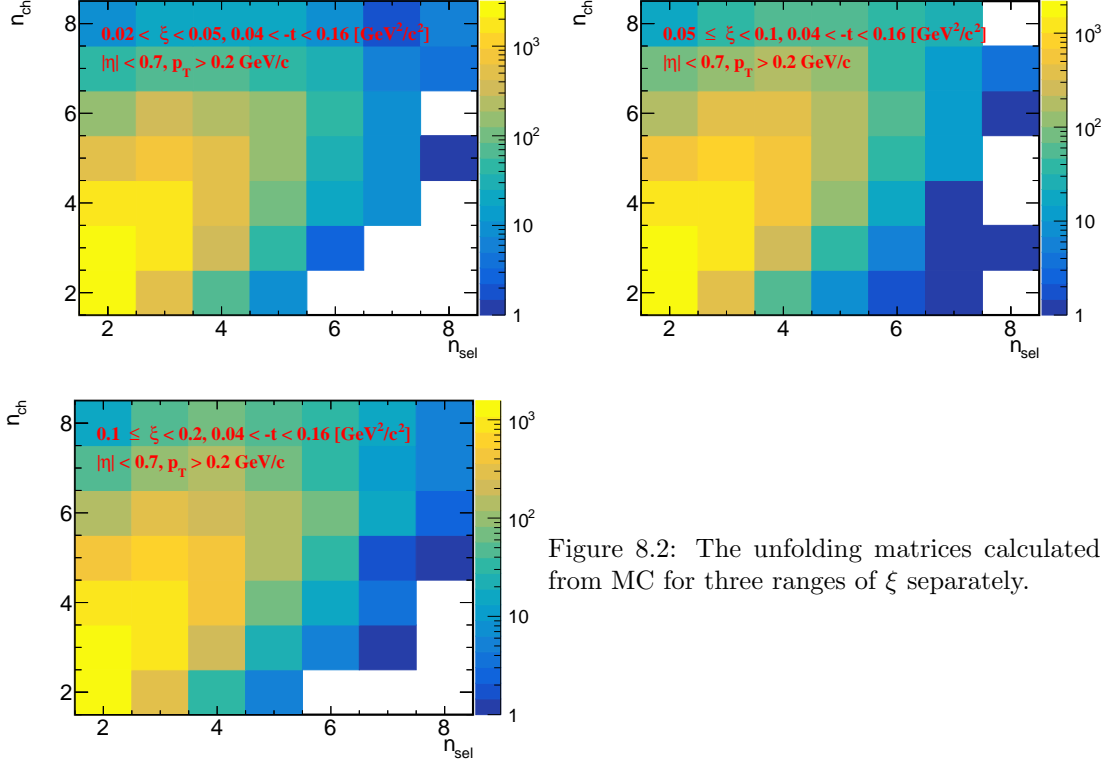

Figure 8.2: The unfolding matrices calculated from MC for three ranges of ξ separately.

The distribution dN/dn_{ch} obtained after the unfolding procedure was corrected for BBC-small efficiency, through $w_{BBC}(n_{ch})$ weights, and migrations of events between ξ ranges, through $f_\xi(n_{ch})$ weights. Since the unfolding matrices contain track reconstruction efficiencies, non-primary track backgrounds, migrations of tracks into and out of the fiducial region, the weight $w_{trk}(p_T, \eta, V_z)$ was not used.

Finally, the dN/dn_{ch} distribution was normalized to the total number of events, $N_{ev} = N$, which was calculated as the integral of the unfolded distribution.

8.2 Correction to Transverse Momentum and Pseudorapidity Distributions

First the accidental and non-SD backgrounds were subtrated from the p_T and $\bar{\eta}$ distributions. Next, each event was corrected for vertex reconstruction efficiency by applying $w_{ev}^{vrt}(n_{vrt}^{global}, |\Delta z_0|)$ weights. Then, the tracks were corrected for the track reconstruction efficiency, non-primary track background contribution, track and ξ migrations, BBC-small efficiency (the product of $w_{trk}(p_T, \eta, V_z)$, f_ξ and w_{BBC} weights was applied, f_ξ and w_{BBC} were calculated as a function of true-level p_T and $\bar{\eta}$ separately).

In order to obtain charged-particle densities, the p_T and $\bar{\eta}$ distributions were normalized to unity and scaled by the average charged particle multiplicity in an event $\langle n_{ch} \rangle$. The latter was calculated from the corrected charged particle multiplicity distribution dN/dn_{ch} (Sec. 8.1).

The mean particle densities in an event, $\langle p_T \rangle$ and $\langle \bar{\eta} \rangle$, were obtained from the measured distributions.

8.3 Closure Tests

In order to validate the correction procedures, closure tests were performed , i.e. full correction procedure was applied to the MC detector-level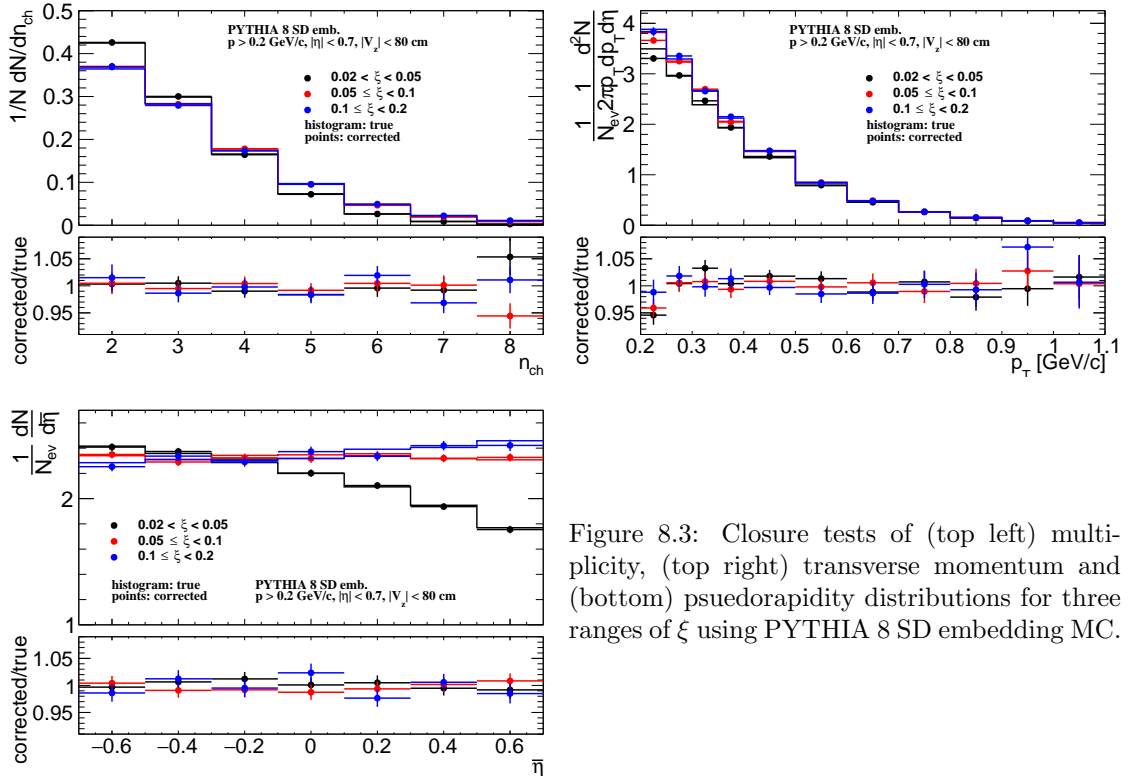 distributions and the results were directly compared to the true-level distributions. Figure 8.3 shows closure tests of multiplicity, transverse momentum and pseudorapidity distributions for three ranges of ξ, separately. PYTHIA 8 SD embedding MC was used as an input. In order to compare corrected and true-level distributions, the statistical uncertainties of the true-level distributions were assumed to be 0. Due to the method of factorization of the global efficiency into the product of single-particle efficiencies, a level of non-closure below 5% is typically considered to be sufficient for the validation of the procedure. However, the difference between true-level and corrected distributions was taken as a systematic uncertainties.

Figure 8.3: Closure tests of (top left) multiplicity, (top right) transverse momentum and (bottom) psuedorapidity distributions for three ranges of ξ using PYTHIA 8 SD embedding MC.

8.4 EAST-WEST asymmetry

Since some data-driven corrections are used and they can not be directly validated by closure tests for MC, other tests were performed to check the correction procedures for data. Therefore, each distribution was calculated separately for events in which forward proton is on one and the other side of the IP (east-west). Figure 8.4 shows the tests of multiplicity, transverse momentum and pseudorapidity distributions for three ranges of ξ, separately. The largest difference is observed for charged-particle multiplicity distributions, where it varies up to 20% for $n_{ch} \geq 7$ and $0.02 < \xi < 0.05$. For the rest multiplicities and ξ ranges, the differences are smaller ($< 10\%$). In case of p_T and $\bar{\eta}$ distributions, a level of these disagreements is below 5%. As a result, half of the differences between east and west distributions were used to be systematic uncertainty.
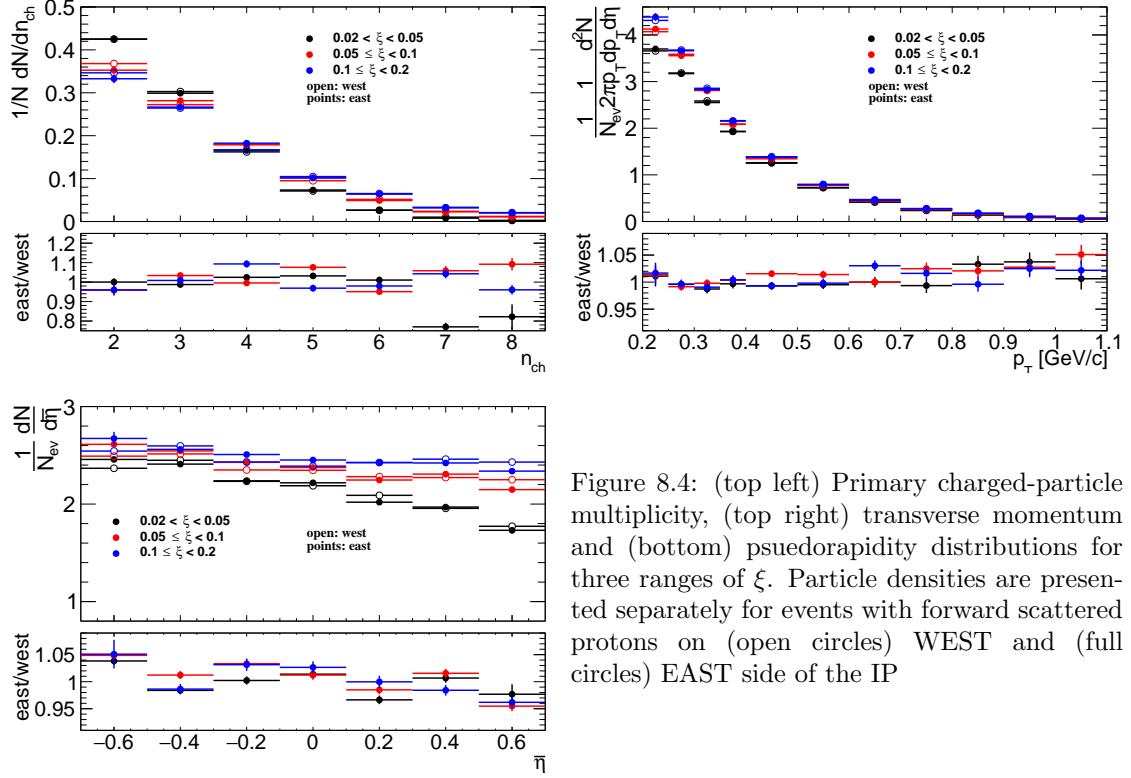
Figure 8.4: (top left) Primary charged-particle multiplicity, (top right) transverse momentum and (bottom) psuedorapidity distributions for three ranges of ξ. Particle densities are presented separately for events with forward scattered protons on (open circles) WEST and (full circles) EAST side of the IP

8.5 Particle Identification

The specific ionization energy loss, the dE/dx, is a function of magnitude of the particle momentum. In this section the particle identification by the dE/dx is described. Due to the low particle multiplicity and lack of signal in VPDs on the outgoing proton side (presence of the rapidity gap) in SD events, the time of collision is not defined precisely enough, therefore, the particle identification by the TOF is not possible and the analysis was limited to identification only by dE/dx.

The ionization energy loss of charged particles in material is given by the Bethe-Bloch formula and for the STAR TPC by the more precise Bichsel formula [13]. The particle type can be determined by comparison of particle's dE/dx with the Bethe-Bloch (Bichsel) expectations. Figure 8.5 shows the dE/dx versus rigidity $q \times p$ for particles in $|\eta| < 0.7$. Particles are well separated at low $|q \times p|$, whereas at higher $|q \times p|$ the dE/dx of different particle species starts to overlap: $e^{\pm}$ and $K^{\pm}$ merge at ~ 0.4 GeV/c, $K^{\pm}$ and $\pi^{\pm}$ merge at ~ 0.65 GeV/c, and $p(\bar{p})$ and $\pi^{\pm}$ merge at ~ 1 GeV/c. Since the dE/dx distribution for a fixed particle type is not Gaussian, the following variable for each particle type was defined:

$$n\sigma^{i}_{dE/dx} = \ln\left(\frac{dE/dx}{(dE/dx)^{\mathrm{BB}}_{i}}\right)/\sigma \tag{8.10}$$

where $(dE/dx)^{\mathrm{BB}}_{i}$ is the Bethe-Bloch (Bichsel) expectation of dE/dx for the given particle type i ($i = \pi, K, p$), σ - the dE/dx resolution. The expected value of $n\sigma^{i}_{dE/dx}$ for the particle under consideration is 0 and the width equals to 1. The sample $n\sigma^{i}_{dE/dx}$ distribution for $\pi^{\pm}$, $K^{\pm}$ and $p(\bar{p})$ in one ξ range, $0.02 < \xi < 0.05$, is shown in Fig. 8.6. Figure 8.7 shows the $n\sigma^{\pi^{\pm}}_{dE/dx}, n\sigma^{K^{\pm}}_{dE/dx}$ and $n\sigma^{p(\bar{p})}_{dE/dx}$ distributions for $0.6 < p_{\mathrm{T}} < 0.65$ GeV/c in the ξ range, $0.02 < \xi < 0.05$, each corrected for the energy loss (mass of i-particle was assumed) [1] and vertexing (other p_{T} bins are shown in Appendix C). To extract the particle yield for a given
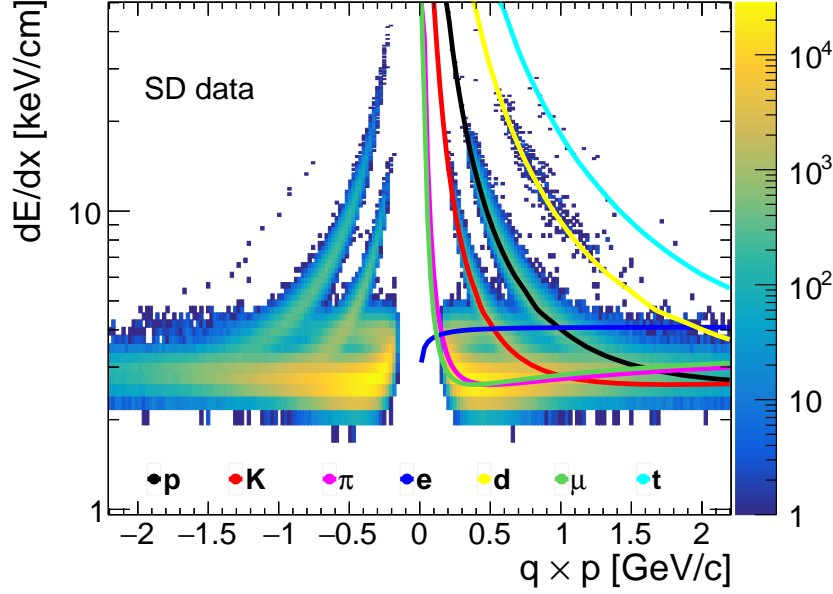
Figure 8.5: Specific ionization energy loss dE/dx as a function of rigidity $q \times p$ for particles in $|\eta| < 0.7$. The Bichsel predictions for each particle species are also shown.

particle type, a multi-Gaussian fit is applied to the $n\sigma^i_{dE/dx}$ distribution in each p_{T} bin and ξ range. The parameters of the multi-Gaussian fit are the centroids μ_{i^-/i^+}, widths σ_{i^-/i^+}, sum and ratios of yields C_{i^-/i^+}, r_{i^-/i^+} for negative i^- and positive i^+ particles ($\pi^\pm$, $e^\pm$, $K^\pm$, p and $\bar{p}$). The positive and negative particle $n\sigma^i_{dE/dx}$-distributions are fitted simultaneously, where the centroids and widths are kept the same for particle and antiparticle. In some p_{T} regions, the fit does not converge, because different particle species are not well separated there. Therefore, multiple steps of fitting are performed to reduce the number of free parameters in the final fit and ensure its stability. Almost all centroids and widths are constrained by a function with free parameters p_k, where $k \in \mathbb{N}$. The function is chosen to describe the data as best as possible. Since dE/dx is a function of the particle momentum and its shape should be independent of the process under study, the values of p_k are obtained only for events with $0.02 < \xi < 0.05$ and kept the same for other ξ ranges. The electron contributions are fixed, but separately for each ξ range. The procedure slightly differs for different particle types. In each step, the multi-Gaussian fit is performed first, then the widths and centroids are fitted in p_{T} ranges in which the fit applied to $n\sigma^i_{dE/dx}$ converges:

1. $\pi^\pm$:

    - Step 1 (Fig. 8.8):
        - Analyze data with $0.2 < p_{\mathrm{T}} < 0.65$ GeV/c
        - Fit μ_{π^-/π^+} and σ_{π^-/π^+} as a function of p_{T} with a polynomial $p_0 p_{\mathrm{T}}^3 + p_1 p_{\mathrm{T}}^2 + p_2 p_{\mathrm{T}} + p_3$
        - Fit r_{e^-/e^+} as a function of p_{T} with a polynomial $p_0 p_{\mathrm{T}}^2 + p_1 p_{\mathrm{T}} + p_2$
        - Fit C_{e^-/e^+}, μ_{K^-/K^+} as a functions of p_{T} with $p_0 \exp\left(p_1 p_{\mathrm{T}}\right) + p_2$
        - Fit μ_{e^-/e^+} as a function of p_{T} with $p_0 \exp\left[-\left(p_1 p_{\mathrm{T}}\right)^{p_2}\right]$
        - Fit σ_{K^-/K^+} as a function of p_{T}, where $0.3 < p_{\mathrm{T}} < 0.5$ GeV/c, with constant p_0
        - Fit $\mu_{\bar{p}/p}$ and $\sigma_{\bar{p}/p}$ as a function of p_{T} with $p_0 \exp\left(p_1 p_{\mathrm{T}}\right)$
    - Step 2:
        - σ_{e^-/e^+} fixed to 1.2 and 0.8 for $0.2 < p_{\mathrm{T}} < 0.4$ and $0.4 < p_{\mathrm{T}} < 0.7$, respectively
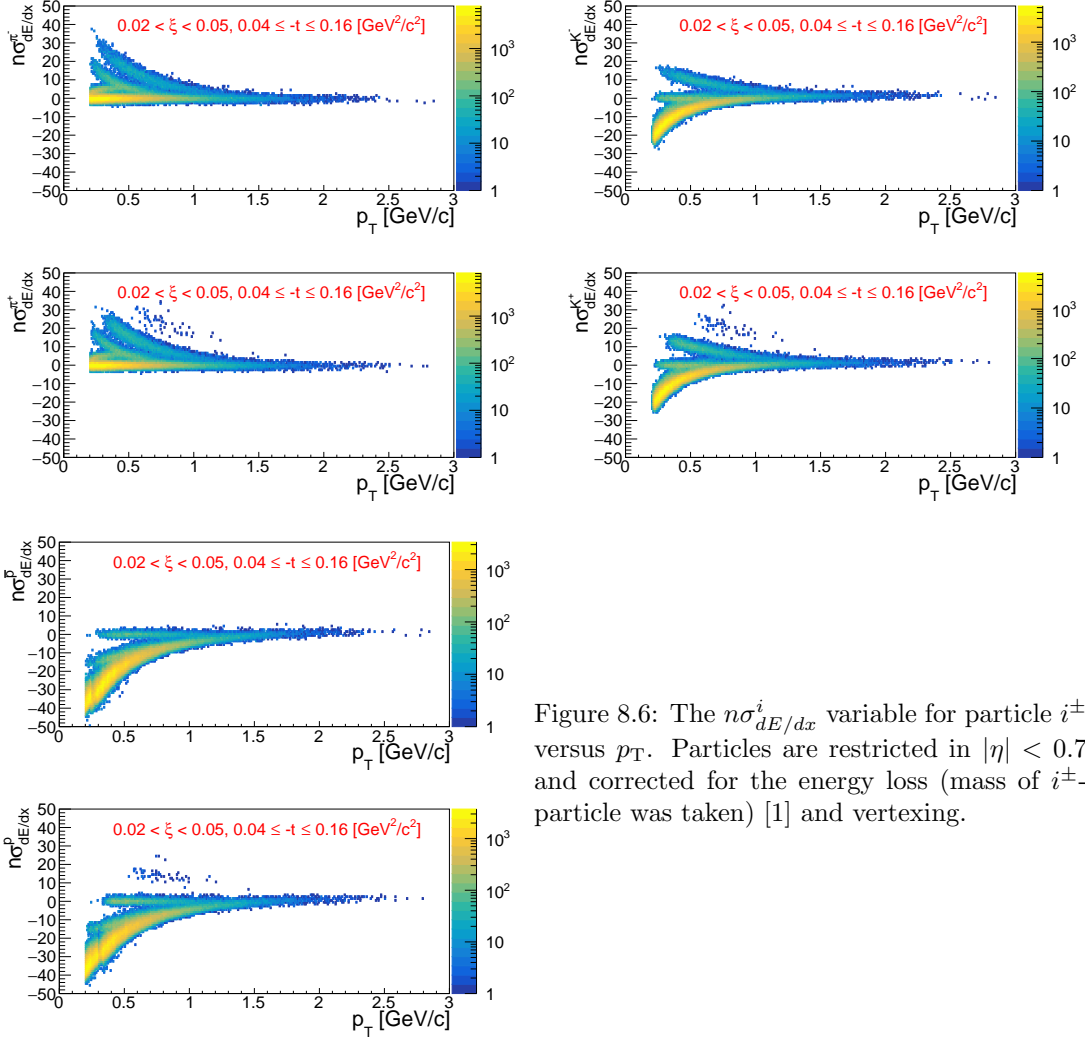   - σ_{K^-/K^+} parametrized for $0.3 < p_{\mathrm{T}} < 0.7$

Figure 8.6: The $n\sigma^i_{dE/dx}$ variable for particle $i^\pm$ versus p_T. Particles are restricted in $|\eta| < 0.7$ and corrected for the energy loss (mass of $i^\pm$-particle was taken) [1] and vertexing.

       – The rest parameters from Step 1 are fixed with obtained parametrization: μ_{π^-/π^+}, σ_{π^-/π^+}, , r_{e^-/e^+}, C_{e^-/e^+}, μ_{e^-/e^+} , μ_{K^-/K^+}, $\mu_{\bar{p}/p}$, $\sigma_{\bar{p}/p}$

2. $K^\pm$:

    • Step 1 (Fig. 8.9):

       – Analyze data with $0.2 < p_\mathrm{T} < 0.6$ GeV/c

       – Fit μ_{π^-/π^+} as a function of p_T with $-\exp\left(p_0 + p_1 p_\mathrm{T}\right)$

       – Fit σ_{π^-/π^+}, C_{e^-/e^+}, σ_{e^-/e^+}, σ_{K^-/K^+} as a function of p_T with $\exp\left(p_0 + p_1 p_\mathrm{T}\right)$

       – Fit r_{e^-/e^+} as a function of p_T with constant p_0

       – Fit μ_{e^-/e^+} as a function of p_T with a polynomial $p_0 p_\mathrm{T}^3 + p_1 p_\mathrm{T}^2 + p_2 p_\mathrm{T} + p_3$

       – Fit μ_{K^-/K^+} as a function of p_T with a polynomial $p_0 + p_1 p_\mathrm{T}^2$

    • Step 2:

       – All parameters from Step 1 except σ_{e^-/e^+} are fixed with obtained parametrization.

       – Fit σ_{e^-/e^+} as a function of p_T, where $0.45 < p_\mathrm{T} < 0.65$ GeV/c, with constant p_0

    • Step 3:
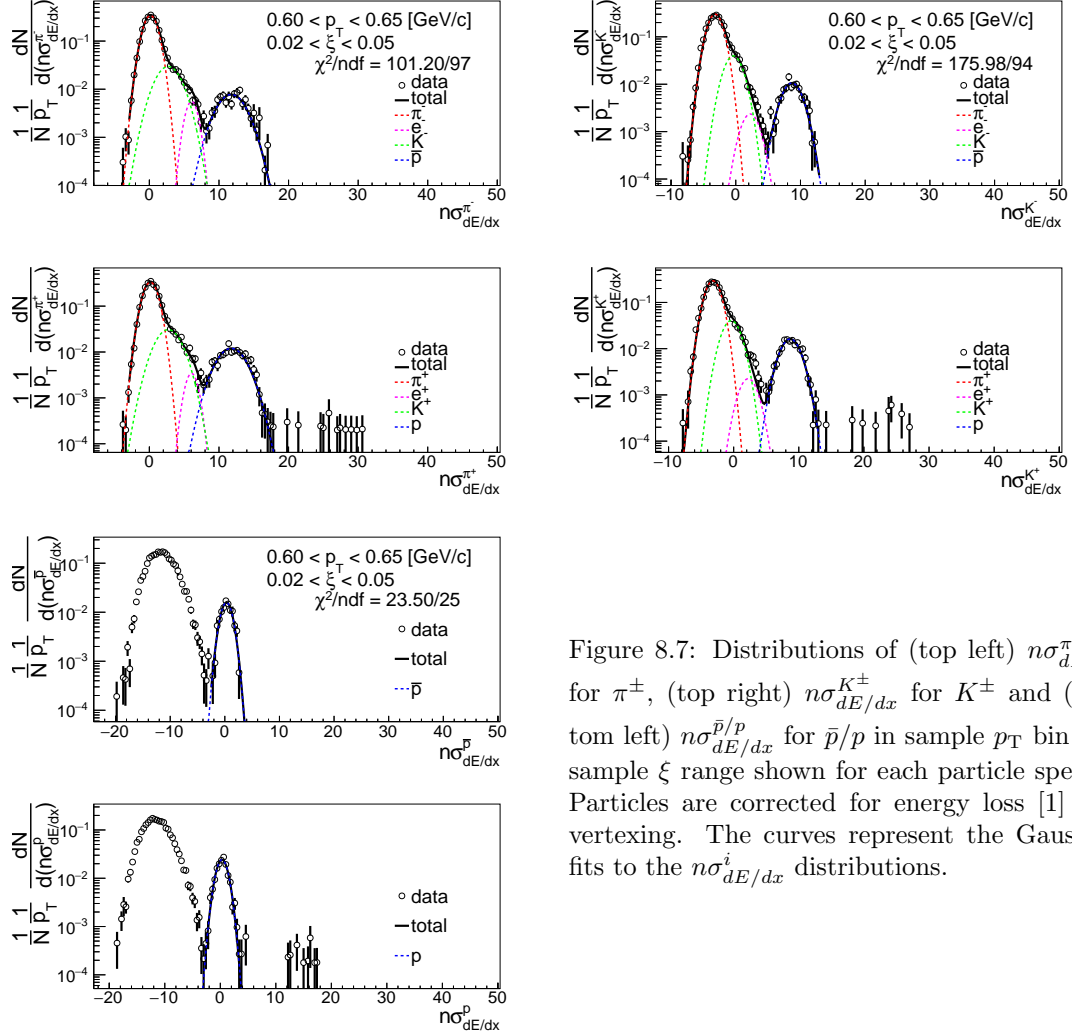
Figure 8.7: Distributions of (top left) $n\sigma_{dE/dx}^{\pi^{\pm}}$ for $\pi^{\pm}$, (top right) $n\sigma_{dE/dx}^{K^{\pm}}$ for $K^{\pm}$ and (bottom left) $n\sigma_{dE/dx}^{\bar{p}/p}$ for $\bar{p}/p$ in sample p_T bin and sample ξ range shown for each particle species. Particles are corrected for energy loss [1] and vertexing. The curves represent the Gaussian fits to the $n\sigma_{dE/dx}^{i}$ distributions.

- σ_{e^-/e^+} fixed with obtained parametrization from Steps 1 and 2 for $0.3 < p_T < 0.45$ and $0.45 < p_T < 0.65$, respectively.
- The rest parameters from Step 1 are fixed with obtained parametrization: μ_{π^-/π^+}, σ_{π^-/π^+}, , r_{e^-/e^+}, C_{e^-/e^+}, μ_{e^-/e^+} , μ_{K^-/K^+}, σ_{K^-/K^+}

3. $\bar{p}, p$:

- Step 1 (Fig. 8.10):
    - Analyze data with $0.4 < p_T < 0.9$ GeV/c
    - Fit μ_{π^-/π^+}, μ_{K^-/K^+} as a function of p_T with a polynomial $p_0 p_T + p_1$
    - Fit σ_{π^-/π^+} as a function of p_T with a polynomial $p_0 p_T^2 + p_1 p_T + p_2$
    - Fit σ_{K^-/K^+} as a function of p_T with $\exp(p_0 + p_1 p_T)$
- Step 2:
    - μ_{K^-/K^+} fixed with obtained parametrization from Step 1
    - All the rest parameters from Step 1 are limited with obtained parametrization
    - Fit μ_{π^-/π^+}, σ_{π^-/π^+}, σ_{K^-/K^+} as a function of p_T with a polynomial $p_0 p_T^2 + p_1 p_T + p_2$
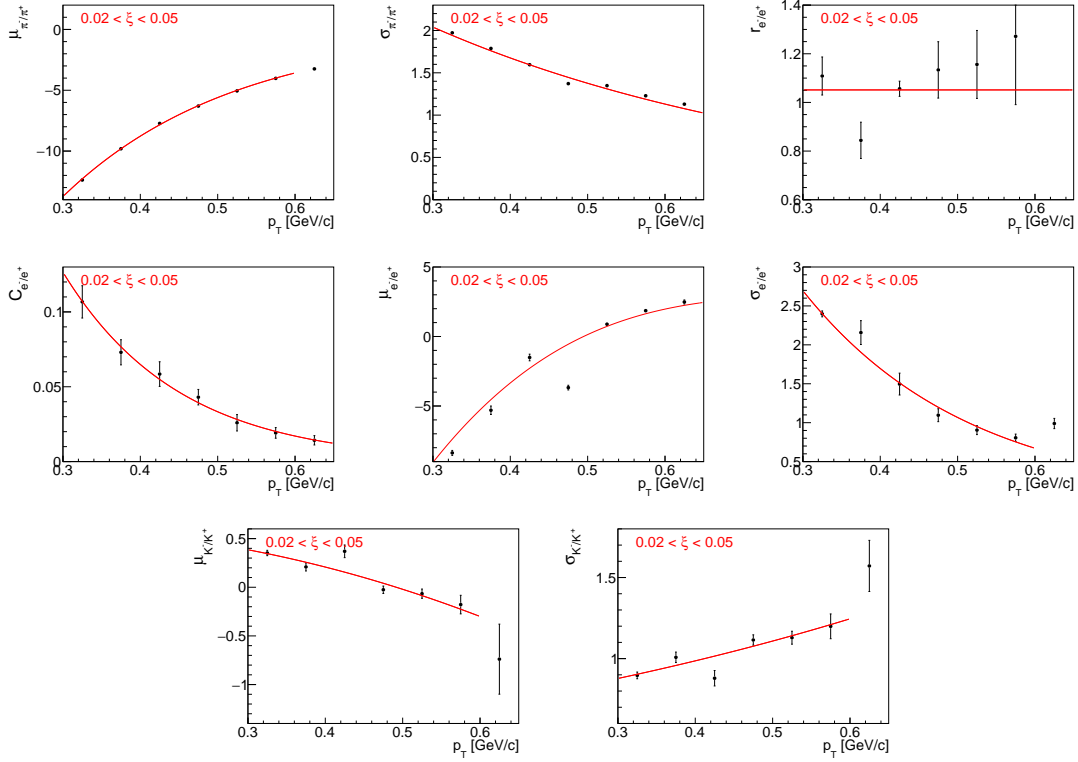
40
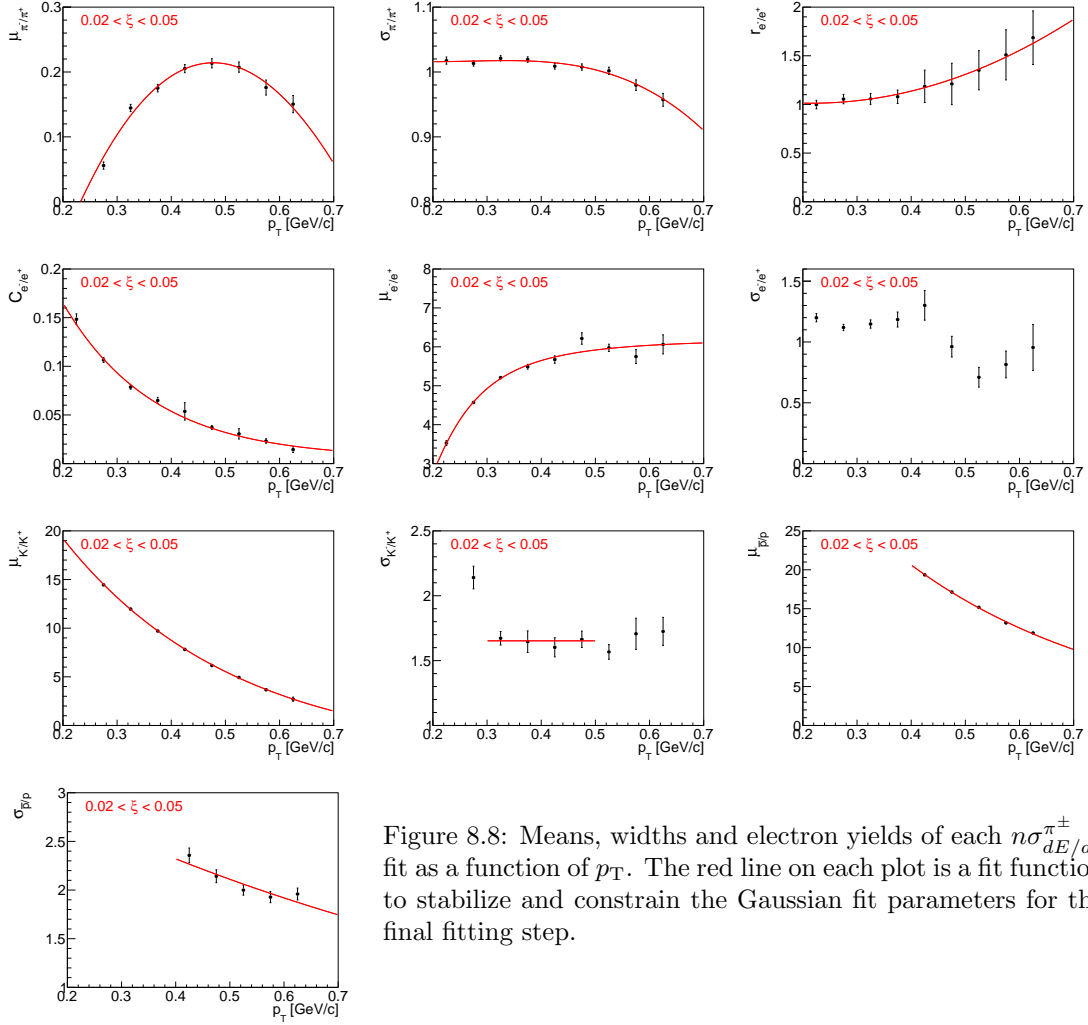
Figure 8.8: Means, widths and electron yields of each $n\sigma_{dE/dx}^{\pi^{\pm}}$ fit as a function of p_{T}. The red line on each plot is a fit function to stabilize and constrain the Gaussian fit parameters for the final fitting step.

— Fit $\mu_{\bar{p}/p}$ as a function of p_{T}, where $0.7 < p_{\mathrm{T}} < 1.0$ GeV/c, with constant p_0

- Step 3:

  — μ_{K^-/K^+} fixed with obtained parametrization from Step 1

  — $\mu_{\bar{p}/p}$ fixed with obtained parametrization from Step 2 for $0.7 < p_{\mathrm{T}} < 1.0$

  — The rest parameters from Step 2 are fixed with obtained parametrization: μ_{π^-/π^+}, σ_{π^-/π^+}, σ_{K^-/K^+}

The particle yield is extracted from the fit to the corresponding $n\sigma_{dE/dx}^{i}$ distribution (corrected only for the energy loss [1] and vertexing). As shown in Fig. 8.6, the dE/dx of each particle type merge at large p_{T}. Hence, the particle identification is limited. Pions can be identified in the momentum range of $0.2 - 0.7$ GeV/c, kaons in $0.3 - 0.65$ GeV/c and (anti)protons in $0.4 - 1.0$ GeV/c.

8.6 Antiparticle-to-Particle Ratios

The following steps were taken to correct an identified antiparticle to particle (pion, kaon, proton and their antiparticle) multiplicity ratios as a function of p_{T} in three ranges of ξ:

Figure 8.9: Means, widths and electron yields of each $n\sigma_{dE/dx}^{K^{\pm}}$ fit as a function of p_{T}. The red line on each plot is a fit function to stabilize and constrain the Gaussian fit parameters for the final fitting step.
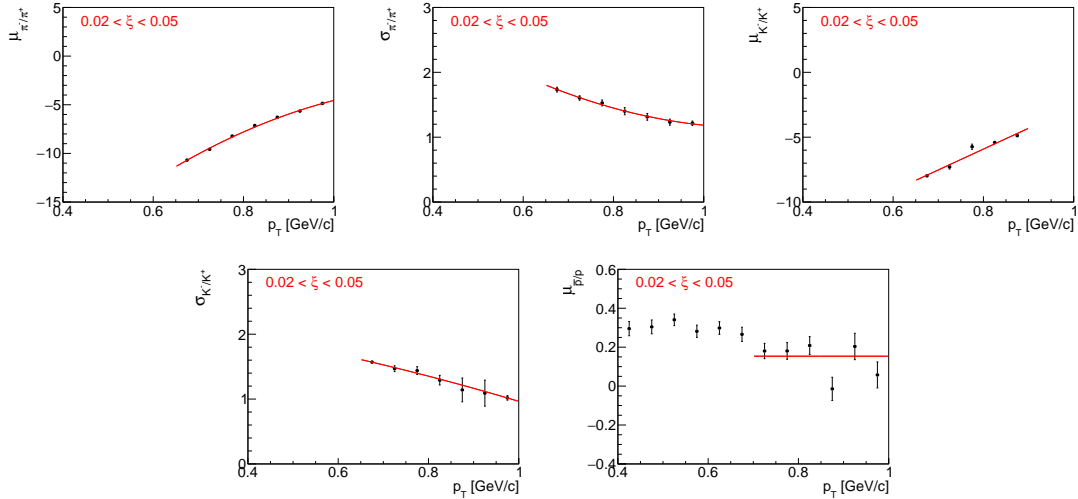
Figure 8.10: Means and widths of each $n\sigma_{dE/dx}^{\bar{p}/p}$ fit as a function of p_{T}. The red line on each plot is a fit function to stabilize and constrain the Gaussian fit parameters for the final fitting step.

- The raw identified particle yields were obtained through multi-Gaussian fits to the $n\sigma_{dE/dx}^{i}$ distributions (Sec. 8.5), where the vertex reconstruction and energy loss corrections [1] were applied. The latter depends on the particle type.

- The accidental and non-SD backgrounds were subtracted. It was assumed that the former does not depend on the particle type, i.e. the same contribution of accidental background was used as for charged particles without identification (Sec. 4.1).

- The particle yields were corrected for track reconstruction efficiencies [1], which depend on the particle type and charge. These corrections were averaged over η and V_z.

- The background from non-primary tracks was subtracted (Sec. 4.2):

  - $\pi^{\pm}$: weak decays pions, muon contribution and background from detector dead-material interactions,

  - p: background from detector dead-material interactions,

  - $p, \bar{p}$: reconstructed tracks which have the appropriate number of common hit points with true-level particle, but the distance between them is too large (this background is negligibly small for other particle types),

  - all: fake track contribution, the same for each particle type.

- Since track and ξ migrations, and BBC-small efficiency, do not depend on the particle type and charge, these corrections are not applied.

- Finally, each antiparticle p_T distribution was divided by the corresponding particle p_T distribution to obtain fully corrected identified antiparticle to particle multiplicity ratios.

- Additionally, the average antiparticle to particle ratios in each ξ region were calculated by fitting a constant to above ratios.

9. Systematic Uncertainties

Apart from the statistical uncertainties there are also systematic uncertainties originating from inefficiencies and limitations of the measurement devices and techniques. Systematic uncertainties are obtained by using modified input distributions and calculating the difference between standard and changed settings for each bin of the distribution. The systematic uncertainties on $1/N\ dN/dn_{\mathrm{ch}}$ are propagated by randomly removing and adding tracks in the n_{sel} distribution before unfolding procedure.

The following sources of systematic uncertainties were considered:

- the effect of off-time pile-up on TPC track reconstruction efficiency [1],

- the uncertainty of TPC track reconstruction efficiency related to the description of dead-material in simulation [1],

- representation of data sample in embedding MC [1],

- fake track background contribution (Sec. 4.2),

- TOF system simulation accuracy [1],

- accidental background contribution (Sec. 4.1),

- the effect of alternative model of hadronisation on BBC-small efficiency (Sec. 6.2),

- non-SD background contribution (Sec. 5),

- non-closure (Sec 8.3),

- non-closure of N_{ev}, applied only to p_{T} and $\bar{\eta}$ distributions,

- the $1/N_{\mathrm{ev}}\ dN/d\bar{\eta}$ distribution was calculated separately for events in which forward proton is on one and the other side of the IP (east-west).

Figures 9.1 to 9.3 show the components contributing to the total systematic uncertainty for charged particle distributions without the identification. The dominant systematic uncertainty for p_{T} and n_{ch} distributions is related to TOF system simulation accuracy. It affects mainly low-p_{T} particles, where it is about 6%, and large charged particle multiplicities, where it varies up to 25% for $n_{\mathrm{ch}} = 8$ and $0.02 < \xi < 0.05$. In case of $\bar{\eta}$ distribution, the systematic uncertainty on TOF mainly refers to charged particles produced at the edge of the fiducial region, for which it is about 2%. However, the largest (up to 6%) systematic uncertainty for $\bar{\eta}$, is related to the observed diffrence in the distributions calculated separately with respect to the forward proton direction. The rest of the components have smaller contributions to the total systematic uncertainty. The systematic uncertainty on non-closure is at the level of 2% which proves the accuracy of the correction procedure.

Figures 9.4 to 9.7 show breakdown of all different systematics for the antiparticle-to-particle multiplicity ratio distributions. An additional systematic contribution for $\bar{p}/p$ multiplicity ratio due to proton background estimation was introduced. Since most of the corrections are the same for particle and its antiparticle, nearly all systematic uncertainties cancel out in the antiparticle-to-particle ratios. The largest sources of systematics, which do not, are related to proton background estimation and dead-material effect on TPC track reconstruction efficiency. The former was found to be up to 5%, whereas the latter varies up to 2% for low-p_{T} $\bar{p}/p$ multiplicity ratio.
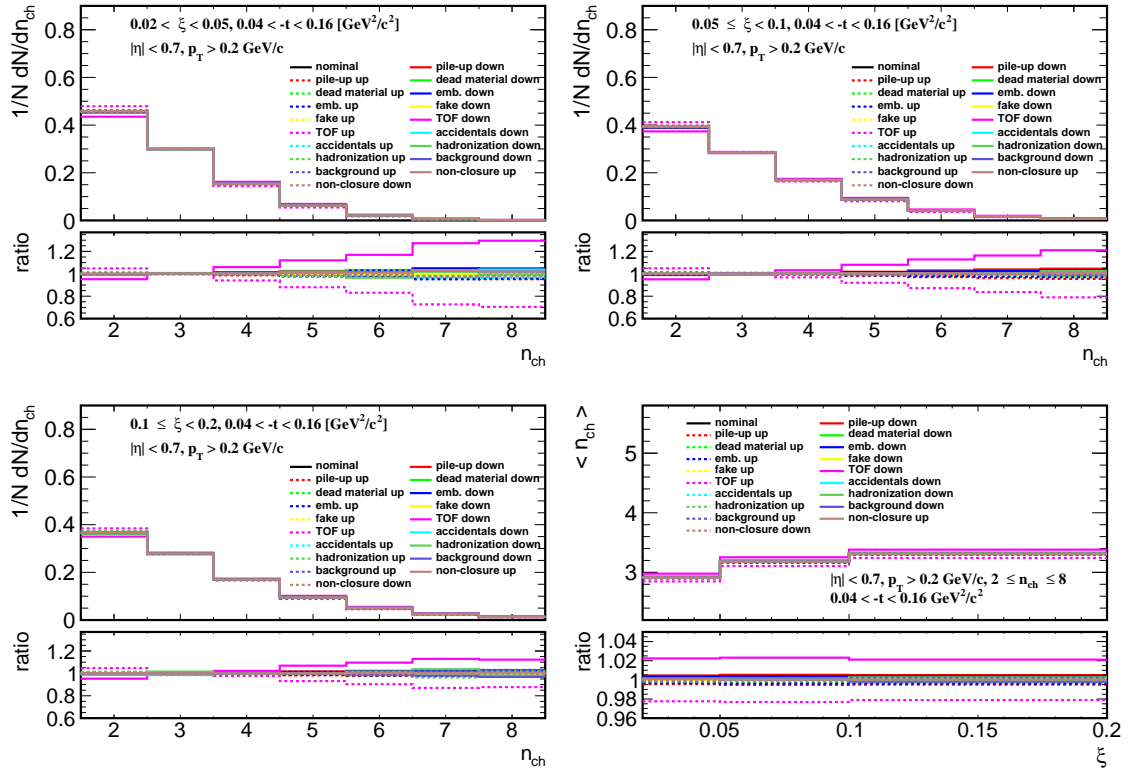
Figure 9.1: Components of the systematic uncertainties for the charged particle multiplicity in three ξ regions and for the average charged particle multiplicity.
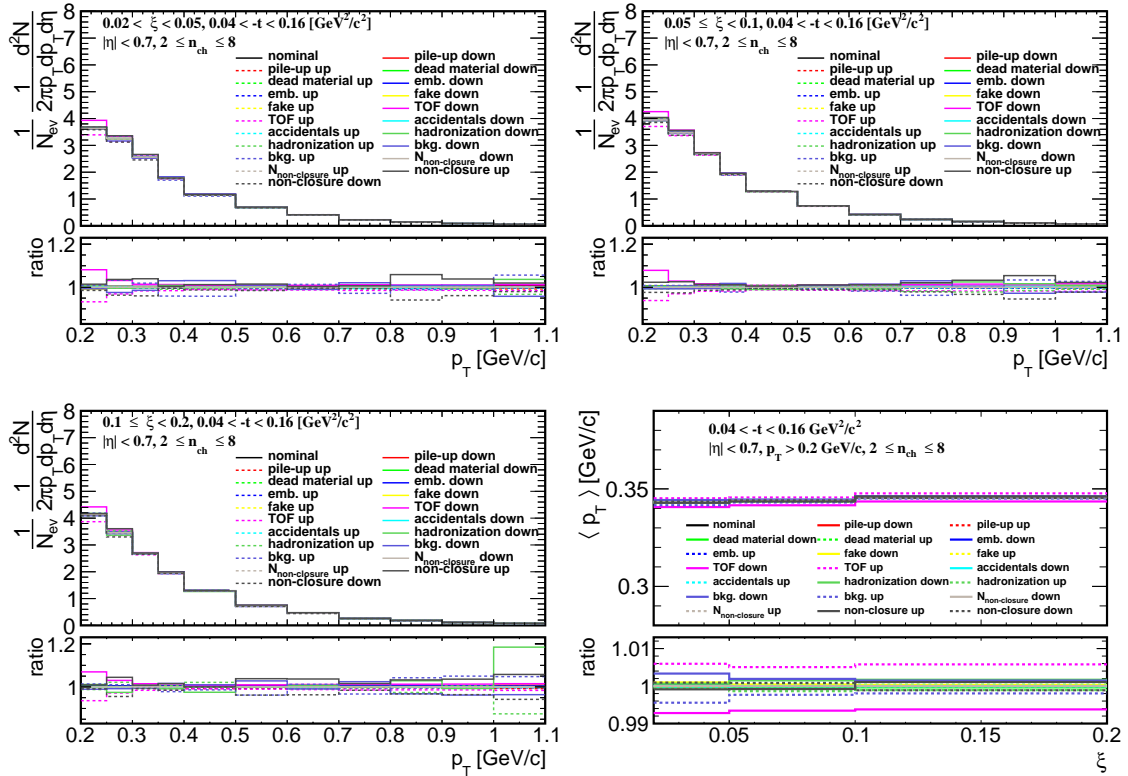

Figure 9.2: Components of the systematic uncertainties for p_T distributions in three ξ regions and for an average p_T distribution.
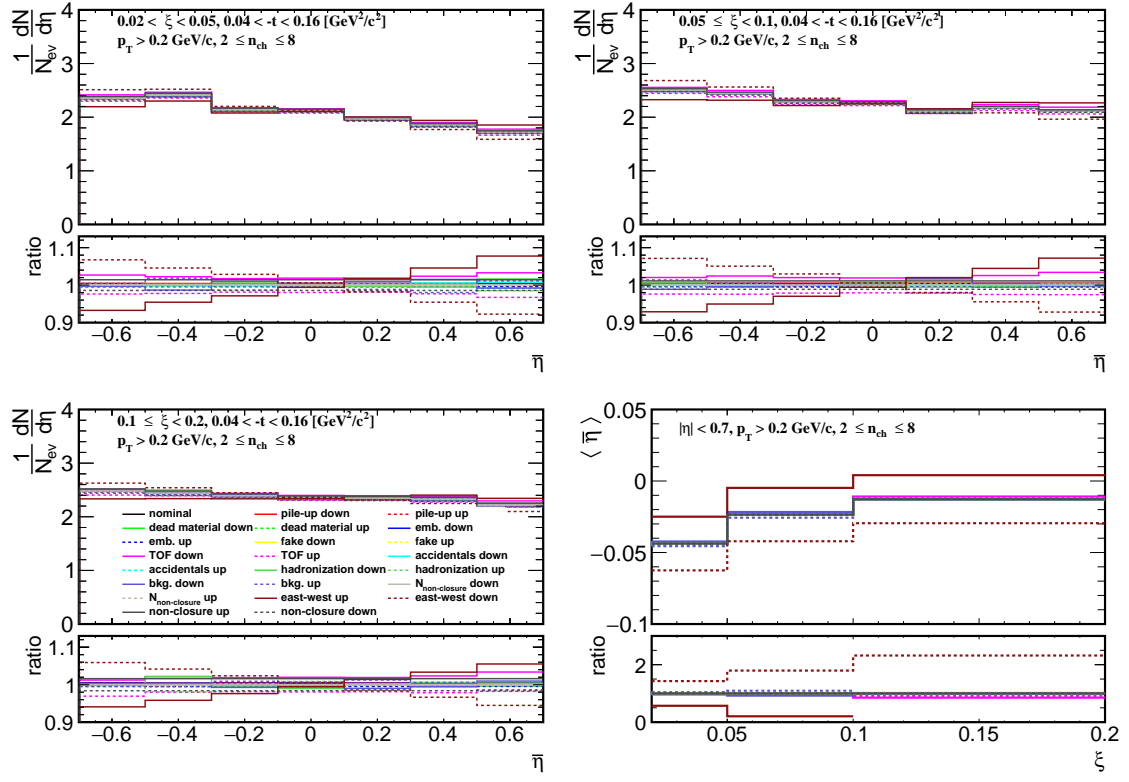
Figure 9.3: Components of the systematic uncertainties for $\bar{\eta}$ distributions in three ξ regions and for an average $\bar{\eta}$ distribution.
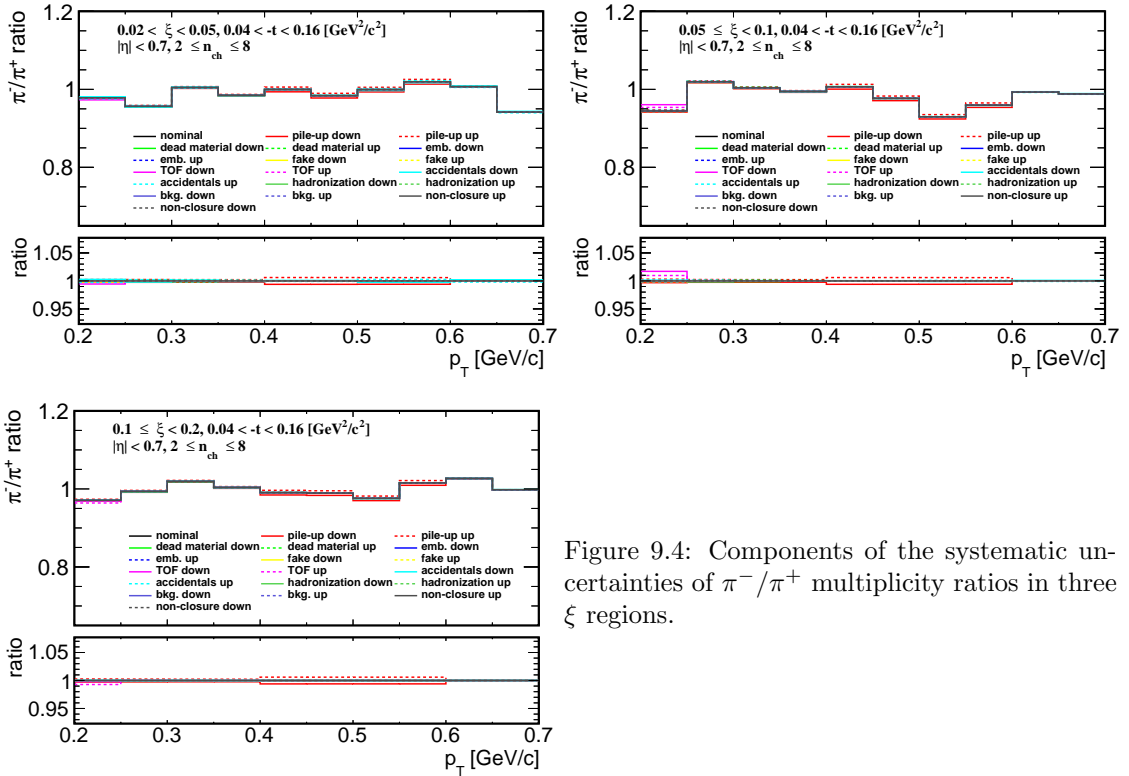

Figure 9.4: Components of the systematic uncertainties of π^-/π^+ multiplicity ratios in three ξ regions.
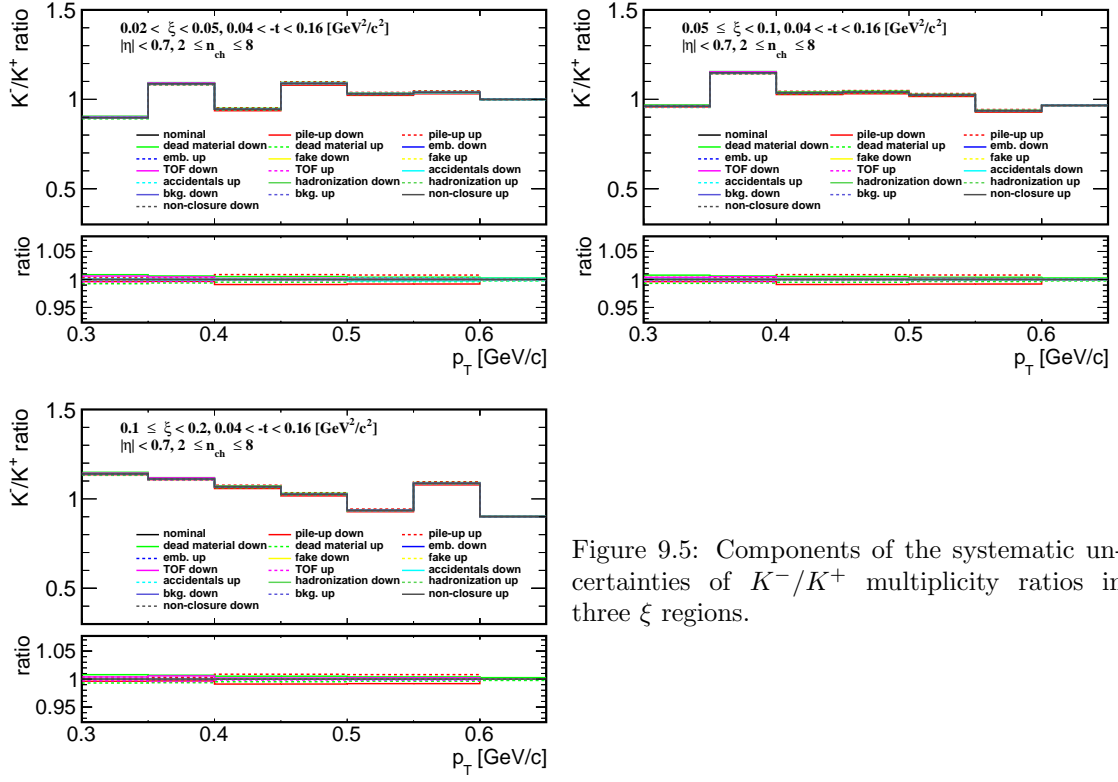
Figure 9.5: Components of the systematic uncertainties of K^-/K^+ multiplicity ratios in three ξ regions.
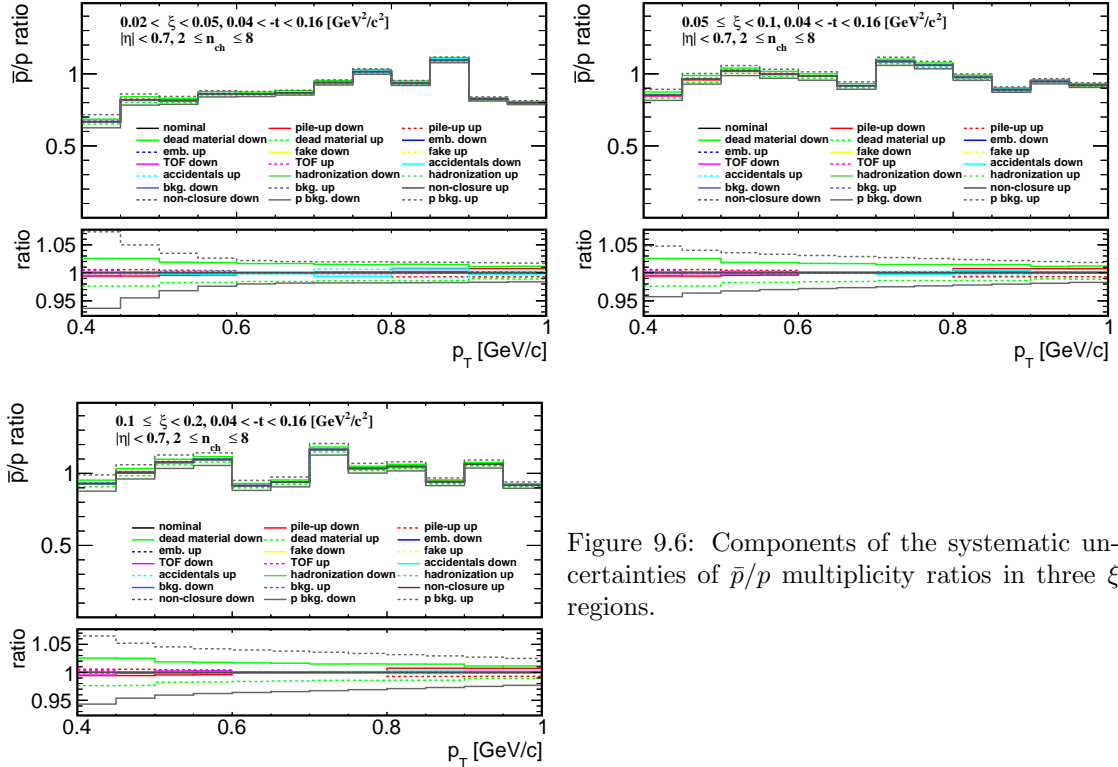
Figure 9.6: Components of the systematic uncertainties of $\bar{p}/p$ multiplicity ratios in three ξ regions.
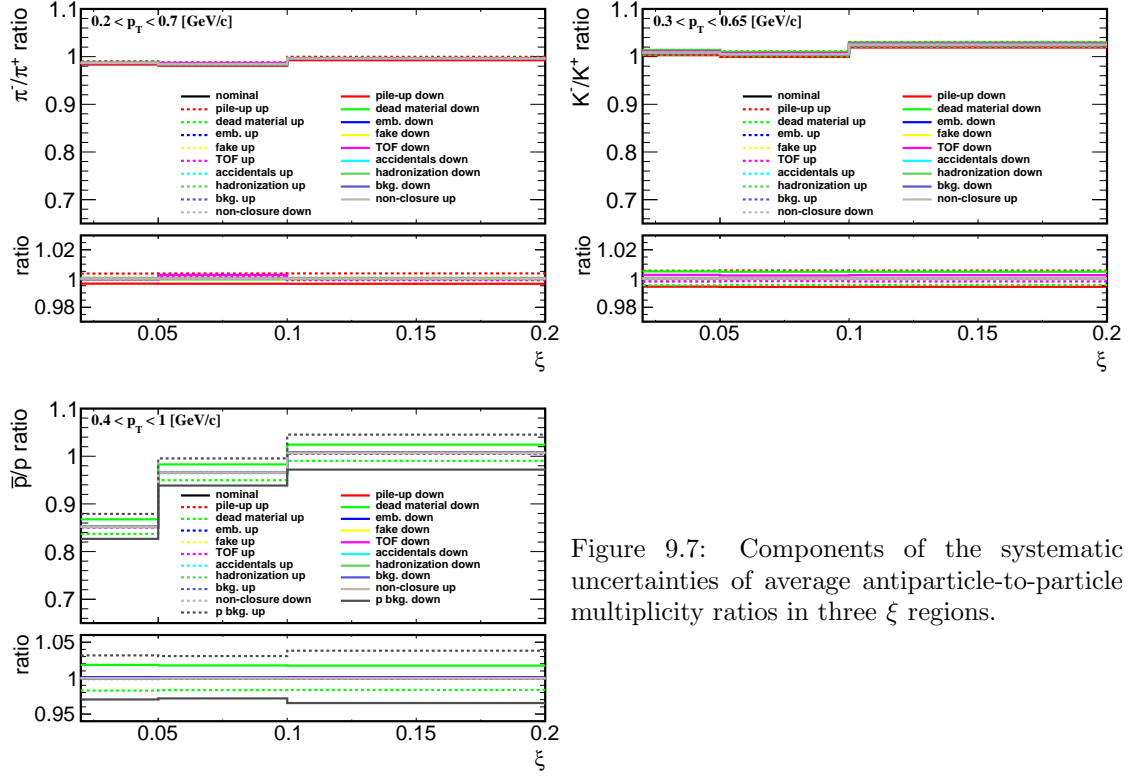
Figure 9.7: Components of the systematic uncertainties of average antiparticle-to-particle multiplicity ratios in three ξ regions.

10. Results

In the following section, the final-state charged particle distributions are compared with various SD MC predictions, i.e.

- PYTHIA 8 4C (SaS),

- PYTHIA 8 A2 (MBR),

- PYTHIA 8 A2 (MBR-tuned): expectations obtained without arbitrary suppression of diffractive cross sections at relatively large ξ,

- HERWIG 7,

- EPOS LHC with combined two classes of processes: diffractive (EPOS-SD) modelled by Pomeron exchange and non-diffractive modelled by low mass excitation of the proton remnant (EPOS-SD$'$).
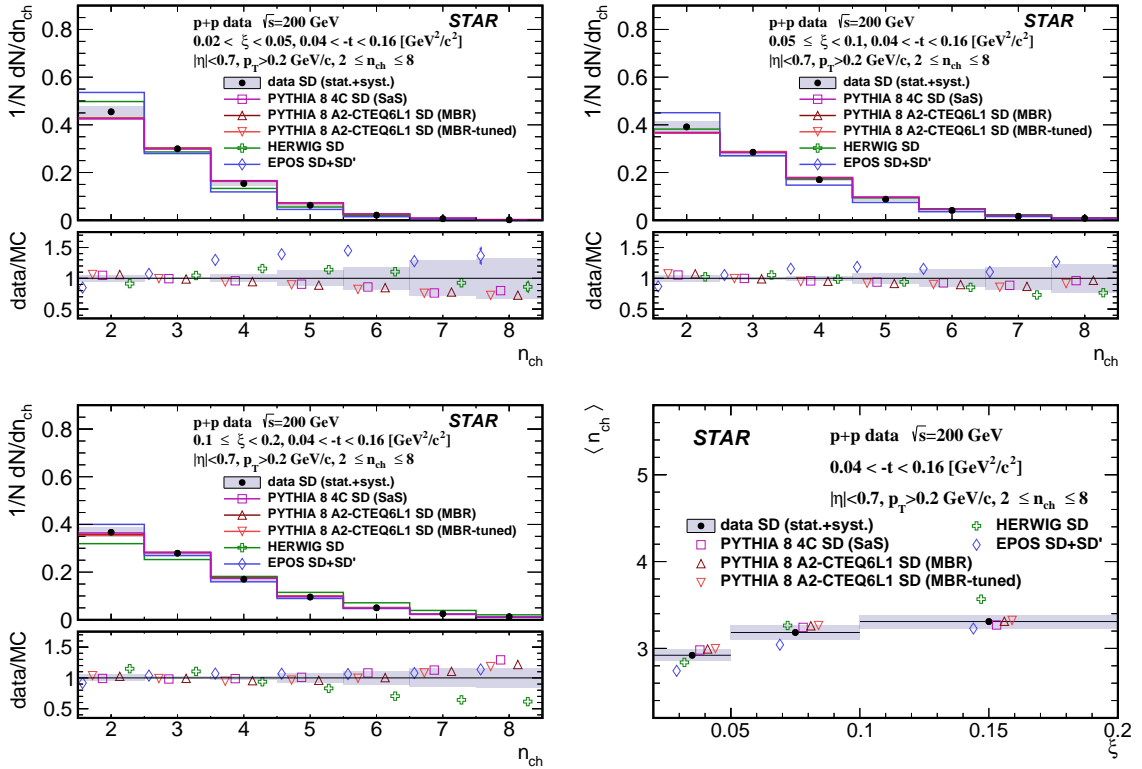
Figure 10.1: Primary charged-particle multiplicity shown separately for the three ranges of ξ: (top left) $0.02 < \xi < 0.05$, (top right) $0.05 < \xi < 0.1$, (bottom left) $0.1 < \xi < 0.2$ and (bottom right) the mean multiplicity $\langle n_{ch} \rangle$ as a function of ξ.

In all figures, data are shown as solid points with error bars representing the statistical uncertainties. Gray boxes represent statistical and systematic uncertainties added in quadrature. Predictions from MC models are shown as colour histograms and markers. The lower panel in each figure shows the ratio of data to the models' predictions. All results are presented separately for three ranges of ξ: $0.02 < \xi < 0.05$, $0.05 < \xi < 0.1$, $0.1 < \xi < 0.2$.

49

Figure 10.1 shows primary charged-particle multiplicity separately for the three ranges of ξ and the mean multiplicity $\langle n_{\rm ch} \rangle$ as a function of ξ. Data follow the expected increase of $\langle n_{\rm ch} \rangle$ with ξ due to the larger diffractive masses probed by increasing ξ in SD process. The shapes of the measured distributions are reproduced reasonably well by all models except EPOS SD+SD$'$ which predicts smaller $\langle n_{\rm ch} \rangle$ for $0.02 < \xi < 0.1$ and HERWIG-SD which for $0.1 < \xi < 0.2$ predicts too large $\langle n_{\rm ch} \rangle$.
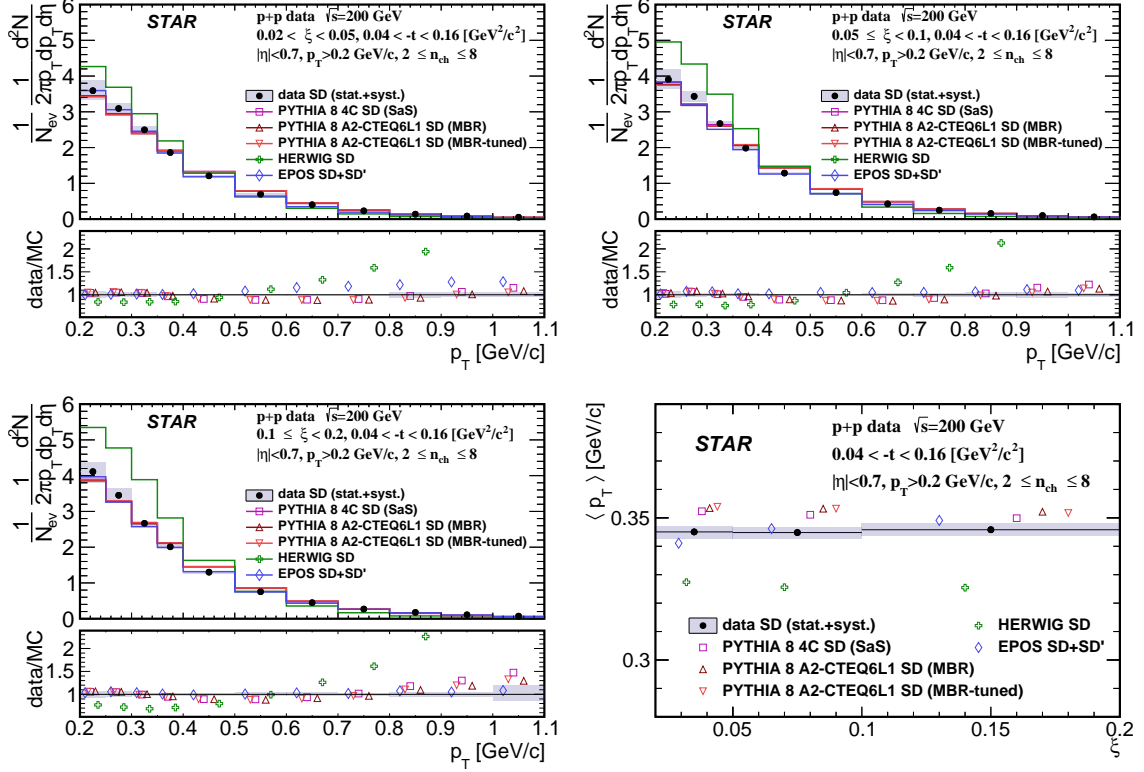
Figure 10.2: Primary charged-particle multiplicities as a function of $p_{\rm T}$ shown separately for the three ranges of ξ: (top left) $0.02 < \xi < 0.05$, (top right) $0.05 < \xi < 0.1$, (bottom left) $0.1 < \xi < 0.2$ and (bottom right) the mean transverse momentum $\langle p_{\rm T} \rangle$ as a function of ξ.

Figure 10.2 shows primary charged-particle multiplicities as a function of $p_{\rm T}$ separately for the three ranges of ξ and the mean transverse momentum $\langle p_{\rm T} \rangle$ as a function of ξ. Data show that $\langle p_{\rm T} \rangle$ depends very weakly on ξ. Models describe data fairly well except HERWIG-SD which predicts much steeper dependence of particle density with $p_{\rm T}$ in all three ξ ranges.

Figure 10.3 shows primary charged-particle multiplicity as a function of $\bar{\eta}$ (defined in Sec. **??**) separately for the three ranges of ξ and the mean pseudorapidity $\langle \bar{\eta} \rangle$ as a function of ξ. Data show expected flattening of the $\bar{\eta}$ distribution with increasing ξ which reflects SD event-asymmetry and fact that the gap-edge at large ξ is outside $|\bar{\eta}| < 0.7$ region leading to more flat distribution of particle density as a function of $\bar{\eta}$. Models describe data fairly well.

Figure 10.4 shows the ratio of production yields of π^-/π^+ as a function of $p_{\rm T}$ separately for the three ranges of ξ. Data in all three ξ ranges are consistent with equal amounts of π^+ and π^- with no significant $p_{\rm T}$ dependence. Models agree with data (except HERWIG) predicting on average small deviation from unity by $\sim 2\%$ what is smaller than data uncertainties. HERWIG in first two ξ ranges predicts too large asymmetry between π^+ and π^-.

Figure 10.5 shows the ratio of production yields of K^-/K^+ as a function of $p_{\rm T}$ separately for the three ranges of ξ . Data in all three ξ ranges are consistent with equal amounts of K^+ and K^- with no $p_{\rm T}$ dependence. Models agree with data except HERWIG in the first ξ range predicting
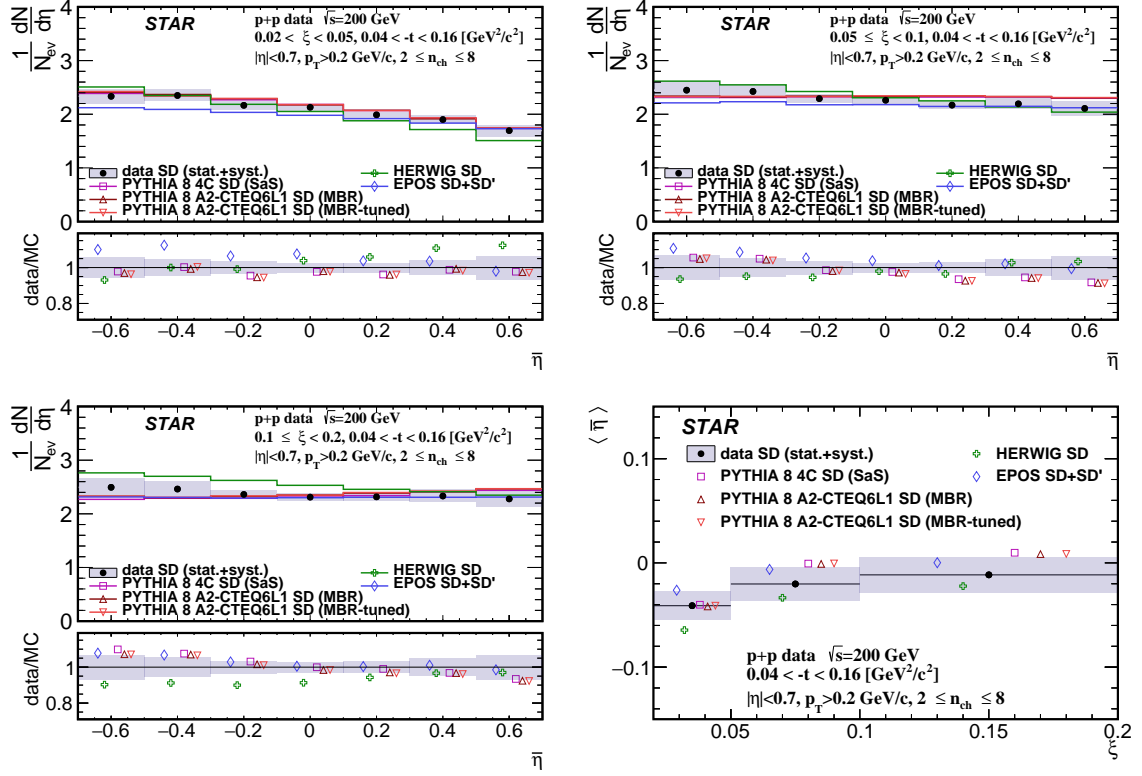
Figure 10.3: Primary charged-particle multiplicity as a function of $\bar{\eta}$ shown separately for the three ranges of ξ: (top left) $0.02 < \xi < 0.05$, (top right) $0.05 < \xi < 0.1$, (bottom left) $0.1 < \xi < 0.2$ and (bottom right) the mean pseudorapidity $\langle \bar{\eta} \rangle$ as a function of ξ.

too large ratio of K^- to K^+.

Figure 10.6 shows the ratio of production yields of $\bar{p}/p$ as a function of p_T separately for the three ranges of ξ. Data in the last two ξ ranges are consistent with equal amounts of p and $\bar{p}$ with no p_T dependence. However, in the first ξ range at $p_T < 0.7$ GeV/c data shows significant deviation from unity indicating a significant transfer of the baryon number from the forward to the central region. PYTHIA8 and EPOS SD+SD' agree with data in the last two ξ ranges. In first ξ range PYTHIA8 predicts small deviation from unity by $\sim 5\%$ which is smaller than observed in data, whereas EPOS SD+SD' predicts an asymmetry between $\bar{p}$ and p of $\sim 30\%$ which is larger than observed in data except $p_T < 0.5$ GeV/c. HERWIG predicts much larger baryon number transfer compared to data in first two ξ ranges and shows consistency with data in last ξ range.

Figure 10.7 shows mean ratio of production yields of π^-/π^+, K^-/K^+ and $\bar{p}/p$ as a function of ξ.
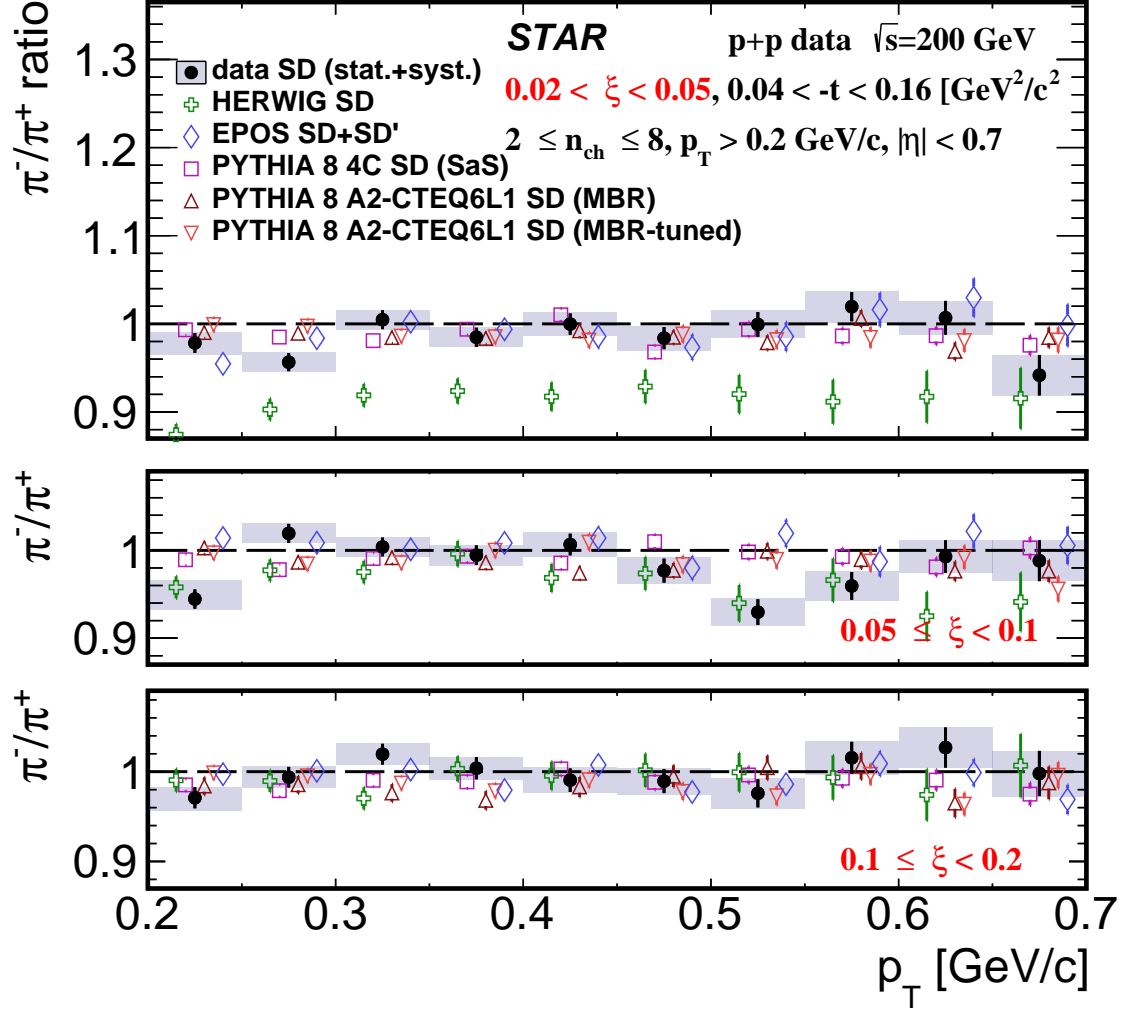
Figure 10.4: Ratio of production yields of π^-/π^+ as a function of p_T shown separately for the three ranges of ξ: (top) $0.02 < \xi < 0.05$, (middle) $0.05 < \xi < 0.1$, (bottom) $0.1 < \xi < 0.2$.
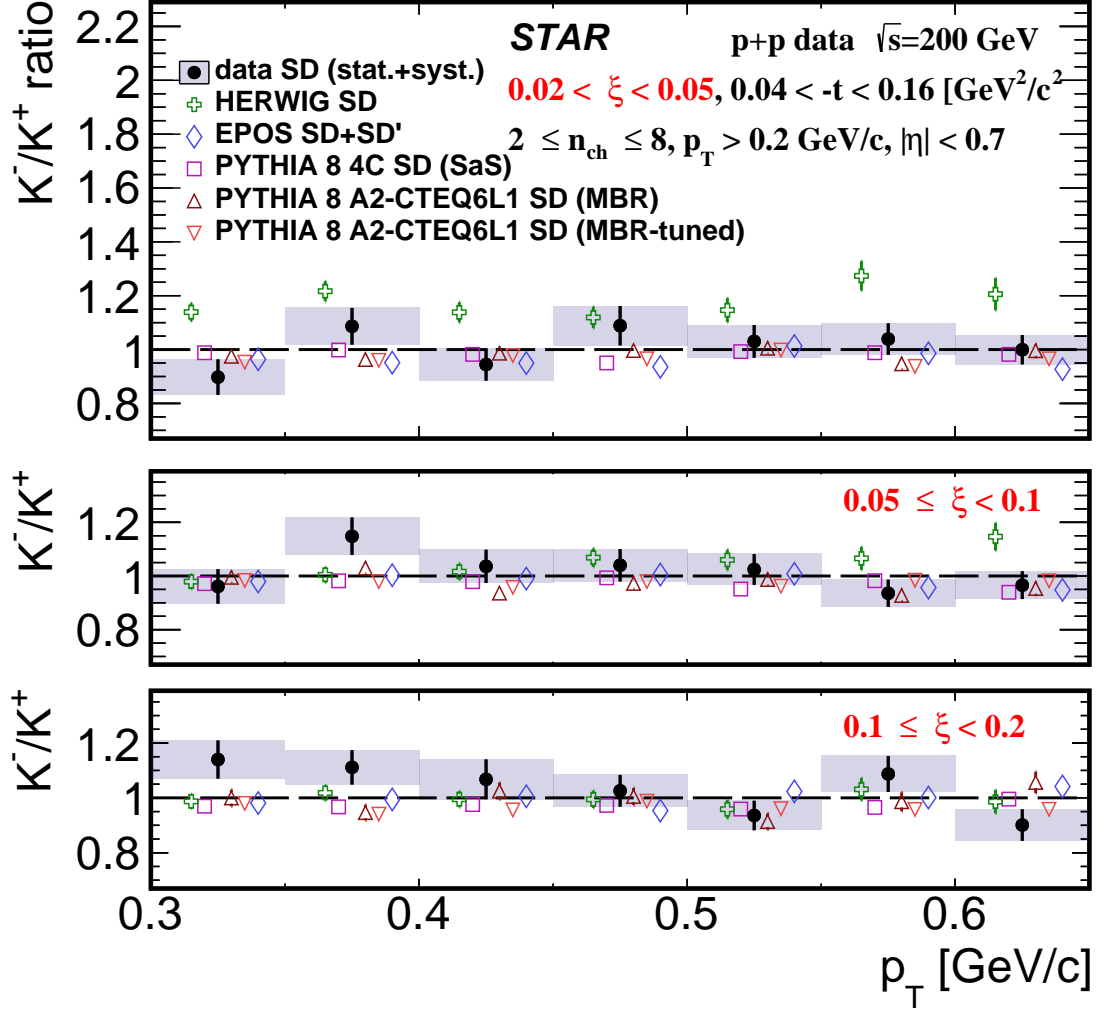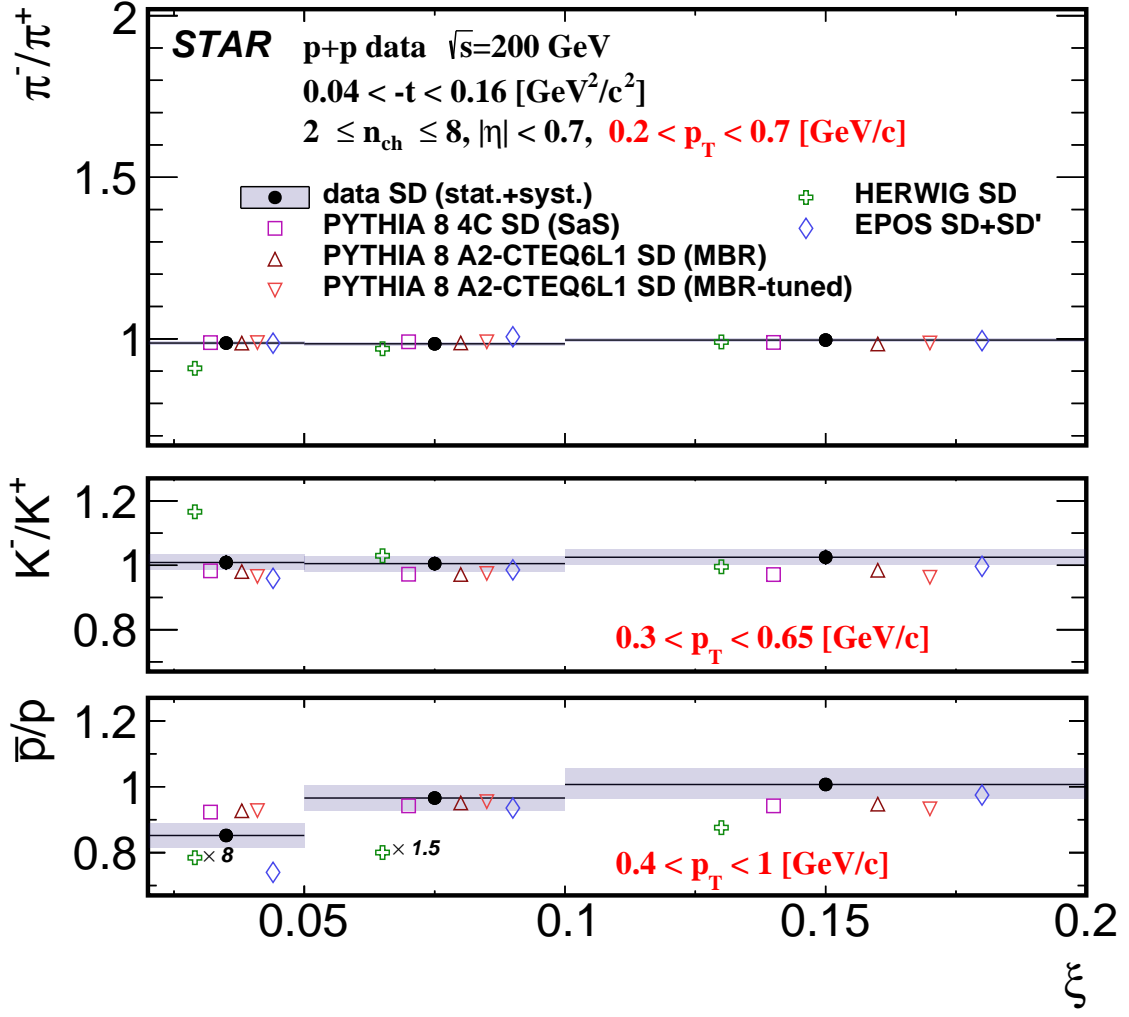
Figure 10.5: Ratio of production yields of K^-/K^+ as a function of p_T shown separately for the three ranges of ξ: (top) $0.02 < \xi < 0.05$, (middle) $0.05 < \xi < 0.1$, (bottom) $0.1 < \xi < 0.2$.
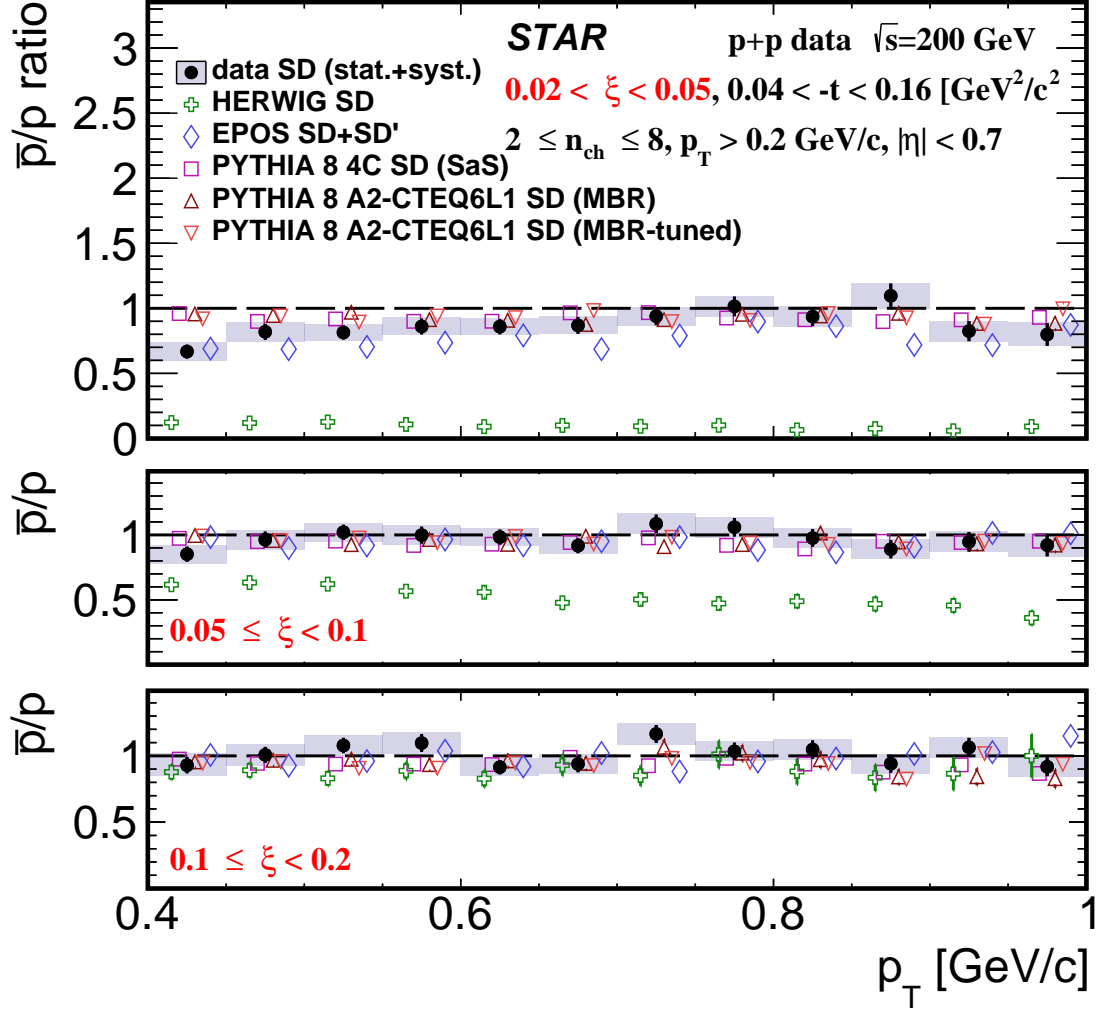
Figure 10.6: Ratio of production yields of $\bar{p}/p$ as a function of p_T shown separately for the three ranges of ξ: (top) $0.02 < \xi < 0.05$, (middle) $0.05 < \xi < 0.1$, (bottom) $0.1 < \xi < 0.2$.

Figure 10.7: Ratio of production yields of π^-/π^+, K^-/K^+ and $\bar{p}/p$ as a function of ξ.

11. Summary and Conclusions

Inclusive and identified (pion, kaon, proton and their antiparticles) charged particle production in Single Diffractive Dissociation process has been measured in proton-proton collisions at $\sqrt{s} = 200$ GeV with the STAR detector at RHIC using data corresponding to an integrated luminosity of 15 nb^{-1}.

Significant differences are observed between the measured distributions of ξ and Monte Carlo model predictions. Amongst the models considered EPOS and PYTHIA8 (MBR) without suppression of diffractive cross sections at large ξ provide the best description of the data.

Primary-charged-particle multiplicity and its density as a function of pseudorapidity and transverse momentum are well described by PYTHIA8 and EPOS-SD$'$ models. EPOS-SD and HERWIG do not describe the data.

π^-/π^+ and K^-/K^+ production ratios are close to unity and consistent with most of model predictions except for EPOS-SD and HERWIG.

$\bar{p}/p$ production ratio shows a significant deviation from unity in the $0.02 < \xi < 0.05$ range indicating a non-negligible transfer of the baryon number from the forward to the central region. Equal amount of protons and antiprotons are observed in the $\xi > 0.05$ range. PYTHIA8 and EPOS-SD$'$ agree with data for $\xi > 0.05$. For $0.02 < \xi < 0.05$ they predict small deviations from unity (0.93) which is however higher than observed in data (0.86 ± 0.02). HERWIG and EPOS-SD predict much larger baryon number transfers compared to data for $\xi < 0.1$ and show consistency with data for $\xi > 0.1$.

Bibliography

[1] L. Adamczyk, L. Fulek, and R. Sikora, *Supplementary note on diffractive analyses of 2015 proton-proton data*, `https://drupal.star.bnl.gov/STAR/starnotes/private/psn0732`, July, 2019.

[2] B. Z. Kopeliovich and B. G. Zakharov, *Novel Mechanisms of Baryon Number Flow Over Large Rapidity Gap*, Z. Phys. **C43** (1989) 241.

[3] F. W. Bopp, *Baryon transport in dual models and the possibility of a backward peak in diffraction*, in *New trends in high-energy physics: Experiment, phenomenology, theory. Proceedings, International School-Conference, Crimea 2000, Yalta, Ukraine, May 27-June 4, 2000.* `arXiv:hep-ph/0007229 [hep-ph]`.

[4] M. Anderson et al., *The STAR Time Projection Chamber: A Unique tool for studying high multiplicity events at RHIC*, Nucl. Instrum. Meth. **A499** (2003) 659–678.

[5] R. Brun, F. Bruyant, M. Maire, A. C. McPherson, and P. Zanarini, *GEANT3*, CERN-DD-EE-84-1 (1987).

[6] GEANT4 Collaboration, S. Agostinelli et al., *GEANT4: A Simulation toolkit*, Nucl. Instrum. Meth. **A506** (2003) 250–303.

[7] T. Sjöstrand, S. Mrenna, and P. Z. Skands, *PYTHIA 6.4 Physics and Manual*, JHEP **05** (2006) 026.

[8] R. Ciesielski and K. Goulianos, *MBR Monte Carlo Simulation in PYTHIA8*, PoS **ICHEP2012** (2013) 301, `arXiv:1205.1446 [hep-ph]`.

[9] W. Fischer, *Run Overview of the Relativistic Heavy Ion Collider*, `http://www.agsrhichome.bnl.gov/RHIC/Runs/`.

[10] STAR Collaboration, B. I. Abelev et al., *Systematic Measurements of Identified Particle Spectra in pp, d^+ Au and Au+Au Collisions from STAR*, Phys. Rev. **C79** (2009) 034909, `arXiv:0808.2041 [nucl-ex]`.

[11] ATLAS Collaboration, G. Aad et al., *Charged-particle distributions in $\sqrt{s} = 13$ TeV pp interactions measured with the ATLAS detector at the LHC*, Phys. Lett. **B758** (2016) 67–88.

[12] G. D'Agostini, *A Multidimensional unfolding method based on Bayes' theorem*, Nucl. Instrum. Meth. **A362** (1995) 487–498.

[13] H. Bichsel, *A method to improve tracking and particle identification in TPCs and silicon detectors*, Nucl. Instrum. Meth. **A562** (2006) 154–197.

Appendices

A. Acronyms

AGS   Alternating Gradient Synchrotron

AFP   ATLAS Forward Proton

ALFA   Absolute Luminosity For ATLAS

ATLAS   A Toroidal LHC Apparatus

BBC   Beam Beam Counter

BCID   Bunch Crossing Identifier

BEMC   Barrel Electromagnetic Calorimeter

BNL   Brookhaven National Laboratory

CD   Central Diffraction

CEP   Central Exclusive Production

CERN   European Laboratory for Particle Physics

CR   Colour Reconnection

DAQ   Data Acquisition System

DD   Double Diffractive

DIS   Deep Inelastic Scattering

DL   Donnachie and Landshoff

DPDFs   Diffractive Parton Distribution Functions

EBIS   Electron Beam Ion Source

FCAL   Forward Calorimeters

FSR   Final State Radiation

HCAL   Hadronic Calorimeter

HEC   Hadronic End-Cap

ECR   Electron Cyclotron Resonance

EM   Electromagnetic

HFT   Heavy Flavor Tracker

HLT   High Level Trigger

IBL   Insertable B-Layer

ID   Inner Detector

IP   Interaction Point

ISR   Initial State Radiation

L1   Level-1

907	**LAr**	liquid argon
908	**LEIR**	Low-Energy Ion Ring
909	**LEP**	Large Electron Positron Collider
910	**LHC**	Large Hadron Collider
911	**LION**	Laser Ion Source
912	**MAPMT**	Multi Anode Photomultiplier Tube
913	**MB**	Minimum Bias
914	**MBR**	Minimum Bias Rockefeller
915	**MBTS**	Minimum Bias Trigger Scintillator
916	**MPV**	Most Probable Value
917	**MC**	Monte Carlo
918	**MD**	Main Detector
919	**MPI**	Multiple Parton Interactions
920	**MRPC**	Multi-gap Resistive Plate Chambers
921	**MWPC**	Multi Wire Proportional Chambers
922	**ND**	Non-Diffraction
923	**OD**	Overlap Detector
924	**OPPIS**	Optically Pumped Polarized Ion Source
925	**PDFs**	Parton Distribution Functions
926	**PP0**	Patch Panel 0
927	**PP**	Patch Panel
928	**PS**	Proton Synchrotron
929	**PSB**	Proton Synchrotron Booster
930	**QCD**	Quantum Chromodynamics
931	**QED**	Quantum Electrodynamics
932	**QGP**	Quark Gluon Plasma
933	**QFT**	Quantum Field Theory
934	**RFQ**	Radio Frequency Quadrupole
935	**RHIC**	Relativistic Heavy Ion Collider
936	**ROI**	Regions-of-Interest
937	**RP**	Roman Pot
938	**SaS**	Schuler and Sjöstrand
939	**SCT**	Semiconductor Tracker

940	**SD**	Single Diffraction
941	**SM**	Standard Model
942	**SMD**	Shower Maximum Detector
943	**SPS**	Super Proton Synchrotron
944	**SSD**	Silicon Strip Detectors
945	**STAR**	Solenoidal Tracker at RHIC
946	**TDAQ**	Trigger and Data Acquisition
947	**TOF**	Time of Flight
948	**TPC**	Time Projection Chamber
949	**TRT**	Transition Radiation Tracker
950	**UE**	Underlying Events
951	**VPD**	Vertex Position Detector
952	**ZDC**	Zero Degree Calorimeter

B. Proton and Antiproton DCA Distributions
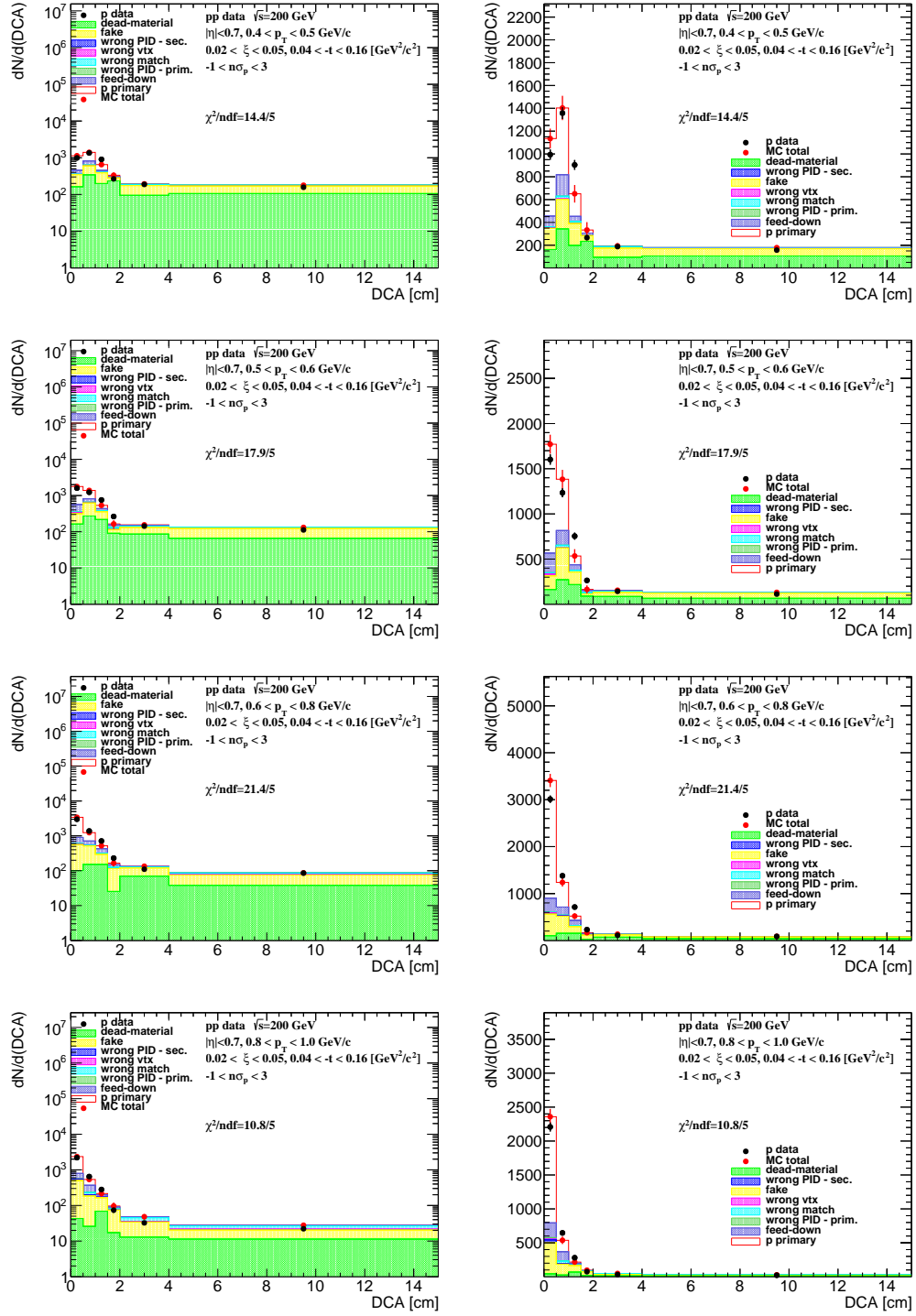
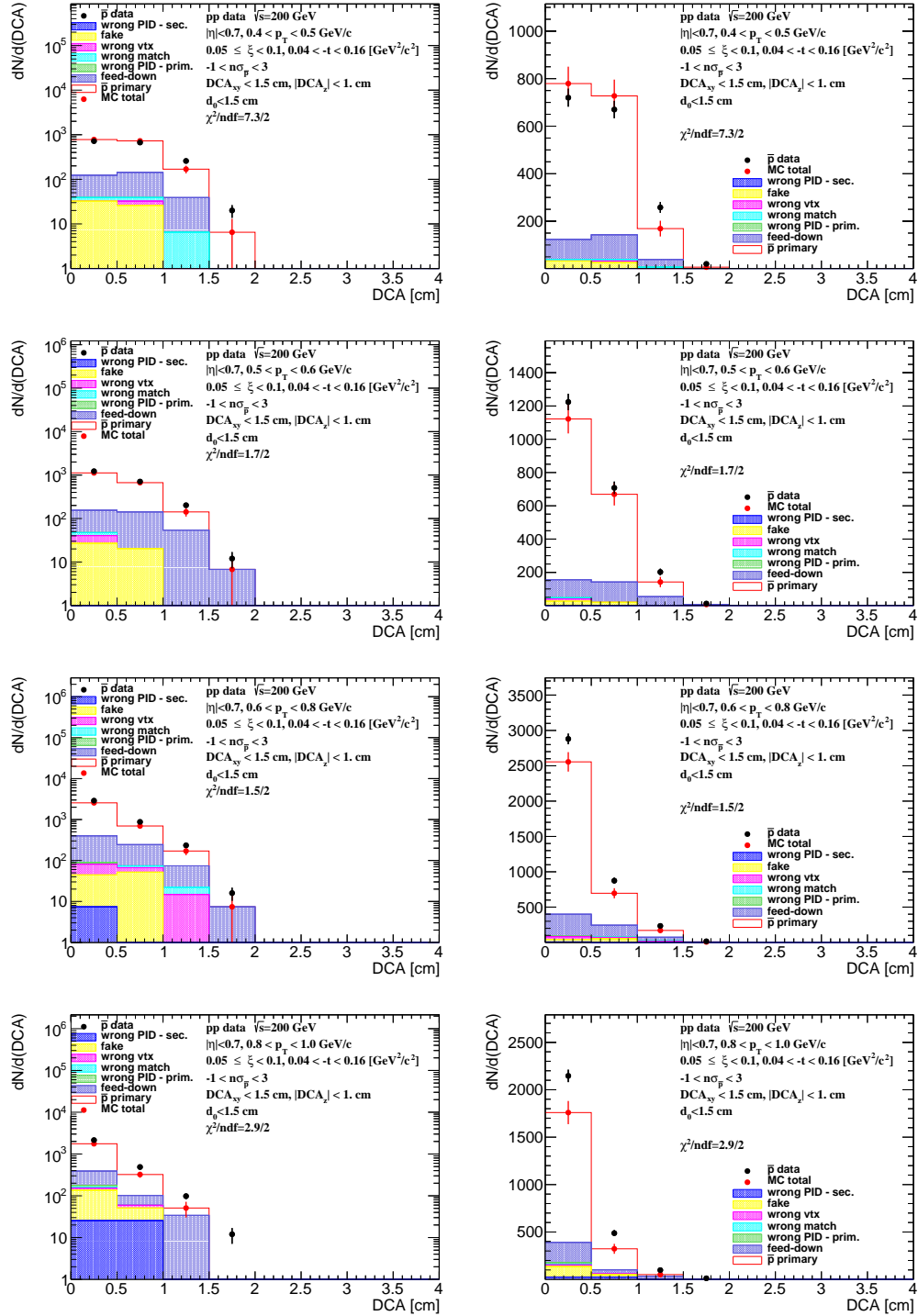Figure B.1: Distributions of DCA for protons in SD interactions with $0.02 < \xi < 0.05$ and loose selection.
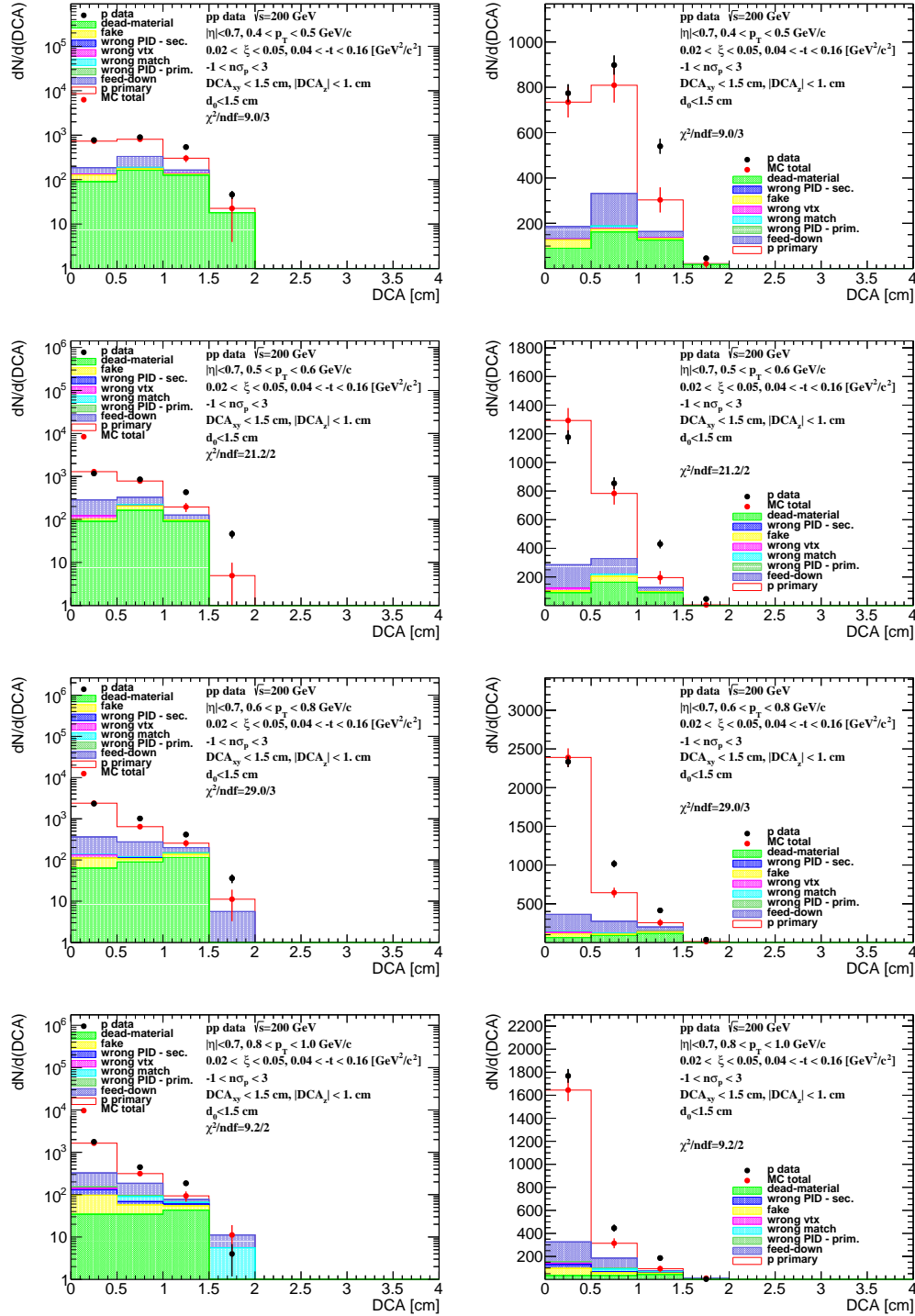
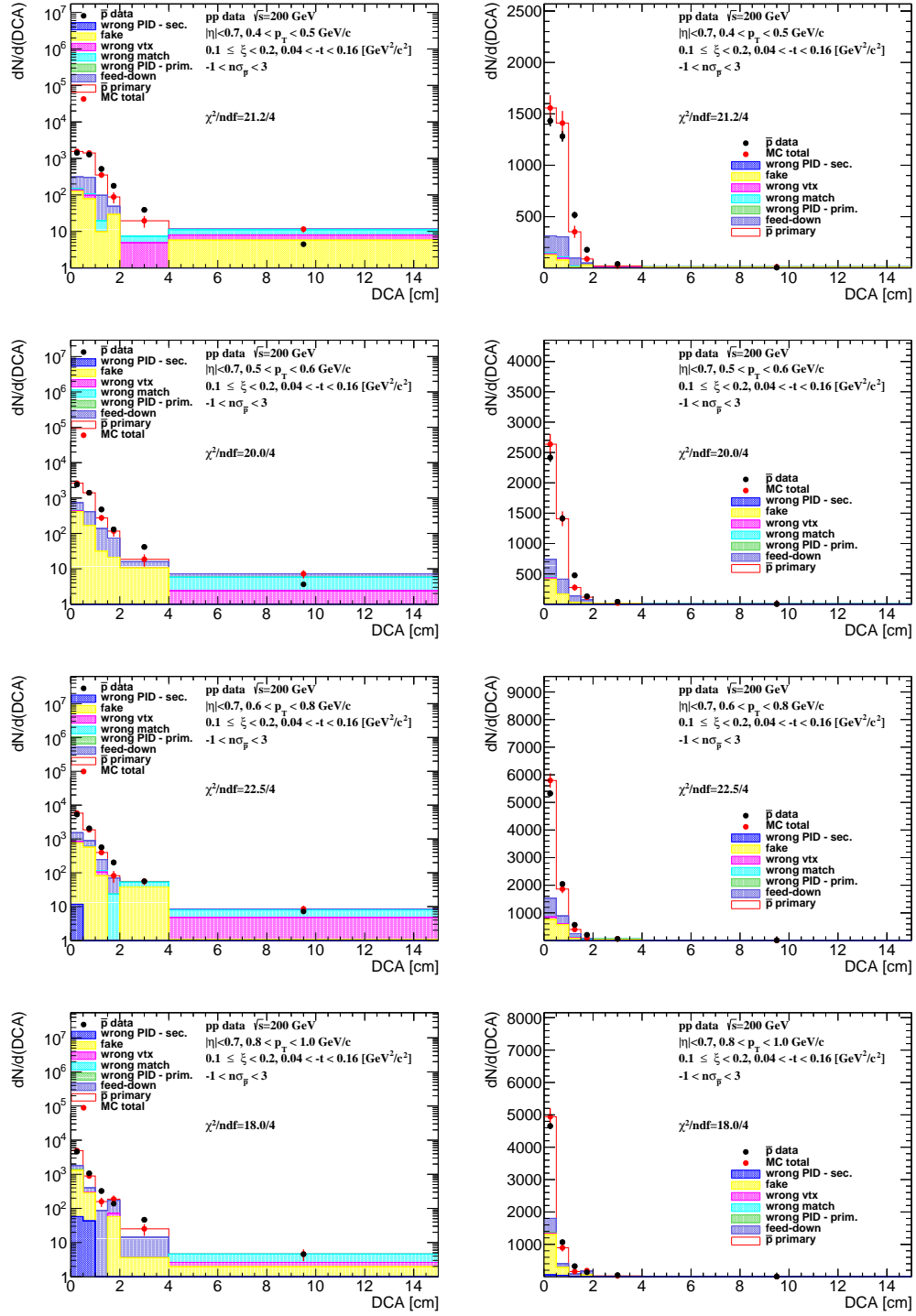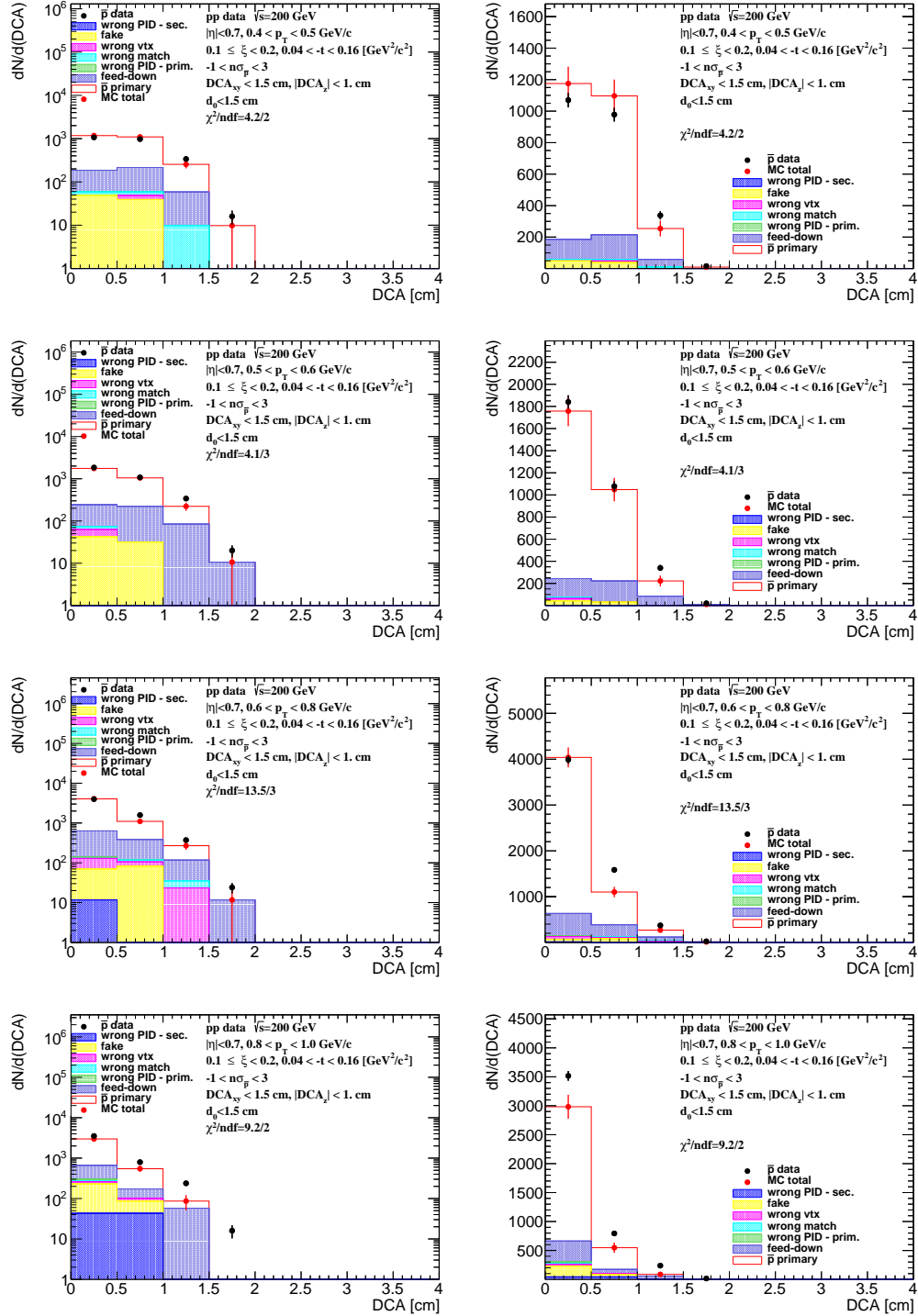Figure B.2: Distributions of DCA for protons in SD interactions with $0.02 < \xi < 0.05$ and normal selection.
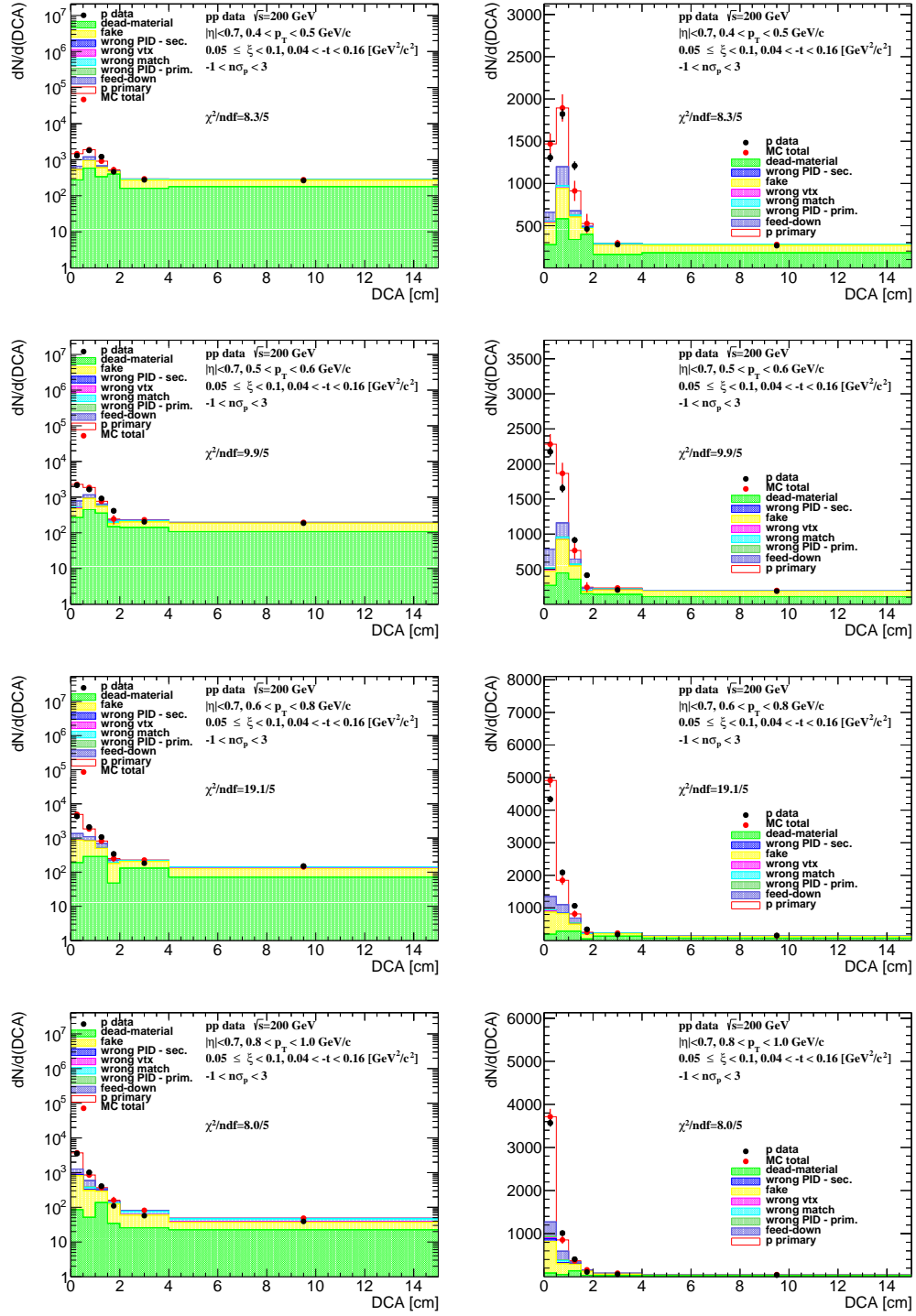
Figure B.3: Distributions of DCA for protons in SD interactions with $0.05 < \xi < 0.1$ and loose selection.
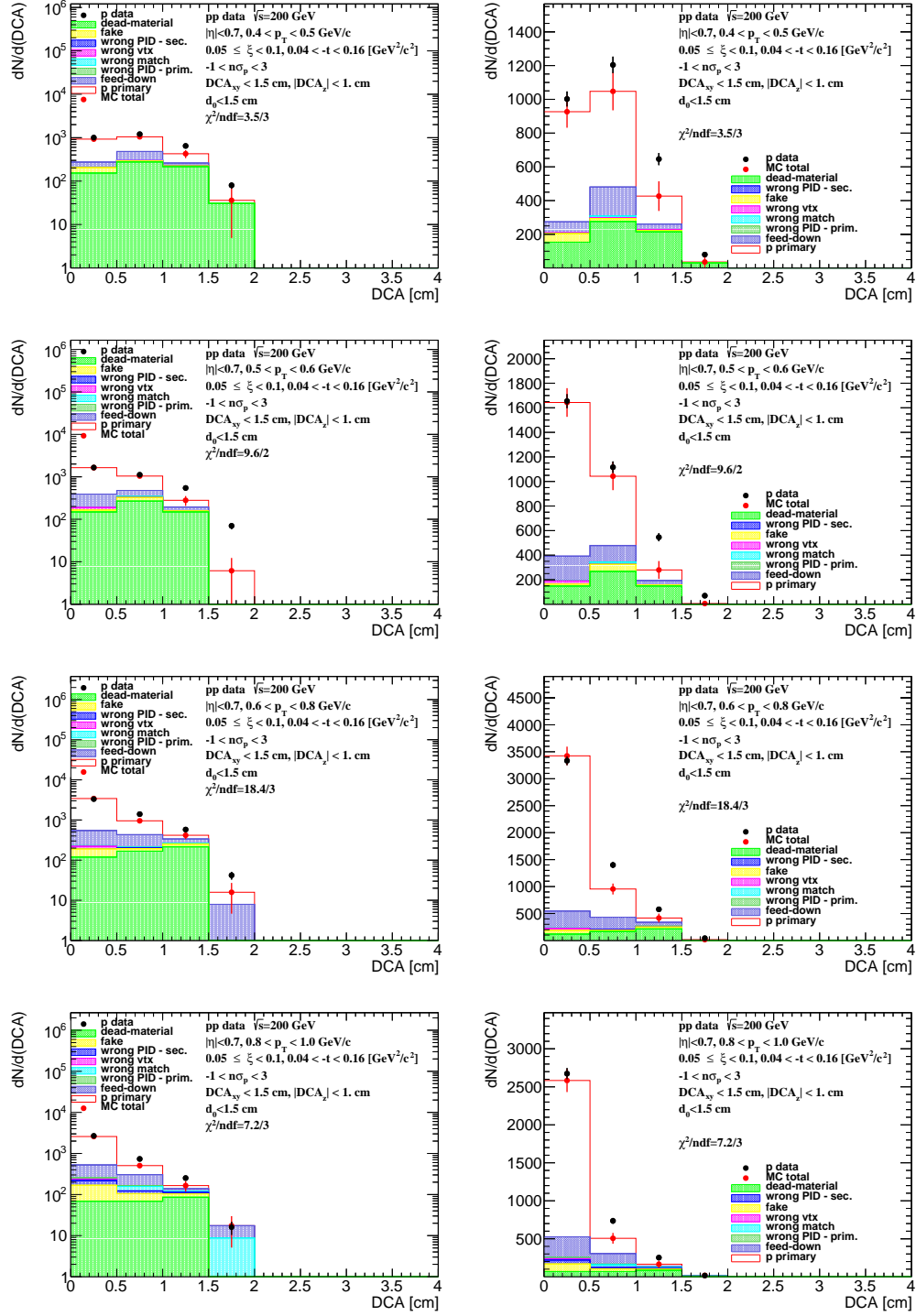
Figure B.4: Distributions of DCA for protons in SD interactions with $0.05 < \xi < 0.1$ and normal selection.
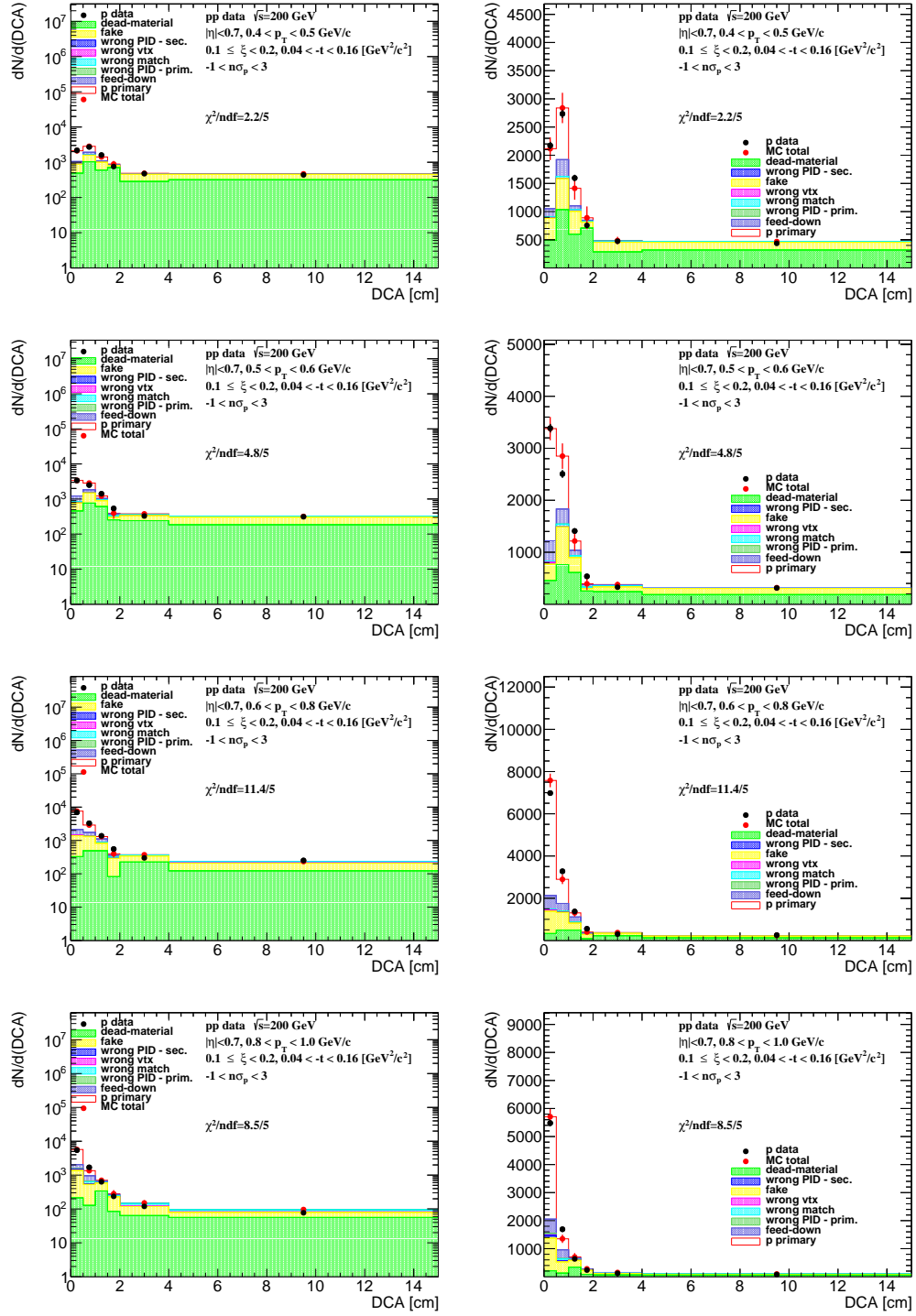
Figure B.5: Distributions of DCA for protons in SD interactions with $0.1 < \xi < 0.2$ and loose selection.
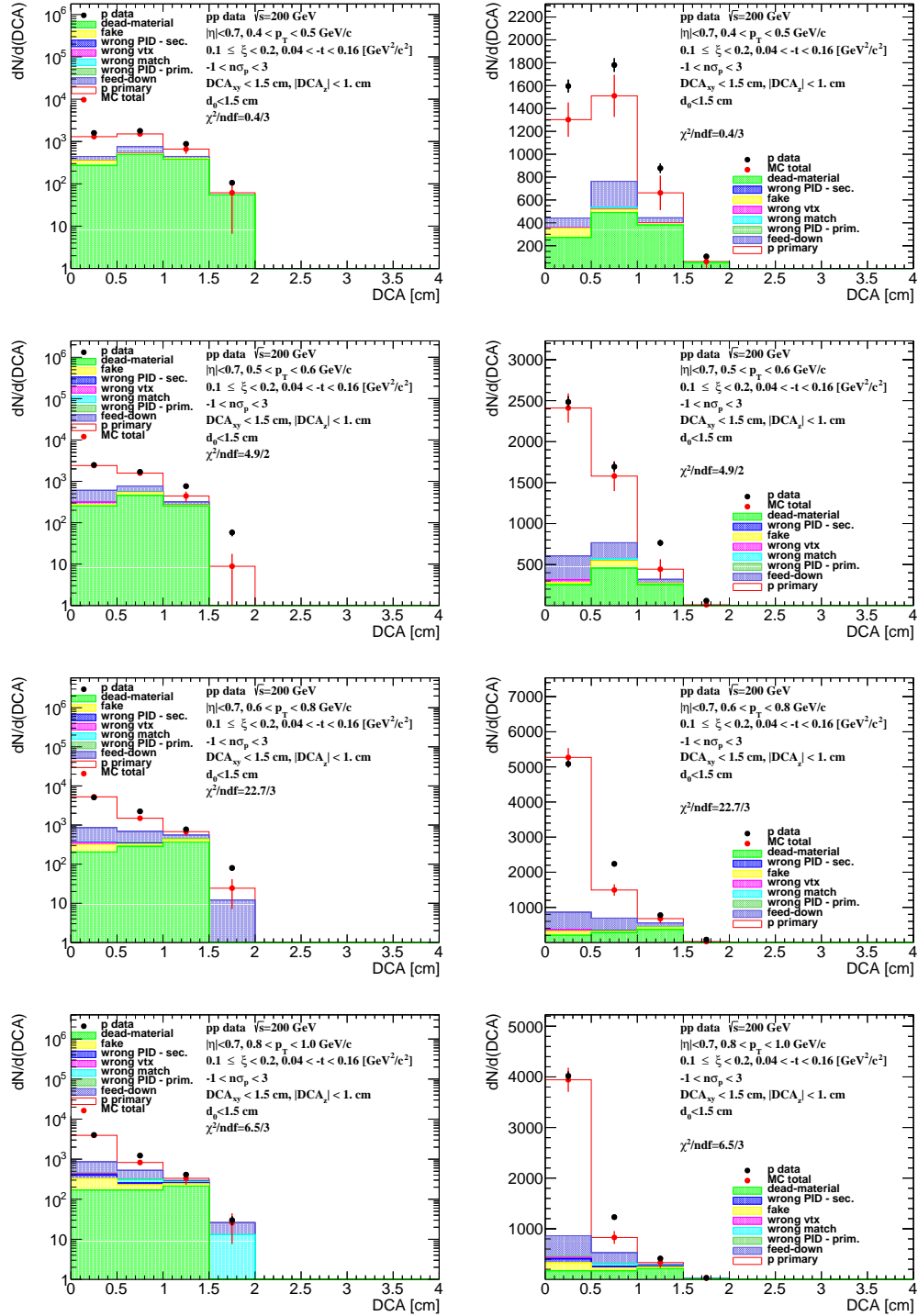
Figure B.6: Distributions of DCA for protons in SD interactions with $0.1 < \xi < 0.2$ and normal selection.
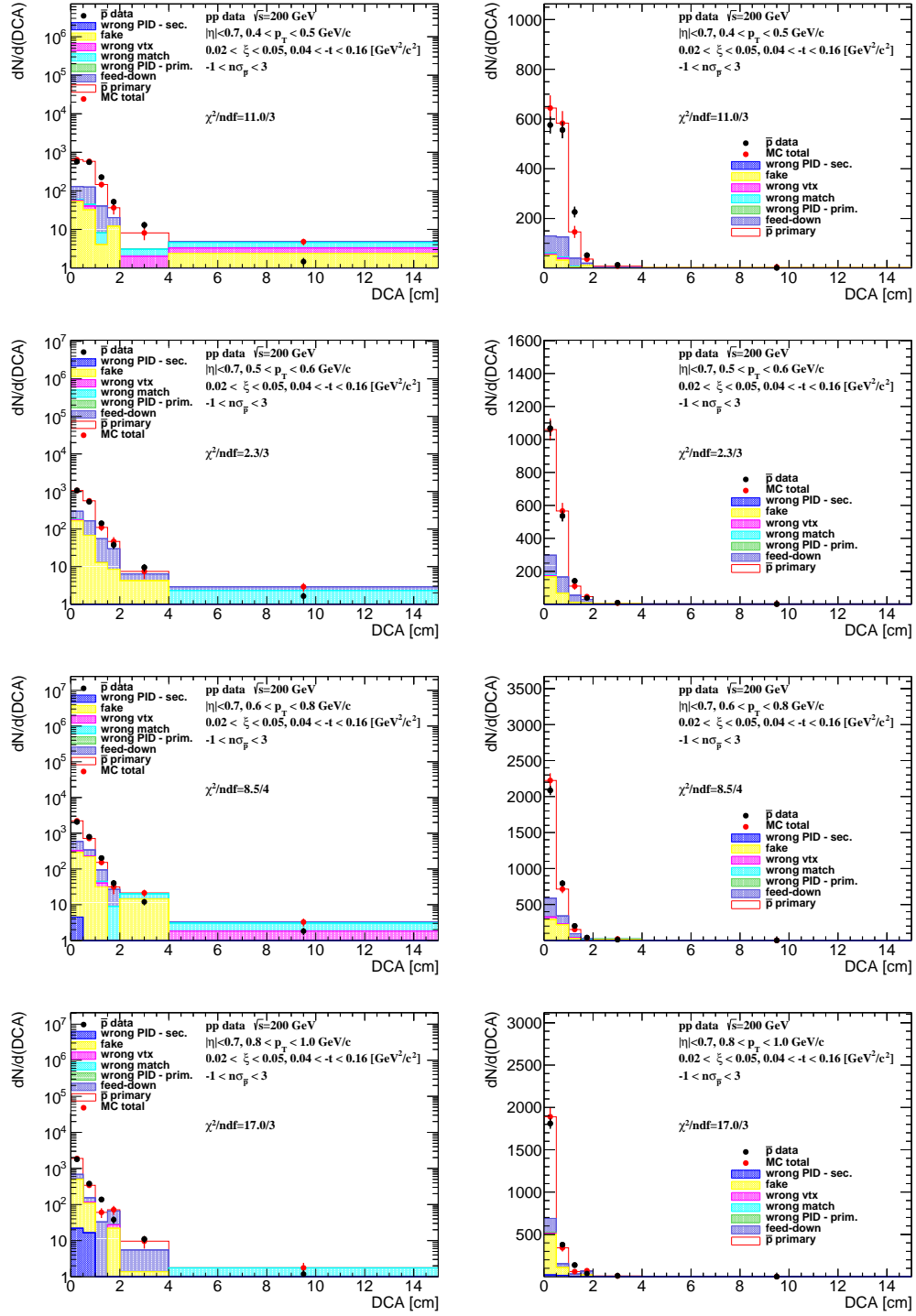
Figure B.7: Distributions of DCA for antiprotons in SD interactions with $0.02 < \xi < 0.05$ and loose selection.
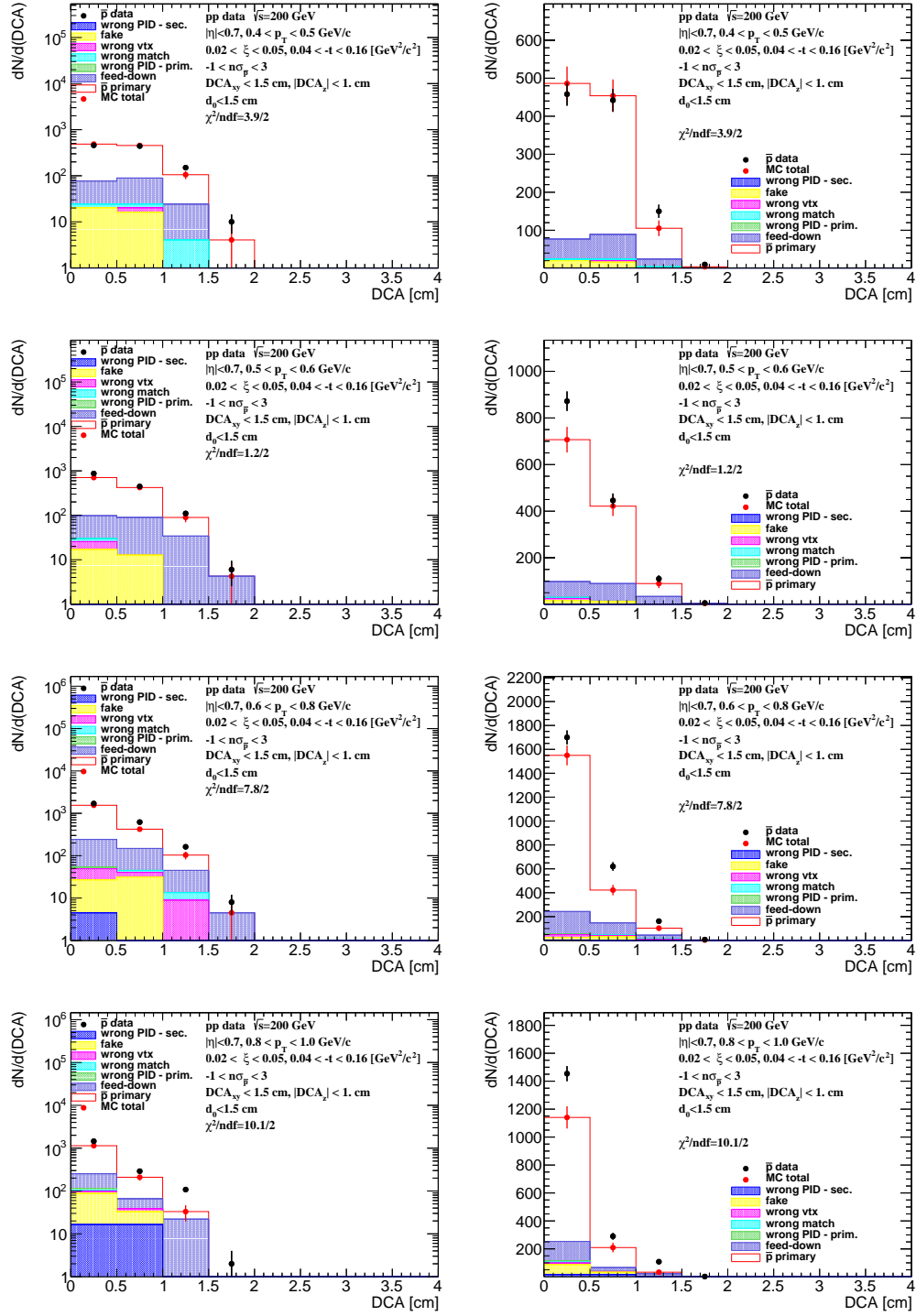
Figure B.8: Distributions of DCA for antiprotons in SD interactions with $0.02 < \xi < 0.05$ and normal selection.
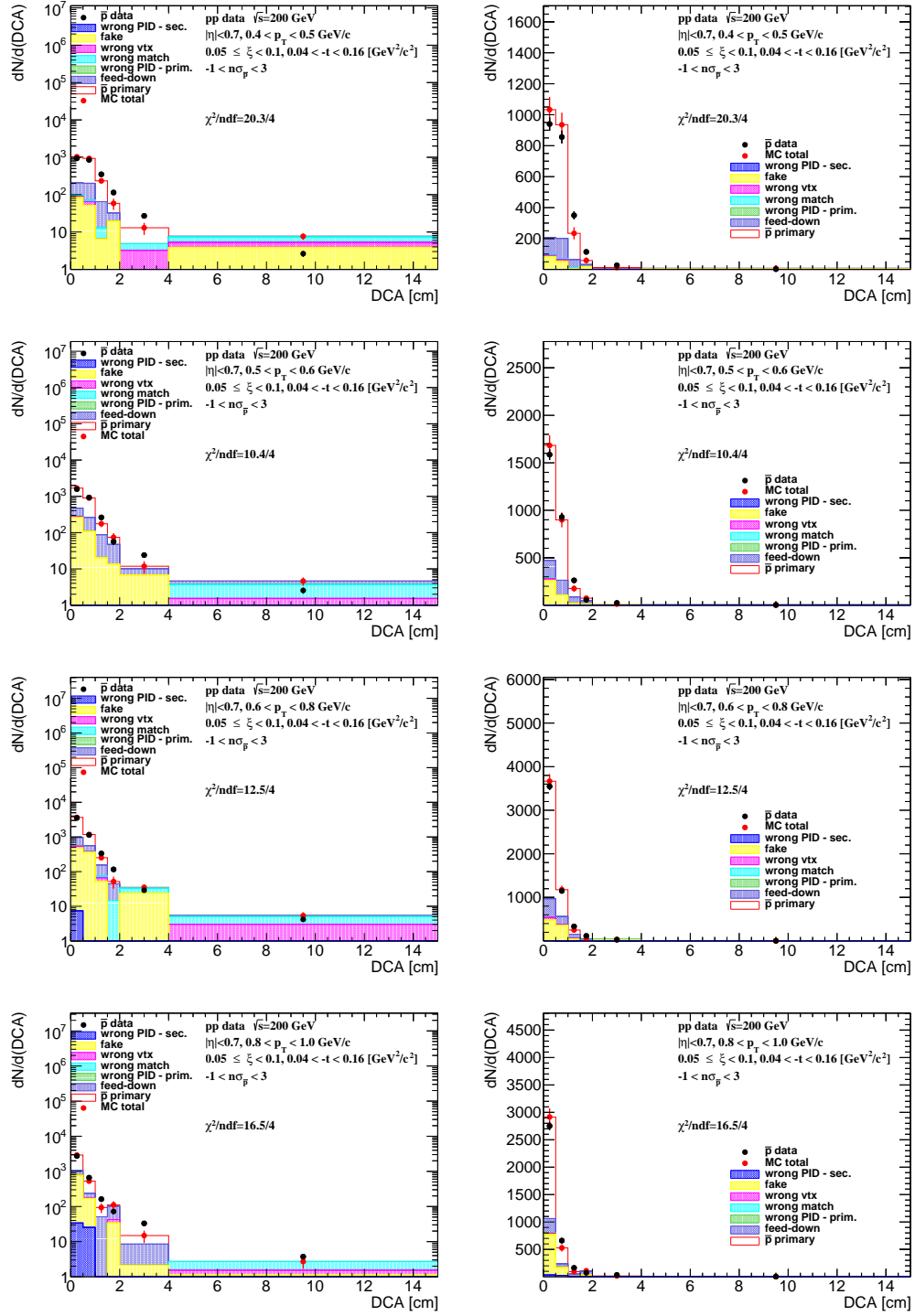
Figure B.9: Distributions of DCA for antiprotons in SD interactions with $0.05 < \xi < 0.1$ and loose selection.

Figure B.10: Distributions of DCA for antiprotons in SD interactions with $0.05 < \xi < 0.1$ and normal selection.

Figure B.11: Distributions of DCA for antiprotons in SD interactions with $0.1 < \xi < 0.2$ and loose selection.

Figure B.12: Distributions of DCA for antiprotons in SD interactions with $0.1 < \xi < 0.2$ and normal selection.

C. Distributions of $n\sigma^i_{dE/dx}$ in SD
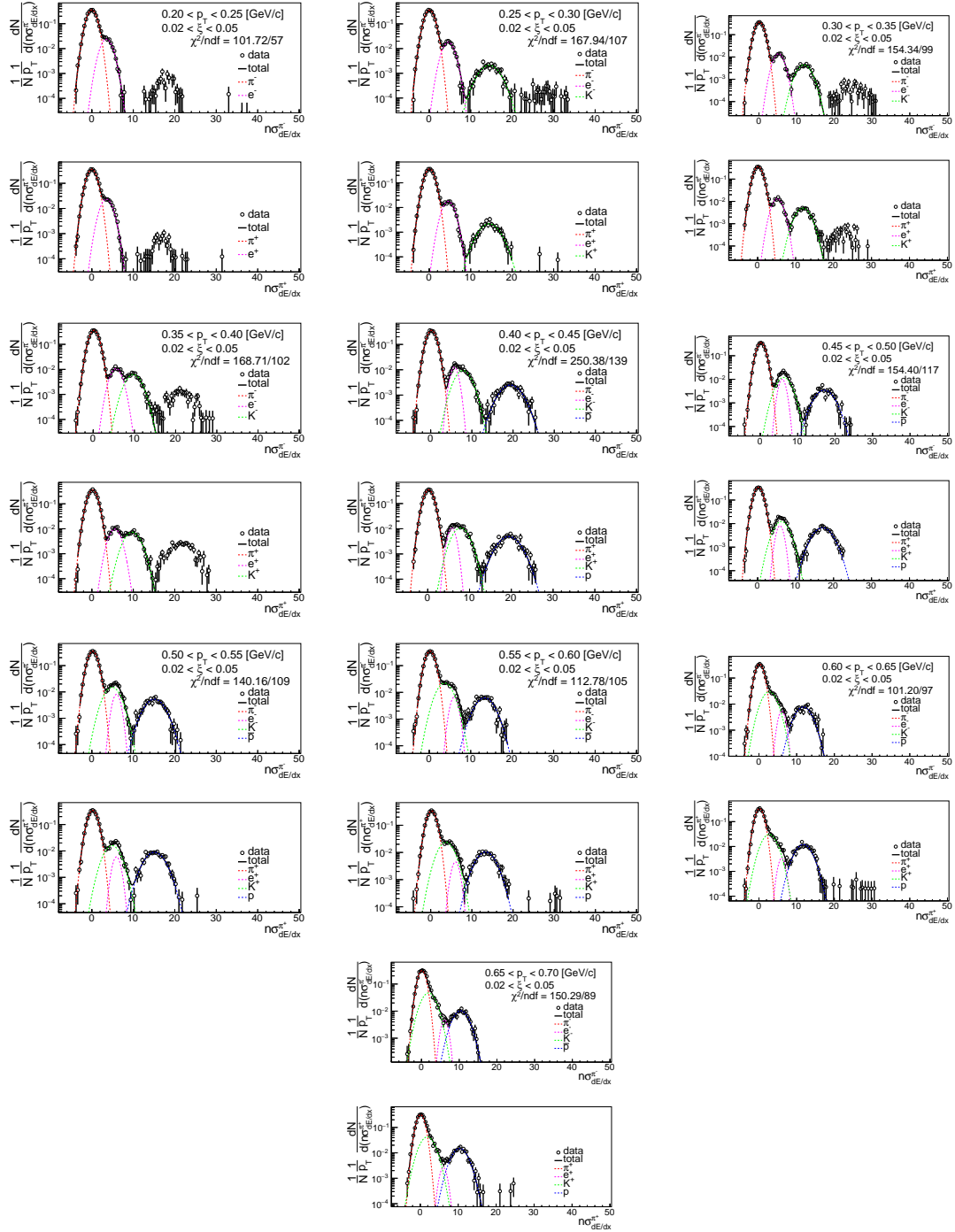
Figure C.1: Distributions of $n\sigma^{\pi^\pm}_{dE/dx}$ for $\pi^\pm$ in SD interactions with $0.02 < \xi < 0.05$.
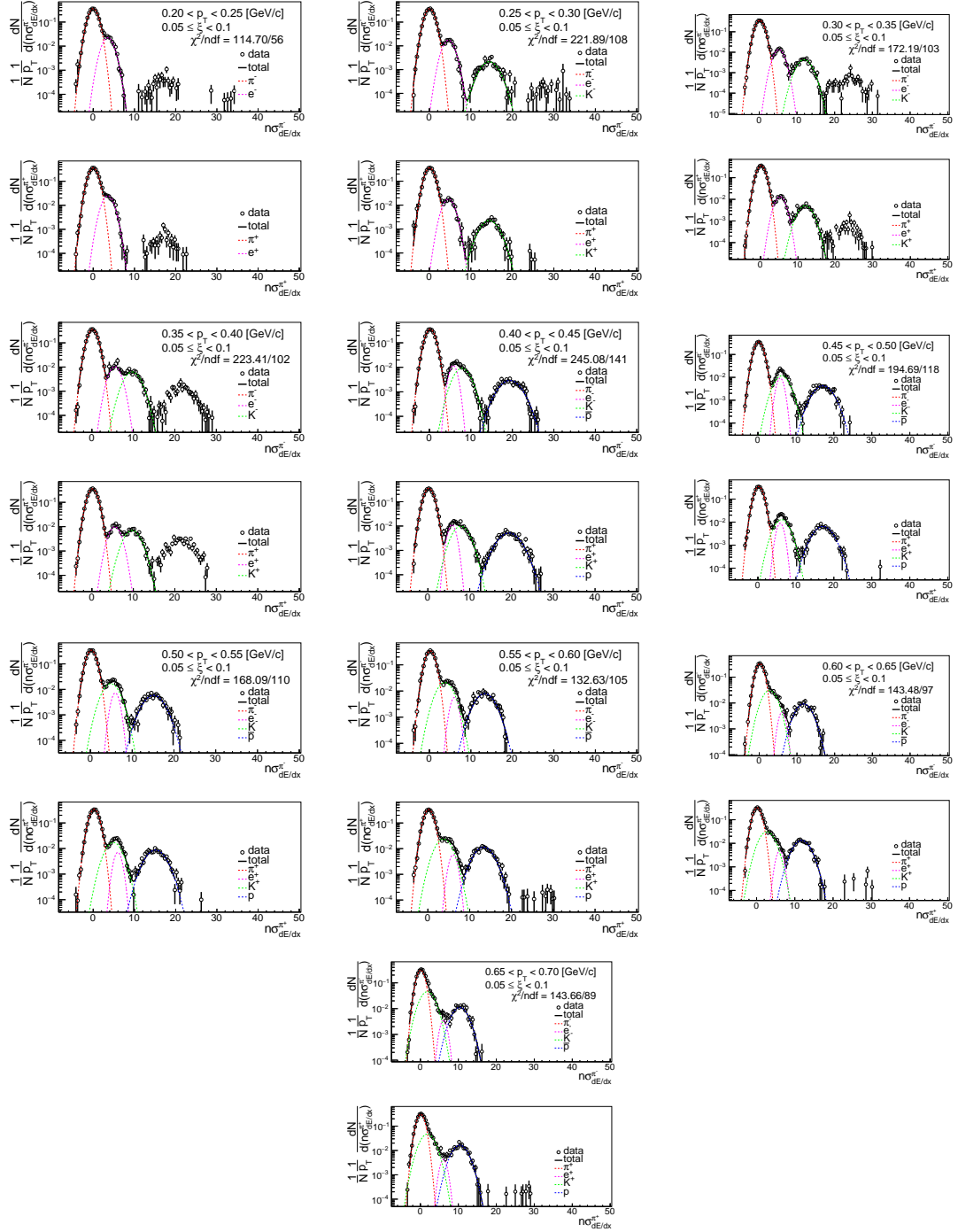
Figure C.2: Distributions of $n\sigma_{dE/dx}^{\pi^{\pm}}$ for $\pi^{\pm}$ in SD interactions with $0.05 < \xi < 0.1$.
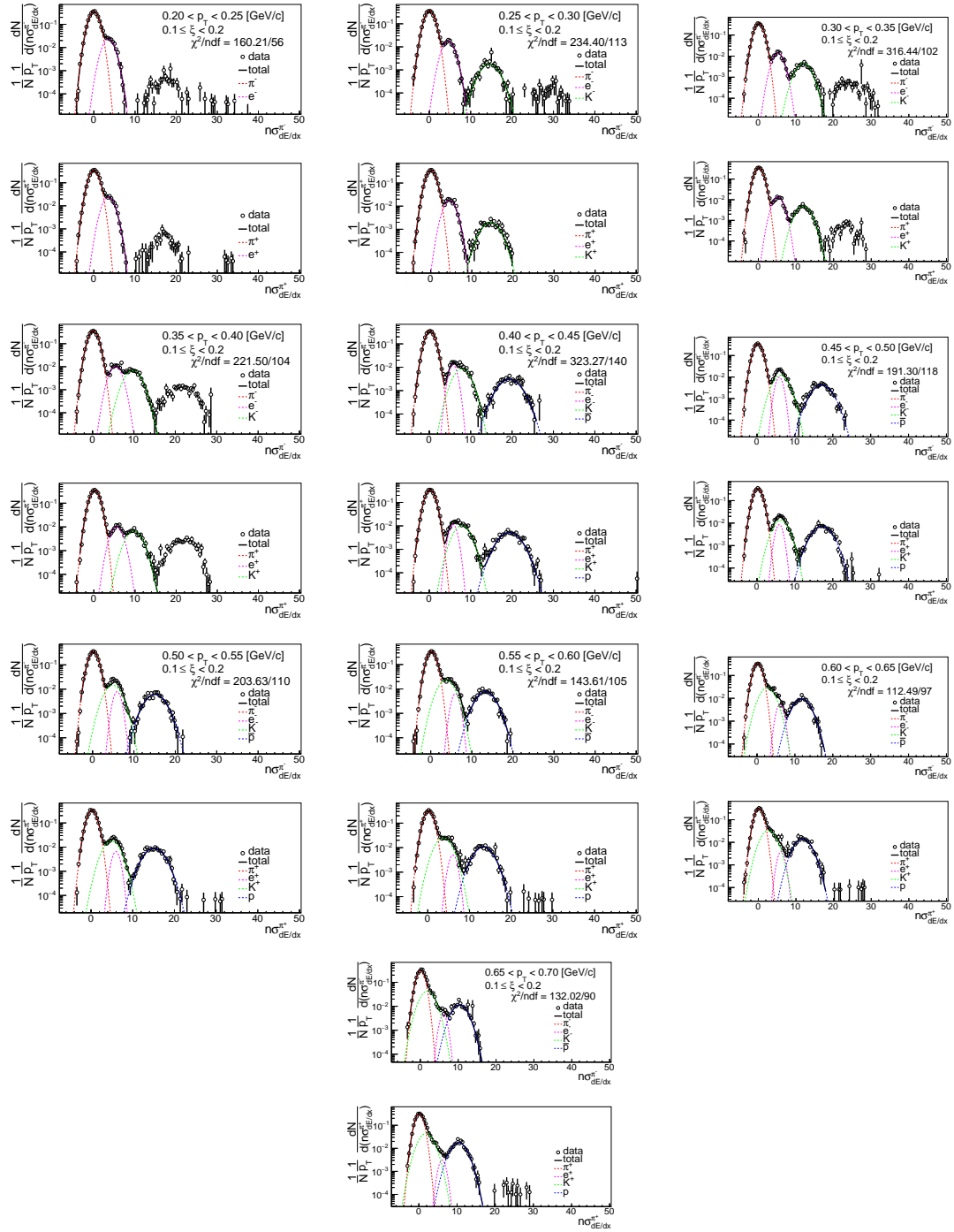
Figure C.3: Distributions of $n\sigma_{dE/dx}^{\pi^\pm}$ for $\pi^\pm$ in SD interactions with $0.1 < \xi < 0.2$.
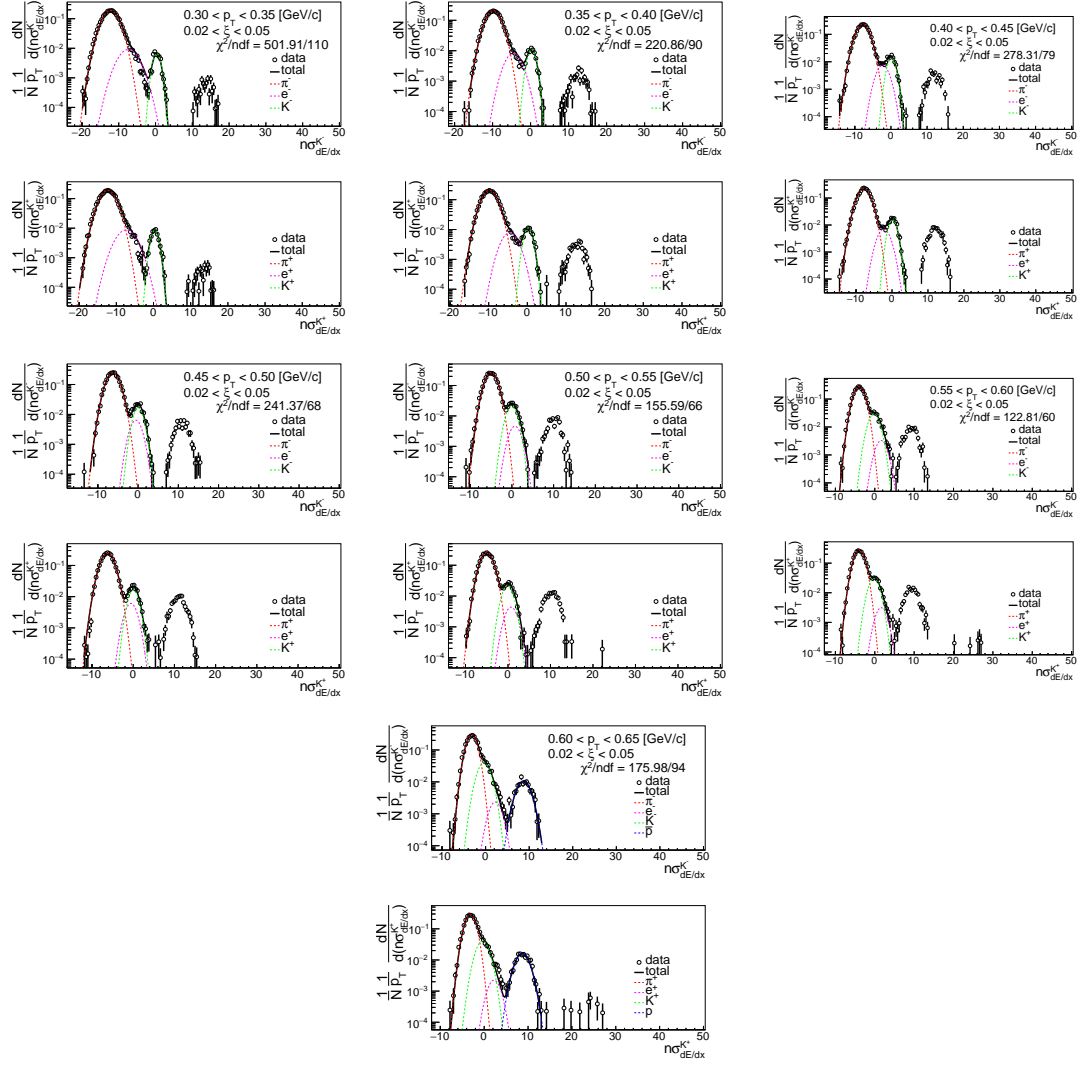
Figure C.4: Distributions of $n\sigma_{dE/dx}^{K^{\pm}}$ for $K^{\pm}$ in SD interactions with $0.02 < \xi < 0.05$.
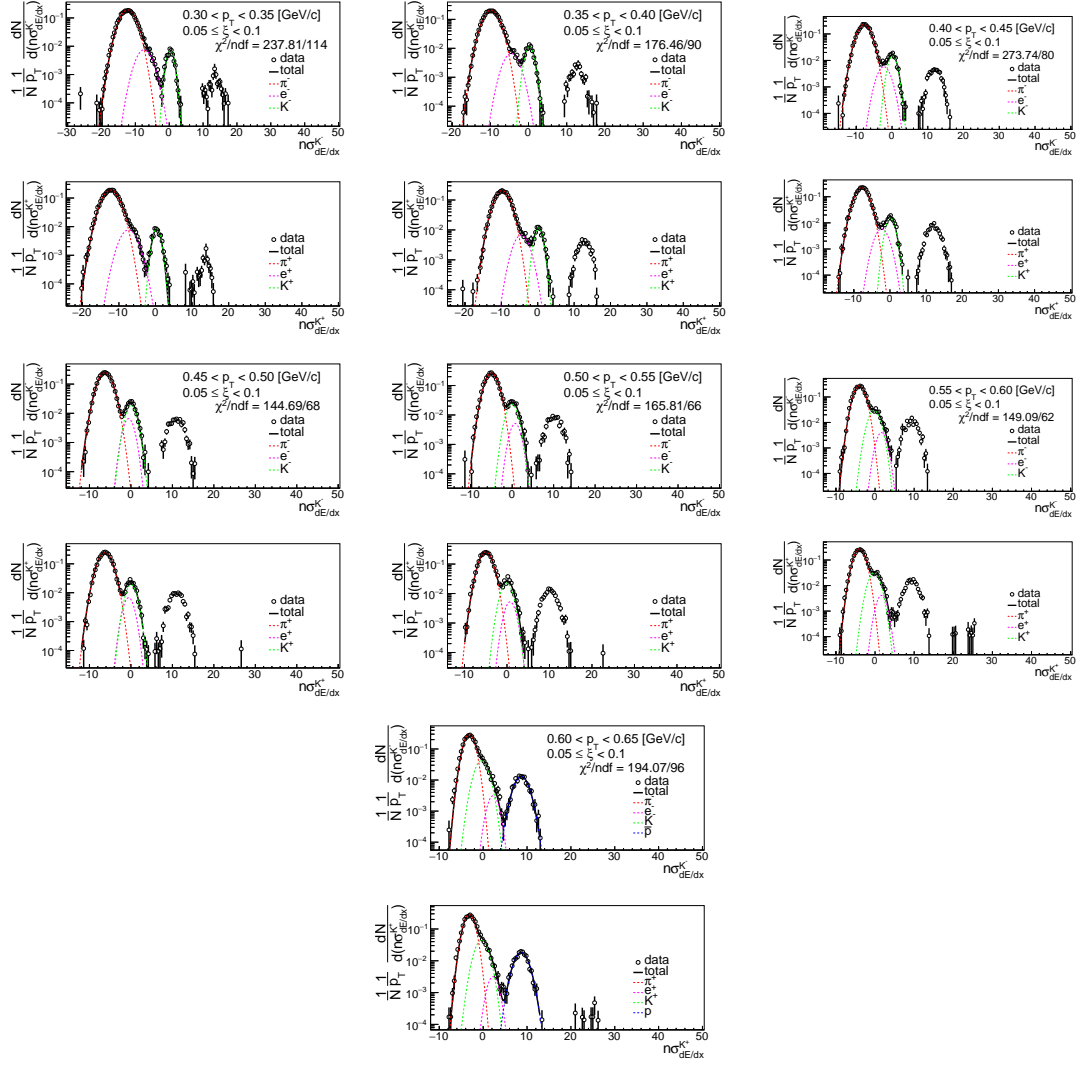
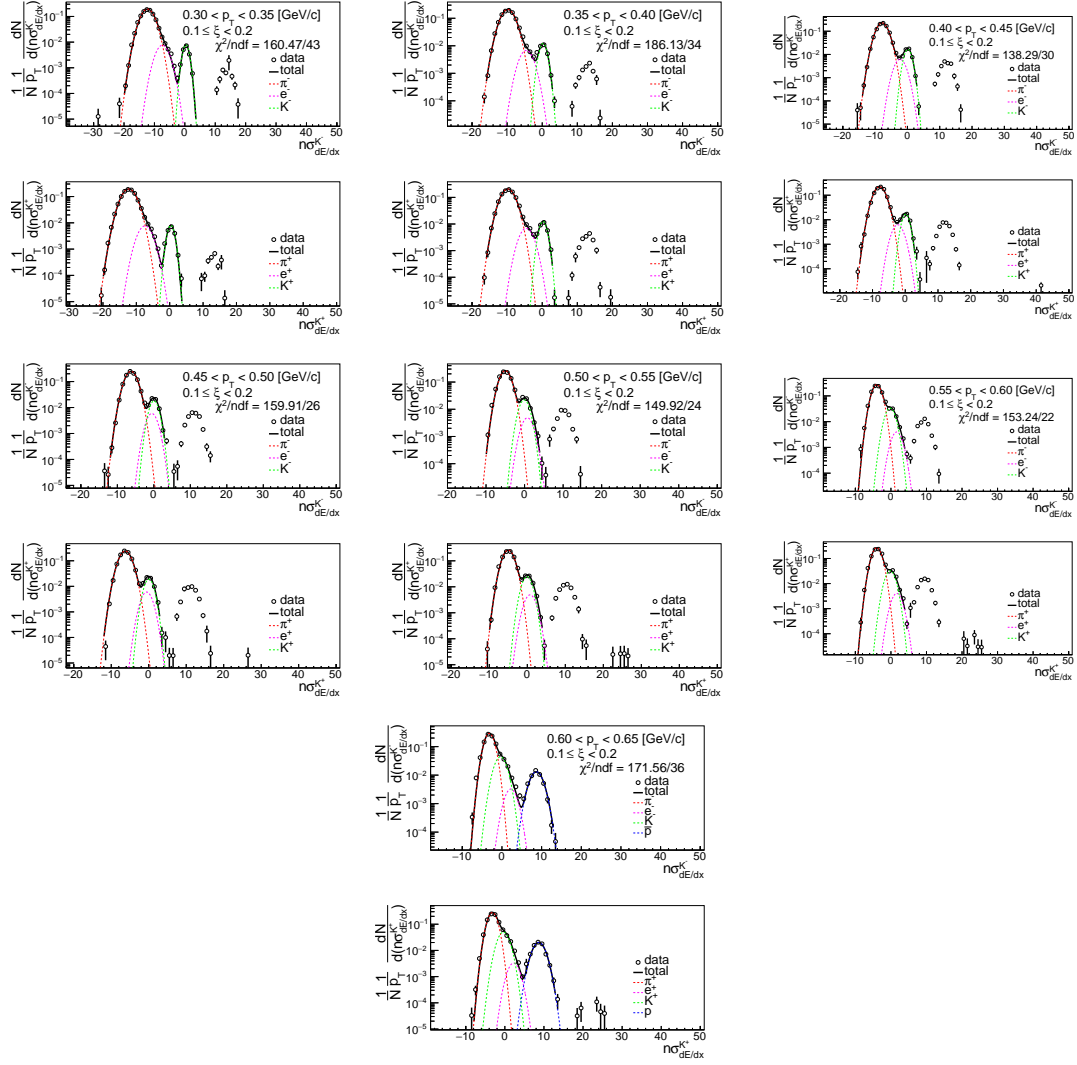Figure C.5: Distributions of $n\sigma_{dE/dx}^{K^\pm}$ for $K^\pm$ in SD interactions with $0.05 < \xi < 0.1$.
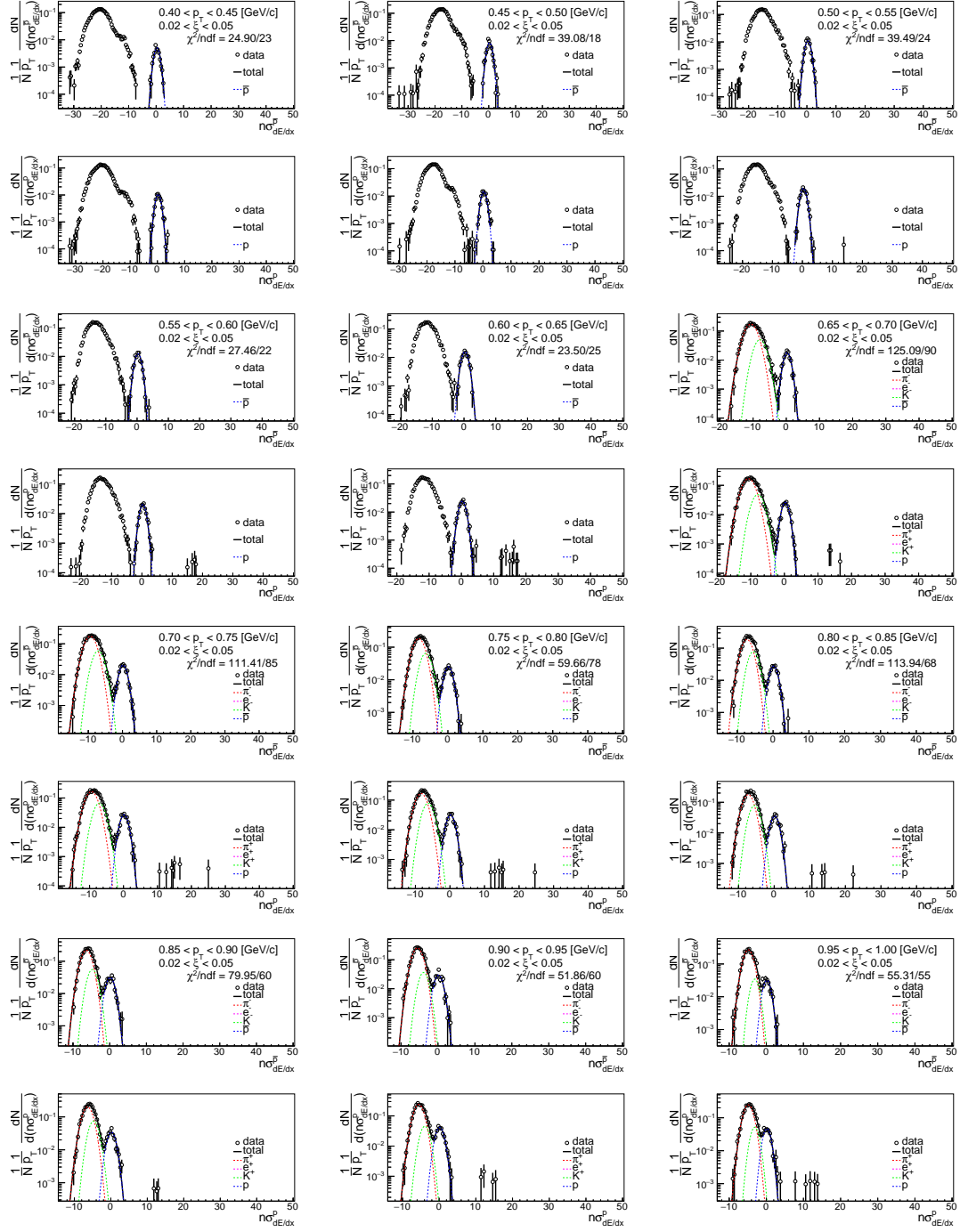
Figure C.6: Distributions of $n\sigma_{dE/dx}^{K^{\pm}}$ for $K^{\pm}$ in SD interactions with $0.1 < \xi < 0.2$.

Figure C.7: Distributions of $n\sigma_{dE/dx}^{\bar{p},p}$ for $\bar{p}, p$ in SD interactions with $0.02 < \xi < 0.05$.
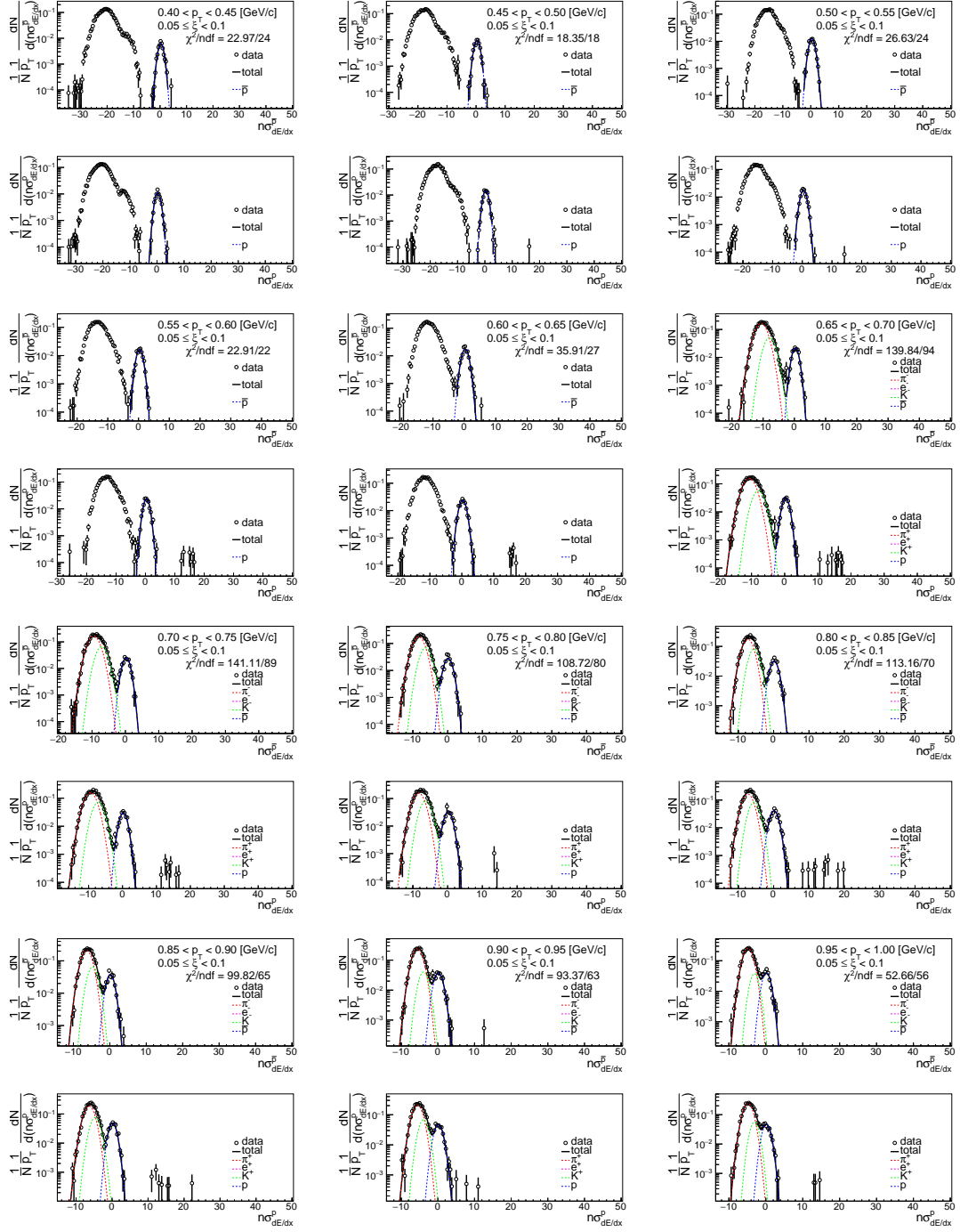
Figure C.8: Distributions of $n\sigma_{dE/dx}^{\bar{p},p}$ for $\bar{p}, p$ in SD interactions with $0.05 < \xi < 0.1$.
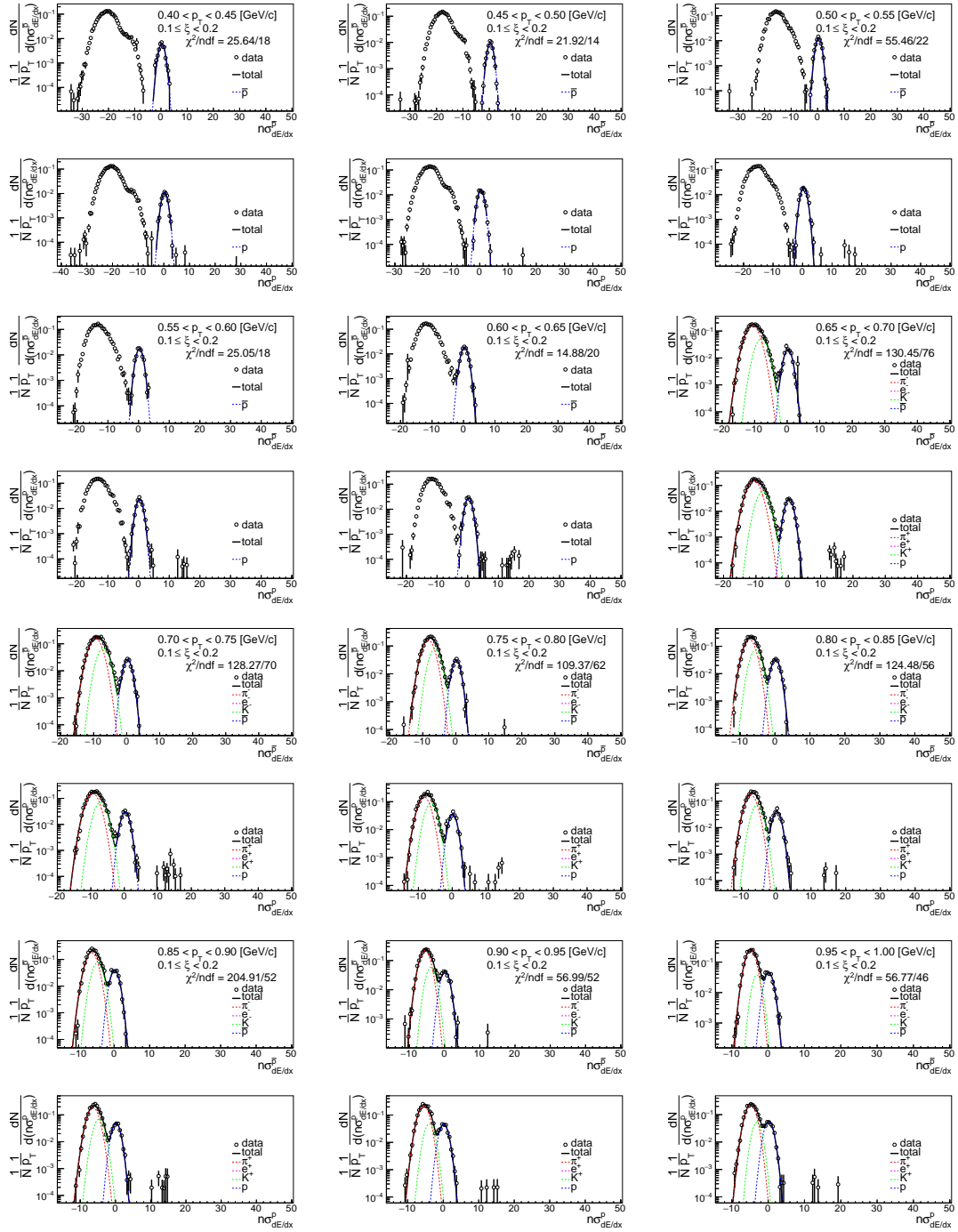
Figure C.9: Distributions of $n\sigma_{dE/dx}^{\bar{p},p}$ for $\bar{p}, p$ in SD interactions with $0.1 < \xi < 0.2$.